The response of moist convection and the atmospheric general circulation to climate warming

by

Martin Simran Singh

Submitted to the Department of Earth, Atmospheric and Planetary Sciences
in partial fulfillment of the requirements for the degree of

Doctor of Philosophy

at the

MASSACHUSETTS INSTITUTE OF TECHNOLOGY

June 2014

Signature redacted

Author ... .
Department of Earth, Atmospheric and Planetary Sciences
May 9, 2014

Signature redacted

Certified by.. .....
Paul O'Gorman
Associate Professor
Thesis Supervisor

Signature redacted

Accepted by ....
Robert D. van der Hilst
Schlumberger Professor of Earth Sciences
Head, Department of Earth, Atmospheric and Planetary Sciences

The response of moist convection and the atmospheric general circulation to climate warming

by

Martin Simran Singh

Submitted to the Department of Earth, Atmospheric and Planetary Sciences
on May 9, 2014, in partial fulfillment of the
requirements for the degree of
Doctor of Philosophy

Abstract

In this thesis, the response of atmospheric circulations to changes in surface temperature is investigated. Both cloud-scale and planetary-scale circulations are considered, and a number of different theoretical and numerical tools are employed.

First, mechanisms maintaining the thermal stratification of a convecting atmosphere are examined based on simulations of radiative-convective equilibrium (RCE) over a wide range of surface temperatures and radiosonde observations of the tropical troposphere. It is argued that cloud entrainment plays a role in determining the lapse rate of convecting regions of the atmosphere, and that this may explain the large increase in convective available potential energy (CAPE) with warming found in the simulations.

Increases in updraft velocity are also found in the RCE simulations as the atmosphere warms. The magnitude of these increases is explained through a conceptual model based on an entraining plume. The results imply that the increase in CAPE identified above is important in determining the behavior of the simulated cloud updrafts in a warming atmosphere.

The precipitation distribution in RCE is also examined. The scaling of precipitation extremes with temperature is found to be amplified by increases in the mean fall speed of hydrometeors as the atmosphere warms. The hydrometeor fall speed affects precipitation rates by altering a measure of the efficiency with which condensation within the column is converted to precipitation at the surface. The potential relevance of this mechanism for convective precipitation extremes on Earth is discussed.

Finally, the large-scale atmospheric circulation response to increasing surface temperature is investigated through a novel transformation of the governing equations. The transformation allows for an upward shift of the circulation with warming, and it is applied to a hierarchy of numerical simulations, including simulations with both idealized and comprehensive general circulation models. The transformation is found to reproduce some of the features of the simulated circulation responses to warming in the middle and upper troposphere, and it has potential applications in understanding the source of inter-model scatter in climate model simulations of global warming.

Thesis Supervisor: Paul O'Gorman
Title: Associate Professor

Acknowledgments

First and foremost I must thank my advisor, Paul O'Gorman, for his tremendous support over the last five years I have been in graduate school. He is a constant source of ideas, and has taught me a great deal about science, as well as life, over our many long conversations. I particularly admire his ability to find humor in all things scientific.

I also wish to thank the rest of my thesis committee, Kerry Emanuel, Alan Plumb and Zhiming Kuang, for their guidance and feedback on my progress throughout my time at MIT. Despite their busy schedules, they have always had time to meet with me and discuss my research, or answer any questions I might have.

The life of the EAPS department are the students and postdocs. I would like to thank past and present officemates, classmates and friends, who, over the years, have provided vibrant discussions of scientific and non-scientific topics, really making MIT a wonderful place to be. In no particular order: Mike Byrne, Alli Wing, Morgan O'Neill, Tim Cronin, Andy Miller, Aditi Sheshadri, Vince Agard, Diane Ivy, Anita Ganesan, Malte Jansen and Dan Chavas.

My partner Jessica has given me a terrific amount of support, particularly in the few months before completing this thesis. I am forever grateful for her eternal patience.

Finally, I am extremely grateful to my parents and my sister for their support and encouragement through my entire life, and for not complaining too much when I decided to move to the other side of the Earth.

I thank George Bryan for making available CM1, and in particular for incorporating many of my suggestions into version 17 of the model. The research in this thesis benefited from high-performance computing support from Yellowstone (ark:/85065/d7wd3xhc) provided by NCAR's Computational and Information Systems Laboratory, sponsored by the NSF. I am grateful for support from NSF grant AGS-1148594.

Contents

List of Figures

List of Tables

Chapter 1

Introduction

1.1 Motivation

The circulation of the atmosphere is highly complex, comprising turbulent flows on a wide variety of spatial scales. Convective clouds have dimensions of a few hundred meters to a few kilometers, while the general circulation operates on planetary scales. Circulations on all of these scales influence climate parameters that are important for human populations.

Consider, for example, the distribution of precipitation on Earth. The mean precipitation in different regions of the globe is largely dictated by the locations of large-scale circulations such as the Hadley and Walker cells, as well as the position of the mid-latitude storm tracks. Indeed, uncertainty in future trends of mean precipitation are dominated by uncertainty in future changes to the large-scale circulation (Seager et al., 2010; Chadwick et al., 2013; Rowell, 2012).

On the other hand, the behavior of smaller-scale circulations, such as those associated with convective clouds, play an important role in setting the intensity of local precipitation, and how this intensity may change with climate (e.g., Romps, 2011; Berg et al., 2013). In particular, the degree to which the intensity of strong precipitation events (precipitation extremes) may increase under future climate change appears to be highly dependent on the behavior of moist convection in a warmer world. Modeling studies robustly predict increases in precipitation extremes with

warming (Kharin et al., 2007; O'Gorman and Schneider, 2009b), and some observational evidence exists for such a response in long-term trends (Westra et al., 2013). But the rate at which precipitation extremes will strengthen as the climate warms remains uncertain in the tropics (O'Gorman and Schneider, 2009a; O'Gorman, 2012) and where convective processes are important (Wilcox and Donner, 2007; Berg et al., 2013).

Small-scale flows also play a role in determining large-scale climate, both via their dynamical effects (e.g., Riehl and Malkus, 1958; Xu and Emanuel, 1989) and via the radiative effects of associated clouds (e.g., Zelinka and Hartmann, 2010). This scale interaction implies that, even if our interest is limited to large-scale climatic features, we must consider how these features may be affected by moist-convective dynamics.

The importance of moist-convection for the circulation of the atmosphere is a particular challenge for the field of climate modeling. Explicitly simulating moist convection in a global model requires immense computational resources, and, aside from a few notable exceptions (e.g., Tomita et al., 2005), most simulations of the global climate rely on general circulation models (GCMs), in which the small-scale convective dynamics are parameterized. While there is a long history in the development of convection parameterizations (see Arakawa, 2004, for a review), these model components are implicated in many shortcomings of the current generation of GCMs (e.g., the "double ITCZ problem", Zhang and Wang, 2006). Additionally, the differences in convection parameterizations in different models may be responsible for some of the inter-model scatter in the mean climate and response to forcing found in GCM simulations (e.g., Frierson, 2007; Wilcox and Donner, 2007). This inter-model scatter is a primary contributor to uncertainty in future predictions of climate change on regional and local scales.

The difficulty in simulating moist convection in large-scale models, as well as the large scatter among future model predictions of climate change, suggests a few important areas where research progress could be made. Firstly, improved theoretical understanding of moist convection is needed, particularly in regards to how it may change as a result of warming of the climate. Since GCMs cannot resolve the relevant

dynamics, process-level studies using other tools, such as cloud-system resolving models (CRMs), may prove useful for this purpose. Secondly, a greater focus is required on understanding the response of GCMs to climate perturbations. For instance, one may ask which aspects of the climate response are robust across models, and why the model spread is large in others. The answers to these questions may be useful in interpreting the results of imperfect model ensembles and may potentially guide research in model development.

In this work, we adopt an idealized approach and consider the effect of changing surface temperature on moist convection as well as the general circulation of the atmosphere. The wide range of spatial scales relevant to the problem necessitates the use of a number of different theoretical and modeling tools. We begin by investigating the behavior of convective dynamics in the simple configuration of radiative-convective equilibrium (RCE). We use a CRM to simulate RCE over a wide range of surface temperatures in order to investigate the scaling of updraft velocity and precipitation intensity as the atmosphere warms. We then turn to the large-scale circulation and the constraints placed on it by the moist governing equations. We construct a transformation of the equations that provides a prediction for the change in vertical structure of the circulation as a result of warming based on knowledge of this structure in the current climate.

1.2 Background

In this section we provide some background on the topics explored in this thesis to give context for the results presented in later chapters. In section 1.2.1 we introduce the concept of radiative-convective equilibrium (RCE), and review some previous results regarding moist convection obtained through this framework. In section 1.2.2 we discuss approaches for understanding and interpreting the results of an ensemble of imperfect climate models to motivate our study of the vertical structure of circulation change presented in chapter 5.

1.2.1 A numerical laboratory for moist convection

A large part of this thesis is concerned with understanding the changing behavior of moist convection as the atmosphere warms. A particularly simple framework within which to study moist convection is that of radiative-convective equilibrium (RCE). The state of RCE may be represented conceptually as a horizontally infinite atmosphere existing above a uniform surface. Radiation acting on this system causes the atmosphere to cool, and the resulting destabilization allows convective clouds to develop. Eventually, a statistical equilibrium is achieved, and turbulent fluxes of sensible and latent energy, communicated through the troposphere by convection, balance the loss of energy by radiative processes.

In contrast to other simple idealizations, such as Rayleigh-Bernard convection, RCE is difficult, if not impossible, to simulate in the laboratory. This is particularly true if one is studying moist convection, for which processes relating to condensation and precipitation are of first order importance. In many regards, however, RCE is the simplest configuration in which to study moist convection in numerical models. There is a long history of RCE studies being used to understand aspects of the climate, and a rich literature exists examining different aspects of this seemingly simple problem.

Some of the early work involving RCE in relation to climate was concerned with how radiative and convective processes combine to determine the mean temperature of the planet (Manabe and Strickler, 1964). Indeed, RCE models produced some of the first estimates of climate sensitivity (Manabe and Wetherald, 1967), estimates that are not too different from values obtained using modern GCM simulations of greenhouse-gas induced warming (see e.g., Collins et al., 2013).

In the last two decades, computational resources have grown such that explicit simulations of moist convection in RCE have become possible using cloud-system resolving models (CRMs) (e.g., Held et al., 1993; Islam et al., 1993; Robe and Emanuel, 1996; Tompkins and Craig, 1998). In such studies, RCE is typically modeled using a finite domain with doubly periodic boundary conditions and horizontal grid spacings of the order of one kilometer or less. While these resolutions are only barely

convection resolving (Bryan et al., 2003), CRMs run in the state of RCE provide a convenient numerical laboratory within which to test theories of moist convection.

A surprising finding based on RCE studies in CRMs is the possibility of what has become known as convective *self-aggregation* (Held et al., 1993; Bretherton et al., 2005; Muller and Held, 2012; Wing and Emanuel, 2014). In disaggregated convection, which appears to be the more common state in simulations of RCE, convective clouds occur randomly throughout the domain. When convection is aggregated, all of the active convective elements are constrained to a small region, while weak subsidence occurs over the rest of the domain. The appearance of self-aggregation in simulations of RCE has been argued to be a manifestation of an instability of the RCE state itself (Emanuel et al., 2014). Indeed, global simulations of RCE develop planetary-scale clusters of convective activity, even when the boundary conditions are horizontally uniform (Popke et al., 2013). Despite this potential instability to large-scale disturbances, RCE is nonetheless a useful idealization through which to probe the behavior of moist convection, and we will use it extensively in this thesis.

A very basic question one may ask about the behavior of moist convection is: what sets the magnitude of the buoyancy and updraft velocity in clouds? Buoyancy and updraft velocity scales for dry convection may be derived based on simple physical or dimensional considerations (see e.g., Emanuel et al., 1994; Emanuel, 2001), but a complete theory for these properties in moist convection remains elusive. Dry convection is (in the Buossinesq limit) symmetric to an inversion of the vertical axis, and thus one may assume that updrafts and downdrafts will occupy roughly equal areas of the domain. Moist convection, on the other hand, has long been known to favor narrow intense updrafts within clouds interspersed with weak clear-air subsidence (e.g., Bjerknes, 1938; Pauluis and Schumacher, 2011).

A number of authors have derived scalings for moist-convective buoyancy and updraft velocity based on the twin constraints of the energy and entropy budgets (Emanuel and Bister, 1996; Rennó and Ingersoll, 1996; Robe and Emanuel, 1996; Craig, 1996). These studies attempt to constrain the frictional dissipation associated with convective air motions based on the total irreversible entropy production in

the atmosphere. However, subsequent work has shown that the irreversible entropy production in RCE is primarily related to moist processes such as the frictional dissipation associated with falling hydrometeors (Pauluis et al., 2000) and irreversible mixing of dry and moist air parcels (Pauluis and Held, 2002a,b). These extra entropy sources must be taken into account in order for any theory based on the entropy budget to succeed.

An alternative hypothesis was put forward by Parodi and Emanuel (2009), who suggested that the fall speed of hydrometeors plays a key role in determining the updraft velocity in moist convection. Their analysis is based on a balance between updrafts lofting condensed water into the atmosphere and the condensed water itself reducing the buoyancy of clouds. They present an elegant "moist scaling" equation that accounts for changes in updraft velocity found in simulations of RCE with a simple warm-rain microphysics scheme in which the fall speed of rain was artificially varied. However, it is unclear if this represents a general result, and if, for example, the moist scaling equation may be applied to more complex situations involving ice-phase hydrometeors as well as rain.

Recent studies have considered the specific problem of how moist-convective updraft velocity may change as a result of warming of the atmosphere. CRM simulations of RCE run over different surface temperatures show an increase in the buoyancy and peak updraft velocity of convective clouds with warming (Romps, 2011; Muller et al., 2011). These studies with explicit convection, as well as other modeling studies using parameterized convection (Sobel and Camargo, 2011; Fasullo, 2012), have also found increases in convective available potential energy (CAPE) as the surface temperature increases. CAPE refers to the amount of energy available to a parcel that rises from the surface without mixing with the environment. One may construct a velocity scale $w_{CAPE} = (2CAPE)^{1/2}$ based on CAPE which refers to the peak updraft of such a parcel. To the extent that clouds may be represented by air parcels ascending without dilution to the upper troposphere, the updraft velocity increases would be expected to follow those of w_{CAPE}. But it is known that undilute ascent is extremely rare in simulated clouds (Romps and Kuang, 2010a), and the CAPE velocity scale has

been found to be considerably larger than typical updrafts in simulations of moist convection (Muller et al., 2011). What causes the increase in updraft velocity in RCE simulations, and whether this increase is related to changes in CAPE are currently open problems in the field. The aim of chapters 2 and 3 of this thesis is to make progress towards understanding the temperature dependence of cloud buoyancy and updraft velocity in moist convection, and to evaluate whether the increases found in idealized simulations of warming may have implications for convection in a warmer climate.

The magnitude of the updraft velocity in moist-convective clouds is strongly tied to the intensity of precipitation. In RCE, the total convective mass flux and domain-mean precipitation are constrained by the energy budget such that the integrated latent heating approximately balances the free-tropospheric radiative cooling (Robe and Emanuel, 1996; Takahashi, 2009). The intensity of precipitation, however, depends on the area over which this mass flux occurs. For large values of the updraft velocity, the convective mass flux is spread over a small area, and the local precipitation rate is large.

A particularly relevant question for this thesis relates to how convective precipitation intensity may change as a result of warming. The precipitation rate of a convective cloud is related to the rate at which the cloud updraft transports water out of the boundary layer (e.g., Muller et al., 2011). As the surface temperature increases, the saturation specific humidity increases roughly exponentially, following the Clausius-Clapeyron equation. For modest changes in relative humidity, this results in a large increase in the amount of water vapor in the atmosphere as the surface warms. A given updraft will then transport more water vapor out of the boundary layer, resulting in increasing precipitation rates with increasing surface temperature.

Studies of the precipitation distribution in RCE have found that, at surface temperatures characteristic of Earth's tropics, the intensity of the strongest precipitation events (precipitation extremes) increases with warming in proportion to the increase in saturation specific humidity near the surface (Muller et al., 2011; Romps, 2011). This rate of increase is roughly 6-7% K^{-1}, and has been termed Clausius-Clapeyron

(CC) scaling. CC scaling of heavy precipitation is consistent with a very simple view of a deep convective cloud as transporting mass into the upper troposphere at a rate that remains fixed with warming. But given the changes to the updraft velocity mentioned above, as well as the complexity of cloud-scale circulations in simulations, it is unclear whether CC scaling of precipitation extremes represents a general constraint, or if factors other than the surface moisture play a role in determining the scaling of precipitation extremes with warming. Indeed, observational analyses of variability suggest that, in some locations, convective precipitation extremes increase with temperature at much higher rates than implied by the increase in surface humidity (Lenderink and van Meijgaard, 2008; Berg et al., 2013). In chapter 4 we will investigate the scaling of high percentiles of the precipitation distribution in RCE over a wide range of temperatures to evaluate possible mechanisms that might lead to increases in precipitation extremes with warming different from those implied by CC scaling.

1.2.2 Understanding climate model ensembles

In chapter 5 of this thesis we focus on the large-scale circulation of the atmosphere and how it may change with warming. A common tool used to study the large-scale atmospheric circulation is the general circulation model (GCM). The aim of these models is to provide a numerical solution to the equations governing flow on a sphere, including equations for conservation of momentum, mass and energy. But, as noted earlier, GCM resolutions are too low to explicitly resolve all the relevant dynamics, and parameterizations are required for certain small-scale processes such as moist convection.

The different representations of sub-grid scale processes among different models is one reason why GCMs do not all agree on the details of the atmospheric circulation or how it may change in the future. A key goal for climate research is to reduce the uncertainty in climate predictions by reducing the scatter in the response of climate models to future natural and anthropogenic forcing. However, even for aspects of this response where GCMs agree, our imperfect knowledge of how to represent sub-grid

processes limits the certainty we have that the model response is the correct one. It is crucial, therefore, that along with improving climate models, we endeavor to understand their future climate responses, and if possible, understand the reasons why they may disagree.

Two contrasting techniques are often used when analysing climate model ensembles. One approach is to focus on the responses that are robust across different models. Since these robust responses are reproduced by a number of models with different formulations and parameterizations, one may expect the particular behavior in question to be the result of some basic physics that may be understood in simple terms. A classic example of this thinking is the study by Held and Soden (2006), in which the intensification of the hydrological cycle (as measured by precipitation minus evaporation) found in many GCM simulations of warming is related to a simple thermodynamic increase in the saturation vapor pressure. Understanding such robust GCM responses is useful in that it may provide confidence that a particular model result will apply to Earth's climate, and it may suggest novel frameworks through which to analyze model output [see Seager et al. (2010) for an example based on the results of Held and Soden (2006)].

A somewhat different approach is to explicitly use the scatter among GCM predictions in combination with observations to attempt to constrain some aspect of the climate system. For example, as described previously, tropical precipitation extremes increase with warming at very different rates in different GCMs. O'Gorman (2012) noted that the rate at which precipitation extremes increased as a result of global warming in a given GCM was related to the response of precipitation extremes to interannual climate variability in the same model. Since there exists observational constraints on the response of precipitation extremes to interannual variability, this model-derived relationship could be used to provide a prediction for long-term changes in precipitation extremes. This second method requires there to be a relationship between some observable quantity in the current climate and some predicted quantity in a changed climate across the model ensemble. But given such a relationship, it may allow for a substantial reduction in the uncertainty associated with the predicted

quantity, as well as possibly provide insights on the reasons behind the different model responses across the ensemble.

In chapter 5, we borrow from both perspectives outlined above to investigate the vertical structure in the change to the atmospheric circulation as the climate warms in terms of an upward shift. An upward shift of the circulation with warming has been noted by a number of authors in a variety of variables such as static stability (Kushner et al., 2001), relative humidity (Sherwood et al., 2010), transient kinetic energy and momentum flux (Lorenz and DeWeaver, 2007), large-scale condensation rate (O'Gorman and Schneider, 2008) and cloud fraction (Mitchell and Ingram, 1992; Tompkins and Craig, 1999). Motivated by this robust model response, our aim in chapter 5 is to document to what degree the change in circulation as a result of warming may be considered a coherent upward shift involving all dynamical variables at all latitudes. A potential application of such an approach is suggested by Sherwood et al. (2010). They noted that predictions of changes to the relative humidity distribution with warming in different GCMs could, in part, be related to the climatological relative humidity distribution in each model via an upward and poleward shift. Studying circulation changes through an upward shift, therefore, may also be useful in understanding inter-model scatter in the circulation response to warming.

1.3 Outline

In this thesis we consider several specific aspects of the more general question: how do atmospheric circulations respond to a warming or cooling of the climate? Our study encompasses motions on the scale of convective clouds as well as the general circulation of the atmosphere.

In chapter 2 we examine the mechanisms that determine the thermal stratification of the tropical atmosphere. Based on numerical simulations of RCE at different surface temperatures and observations of the tropical western Pacific, we will argue that entrainment influences the lapse rate of convecting regions in the atmosphere. We will develop a conceptual model of a convective ensemble, based on an entraining

plume, that predicts that the lapse rate of an atmosphere in RCE systematically deviates from that of a moist adiabat as the atmosphere warms. These changes in lapse rate imply large increases in the CAPE with warming, consistent with the behavior of the simulations.

In chapter 3 we consider the scaling of moist-convective buoyancy and updraft velocity with temperature. We will show that simulations of RCE predict substantial increases in updraft velocity and cloud buoyancy with warming, particularly for the most intense updrafts. These results are interpreted through a set of conceptual models of a convective ensemble based on an entraining plume, including a generalization of the plume model introduced in chapter 2. We argue that the lapse-rate changes associated with the CAPE increase play a leading role in allowing the simulated updraft velocity to increase with warming.

In chapter 4 we turn our attention to precipitation rates in RCE, and in particular the scaling of strong precipitation events (precipitation extremes) with warming. We confirm previous results that, at surface temperatures characteristic of Earth's tropics, precipitation extremes increase with warming in proportion to the amount of moisture near the surface. However, we will show that this is not a general constraint, and increases in precipitation extremes with warming substantially larger than implied by the scaling of surface moisture occur over a wide range of temperatures. We will argue that these high rates of increase in precipitation extremes are related to increases in hydrometer fall speed accompanying warming. These results highlight the importance of microphysics in determining precipitation rates, at least for short accumulation periods [see also Parodi et al. (2011)].

Finally, in chapter 5, we consider the response of the large-scale circulation to global warming. In particular, we examine the response of the vertical structure of the atmospheric general circulation in response to perturbations in surface temperature. We consider the equations governing the large-scale atmospheric flow and develop a transformation that allows for an upward shift of the circulation with warming. The transformation is used to understand the response of a hierarchy of models to small increases in surface temperature. We will show that this transformation provides a

useful framework within which to interpret changes in the circulation in the middle and upper troposphere, but, because of the inability of the transformed solution to satisfy the correct boundary conditions, does not apply in the lower troposphere.

The four chapters of the main body of this thesis are in varying stages of publication or preparation for publication in peer-reviewed journals. Chapter 2 is published as Singh and O'Gorman (2013), and is reproduced here with minor alterations for clarity. Chapter 3 is in preparation for possible publication, while chapter 4 has been submitted to the journal *Geophysical Research Letters*. Chapter 5 is largely a reproduction of Singh and O'Gorman (2012) with minor edits. In chapter 6 we present a summary of our findings and discuss possible future work.

Chapter 2

Influence of entrainment on the thermal stratification in simulations of radiative-convective equilibrium

2.1 Introduction

Convective available potential energy (CAPE), defined as the integrated buoyancy experienced by an undilute parcel as it rises to its level of neutral buoyancy (LNB), is a common measure of the deviation of the atmospheric thermal stratification from that of an undilute moist adiabat. CAPE over the tropical oceans has been found to increase rapidly in climate-model simulations of global warming, with increases of up to 25% occurring in projections of 21st century climate (Sobel and Camargo, 2011; Fasullo, 2012). CAPE also increases with warming in simulations of radiative-convective equilibrium (RCE) performed using cloud-system resolving models (CRMs) (Muller

[1]Material in this chapter is a slightly edited version of: Singh, M. S., and P. A. O'Gorman (2013), Influence of entrainment on the thermal stratification in simulations of radiative-convective equilibrium, *Geophys. Res. Lett.*, 40, 43984403, doi:10.1002/grl.50796. Reproduced with permission.

et al., 2011; Romps, 2011). Despite the robustness of this result, it is not clear why the CAPE increases with temperature, or what the implications for updraft velocities and precipitation intensity may be.

In this study, we show that the increase in CAPE with warming occurs over a wide range of temperatures in simulations of RCE with different CO_2 concentrations. Consistent with previous work (Muller et al., 2011), typical buoyancies found inside clouds are much smaller than those associated with the undilute parcels used to define CAPE. This suggests that entrainment of dry air may be important in setting cloud buoyancy. Motivated by the relative smallness of the cloud buoyancy, we show that the increase in CAPE with warming can be accounted for using a conceptual model in which the atmosphere remains close to neutrally buoyant with respect to an entraining plume with a fixed entrainment profile. The extent to which entrainment reduces the plume buoyancy depends on the saturation deficit of the mid-troposphere, and this saturation deficit increases with warming if the relative humidity remains roughly constant. The greater CAPE in a warmer atmosphere then results from a greater difference in temperature between the entraining plume and the undilute parcel used in the calculation of CAPE.

The conceptual model outlined here is consistent with the convective quasi-equilibrium hypothesis as described by Arakawa and Schubert (1974) in which it is argued that moist convection constrains the "cloud work-function" (a plume-based counterpart to CAPE that considers entrainment) to be close to zero. A role for entrainment in helping to determine cloud buoyancies in moist convection is supported by CRM simulations and some observational studies (e.g., Derbyshire et al., 2004; Holloway and Neelin, 2009; Kuang and Bretherton, 2006; Romps and Kuang, 2010a; Zipser, 2003; Molinari et al., 2012). Others, however, have argued for the importance of undilute ascent in maintaining the mean thermodynamic structure of the tropical atmosphere (e.g., Riehl and Malkus, 1958; Xu and Emanuel, 1989), and it is unclear whether current models adequately represent the relevant mixing processes. Thus, we also provide observational support for the conceptual model discussed above by showing it is consistent with observed lapse rates from radiosondes in the tropical

western Pacific; drier soundings (greater saturation deficit) allow for greater CAPE in a manner consistent with the plume model used to account for the CRM results.

We begin by describing the CRM simulations and the CAPE of the mean profiles (section 2.2). We then introduce a simple bulk entraining plume model in the limit of zero buoyancy that accounts for the CRM results and which highlights the importance of mid-tropospheric humidity in modulating the effect of entrainment (section 2.3). We also present observational evidence for a relationship between tropospheric humidity and lapse-rate; this evidence suggests the mechanisms found in the CRM and plume model may be relevant to the atmosphere (section 2.4). Finally, we give a summary of our conclusions and their implications (section 2.5), and include a supplementary section outlining details not covered in the main body of this chapter (section 2.6).

2.2 CAPE in a cloud-system resolving model

We describe results from three-dimensional doubly-preiodic simulations of radiative-convective equilibrium (RCE) over a wide range of sea-surface temperatures and atmospheric CO_2 concentrations using a model similar to version 16 of the Bryan Cloud Model (Bryan and Fritsch, 2002) with minor alterations to improve energy and mass conservation described in the appendix. The model is fully compressible and non-hydrostatic, and it uses 6th order spatial differencing coupled with 6th order hyper-diffusion for numerical stability. Time stepping is performed using a split-explicit scheme based on that of Wicker and Skamarock (2002). Fluxes of sensible heat, moisture and momentum from the surface are calculated using bulk aerodynamic formulae, with turbulent exchange coefficients evaluated based on Monin-Obukov similarity theory. Microphysics are parameterized following the single-moment scheme of Lin et al. (1983) including six prognostic water species. Sub-grid motions are parameterized via a Smagorinsky turbulence scheme with separate diffusion coefficients for the vertical and horizontal directions (Bryan and Rotunno, 2009). A band-averaged radiative transfer scheme is used, and all simulations are performed with a constant

solar flux of 390 W m^{-2} incident at a zenith angle of 43° (i.e., no diurnal cycle of radiation is included). Simulations are run with identical ozone profiles typical of the tropical atmosphere with a maximum in mixing ratio near 10 hPa, and each simulation includes 64 vertical levels, with the model top set to 26 km. Rayleigh damping is applied to the velocity fields in the upper 2 km to prevent gravity-wave reflection.

Nine simulations are conducted, each with a different imposed CO_2 concentration in the range 1 ppmv – 1280 ppmv and a corresponding SST between 286 K and 309 K. The simulations are run with a horizontal grid-spacing of 1 km in a 84×84 km doubly periodic domain for 40 days, with statistics collected over the last 20 days [see supplementary information (section 2.6) and Fig. 2-4]. The SST is fixed in each simulation and is chosen as the equilibrium SST in a corresponding lower-resolution slab-ocean simulation with the same atmospheric CO_2 concentration (supplementary information; Fig. 2-5). Further details of the model and simulations are given in the supplementary information (section 2.6).

Figure 2-1a shows that the CAPE in the CRM simulations increases quasi-exponentially with SST. The same data are plotted with a logarithmic ordinate in Fig. 2-6. CAPE is defined as the vertical integral of the positive buoyancy of a pseudo-adiabatic parcel lifted to its level of neutral buoyancy (LNB). [Similar behavior is found for reversible CAPE (Fig. 2-7).] The buoyancy of the parcel is calculated relative to the domain- and time-mean virtual temperature profile, and the parcel is initialized with the mean temperature and specific humidity of the lowest model level. Ice is treated with a mixed phase over the range 233.15 K to 273.15 K consistent with the CRM thermodynamics. The CAPE values range from less than 200 J kg^{-1} in the coldest simulation to more than 5000 J kg^{-1} in the warmest simulation. The increase in buoyancy of the undilute parcel is most pronounced in the upper troposphere, and there is also an important contribution from the increase in height of the LNB (Figure 2-2a). The fractional rate of increase of CAPE is approximately 12% K^{-1} at an SST of 300 K, which is somewhat larger than the rates of increase of 8% K^{-1} (Muller et al., 2011) and 7% K^{-1} (Romps, 2011) found in previous studies of RCE. [In the latter publication this was misstated as being per doubling of CO_2; D.M. Romps, 2013, pers.

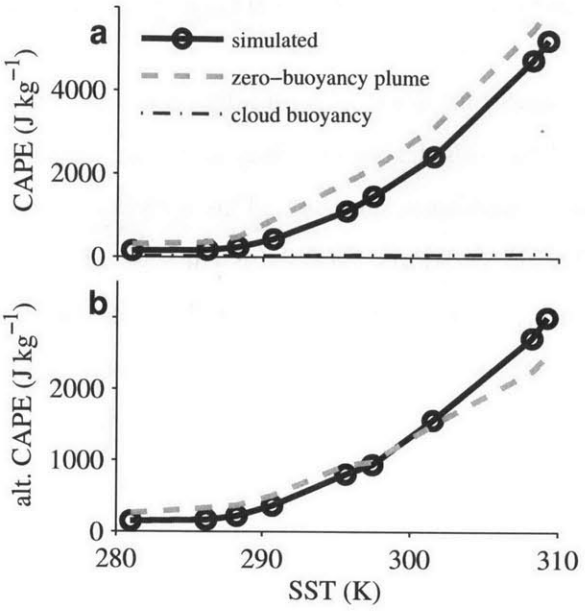

Figure 2-1: Pseudo-adiabatic CAPE in simulations of radiative-convective equilibrium (solid lines with circles) and as predicted by the zero-buoyancy plume model (dashed lines). CAPE is calculated by integrating positive parcel buoyancy up to (a) the LNB or alternatively (b) the anvil detrainment level. The anvil detrainment level is taken to be the level of maximum horizontal- and time-mean cloud-ice concentration in the simulations. The dot-dashed line in (a) shows the cloud-buoyancy integral as defined in the text.

comm.]

Figure 2-1a also shows the cloud-buoyancy integral in each simulation. The cloud-buoyancy integral is a measure of the energy available to convective motions that does not depend on a parcel definition. It is defined to be the vertical integral of the mean buoyancy in cloudy updrafts relative to the domain and time mean. Cloudy updrafts are identified as all points with upward velocity greater than 2 m s^{-1} and cloud water content greater than 0.01 g kg^{-1}, and the integral is taken over all levels for which the mean cloud buoyancy is positive. The cloud-buoyancy integral also increases with SST, but its absolute value is much smaller than the CAPE, with the CAPE being five times larger at the lowest SST and almost fifty times larger at the highest SST (see Fig. 2-6). In the next section we use this property together with a bulk plume model of convection to better understand why CAPE increases with SST.

2.3 Zero-buoyancy entraining plume model

The smallness of the cloud-buoyancy integral relative to the CAPE suggests that some insight may be gained by considering the limit in which clouds are exactly neutrally buoyant with respect to their environment. (This zero-buoyancy limit was previously considered by Bretherton and Park (2008) for the case of shallow convection.) We work with an entraining plume as a highly simplified model of an ensemble of convective clouds; similar models are used in many convective parameterizations (e.g., Tiedtke, 1989).

2.3.1 Derivation

First consider the approximate plume equation,

$$\frac{dh}{dz} = -\epsilon(h - h_e), \tag{2.1}$$

where ϵ is the entrainment rate, $h = c_p T + gz + L_v q_v$ is the moist static energy, and the subscript e refers to the environment. Here c_p is the isobaric specific heat capacity of air, L_v is the latent heat of vaporization, T is the temperature, q_v is the specific humidity, g is the gravitational acceleration, and z is height. Ignoring virtual temperature effects, the assumption of neutrality implies $T = T_e$ and thus $h - h_e = L_v(q_v - q_{ve})$. Above cloud base, the plume is saturated such that $h = h^* = h_e^*$ and $q_v = q_v^* = q_{ve}^*$, where an asterisk refers to a quantity at saturation. Using these expressions to evaluate (2.1) above cloud base gives

$$\frac{dh_e^*}{dz} = -\epsilon L_v(q_{ve}^* - q_{ve}). \tag{2.2}$$

Note that (2.2) is written only in terms of properties of the environment and the entrainment rate ϵ.

Next consider an undilute parcel used in the calculation of CAPE that conserves its moist static energy h_u such that $dh_u/dz = 0$. Subtracting (2.2) from the undilute

parcel equation gives

$$\frac{d}{dz}(h_u^* - h_e^*) = \epsilon L_v (q_{ve}^* - q_{ve}) \tag{2.3}$$

above cloud base. Assuming for simplicity a constant entrainment rate and a constant environmental relative humidity $\mathcal{R}_e \simeq q_{ve}/q_{ve}^*$, we may use equation (2.3) to approximate the temperature difference ΔT between the undilute parcel and the environment. Using the Clausuis-Clapeyron equation to linearize the the saturation specific humidity about the plume temperature, and assuming entrainment acts only above the cloud base z_b we have that

$$\Delta T(z) \simeq \frac{\epsilon(1-\mathcal{R}_e)}{1 + \frac{L_v}{R_v T^2}\frac{L_v q_{ve}^*}{c_p}} \int_{z_b}^{z} \frac{L_v q_{ve}^*}{c_p}\, dz', \tag{2.4}$$

where R_v is the gas constant for water vapor.

The parcel buoyancy is proportional to ΔT, and so equation (2.4) provides a basis to reason about the behavior of undilute parcel buoyancy and CAPE in an atmosphere that is neutrally buoyancy with respect to an entraining plume. According to (2.4), the buoyancy of undilute ascent is proportional to the entrainment rate and the relative humidity deficit of the environment $(1 - \mathcal{R}_e)$. Furthermore, as the surface temperature is increased, the integrand in (2.4) increases in proportion to the mean saturation specific humidity of the troposphere, resulting in larger undilute buoyancy values. At high surface temperatures, the denominator in (2.4) also plays a role and slows the growth of undilute buoyancy with temperature.

The simple plume model described above highlights the effect of entrainment of dry tropospheric air on the temperature structure of the atmosphere in the zero cloud-buoyancy limit. In what follows we use a more detailed version of the plume model that takes into account the effects of water on the heat capacity and density of air. The plume equations are integrated upwards assuming neutrality with the environment to give a prediction for the vertical profile of environmental temperature which can then be used to calculate CAPE. To crudely account for the bulk effects of many clouds detraining at different levels, we use an entrainment profile of the form $\epsilon(z) = \hat{\epsilon}/z$ (e.g., Holloway and Neelin, 2009), while still assuming that entrainment is zero below

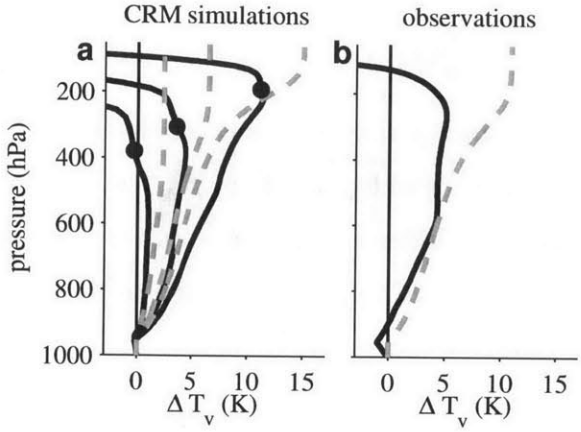

Figure 2-2: Difference in virtual temperature, ΔT_v, between pseudo-adiabatic parcel ascents and (a) CRM profiles or (b) observed profile (solid) compared with the prediction of ΔT_v from the zero-buoyancy plume model (dashed). In (a) profiles are based on the time and domain mean of CRM simulations with SSTs of 286 K, 297 K and 309 K (left to right). The LNB is the level at which $\Delta T_v = 0$ in the upper troposphere; the zero-buoyancy plume model does not predict an LNB. Black dots mark the anvil detrainment level as measured by the level of maximum mean ice concentration in the simulations. In (b) the observational profile is based on the mean over soundings that fall into the red box in Figure 2-3a, and the parcel and plume are initialized at 1000 hPa.

cloud base (identified here as the lifted condensation level). The other inputs to this zero-buoyancy plume model are the near-surface temperature and specific humidity, and a nominal value for the tropospheric environmental relative humidity. Further details are given in the supplementary information (section 2.6).

2.3.2 Application to CRM simulations

The zero-buoyancy plume model reproduces the quasi-exponential increase in CAPE with SST simulated by the CRM (Figure 2-1a). The plume is initialized with the mean temperature and specific humidity of the lowest model level, and, for simplicity, the environmental relative humidity is taken as 80% at all temperatures and heights. (The free tropospheric relative humidity in the simulations depends on altitude, but does not vary greatly from this value.) The zero-buoyancy plume estimate of the environment virtual temperature is only valid up to levels at which convection occurs,

and it is always less than that of an undilute parcel. As a result, the zero-buoyancy plume model does not predict the height of the LNB; we instead take as given the LNB diagnosed from the simulations when using the zero-buoyancy plume model to estimate CAPE. The entrainment parameter is set to $\hat{\epsilon} = 0.75$ in order to provide a good overall fit in Figures 2-1 and 2-2. According to the zero-buoyancy plume model, the increase of CAPE with SST in the CRM simulations is largely explained by the combined effects of the increase in the height to which convection extends and the increase in the saturation deficit of the atmosphere leading to more effective reduction of buoyancy by entrainment of dry air. The slight overestimate of CAPE by the zero-buoyancy plume model shown in Figure 2-1a relates to the LNB being higher than the anvil detrainment level (shown by the dots in Figure 2-2a) and consequently the assumption of neutral buoyancy not being satisfied at all levels up to the LNB in the integral used to calculate CAPE. Better agreement is found if the upper limit of the CAPE integral is alternatively taken as the level of anvil detrainment in each simulation (Figure 2-1b).

The results are qualitatively similar for reversible CAPE and no fallout in the zero-buoyancy plume model, although in this case the entrainment parameter must be reduced to $\hat{\epsilon} = 0.5$ to give a good fit to the CRM results (Figure 2-7) and the buoyancy profiles are somewhat better captured in the upper troposphere (Figure 2-8). Overall, the increase in CAPE predicted by the zero-buoyancy plume model is slightly smaller than found in the CRM simulations (regardless of assumptions regarding fallout), and this may indicate that the entrainment rate itself increases with temperature. Nevertheless, the quasi-exponential character of the increase in CAPE can be accounted for assuming a fixed entrainment profile.

2.4 Radiosonde observations

Since the representation of entrainment in the CRM may not be adequate, we also make a comparison of the zero-buoyancy plume model with radiosonde observations from the tropical western Pacific. To minimize the influence of local boundary-layer

fluctuations, we do not consider CAPE based on a surface parcel, but rather CAPE*, which is defined as the integrated buoyancy of a saturated (undilute) parcel lifted pseudo-adiabatically from 850 hPa to 400 hPa. A fixed upper limit is used to allow for a simple comparison with the zero-buoyancy plume model; the value of 400 hPa is chosen to be below the cloud top in the observations and all of the CRM simulations. Neutrality to an entraining plume can only be expected when the atmosphere is convective, and in the case of the observations the prediction from the zero-buoyancy plume model should be an upper bound on CAPE*. According to the zero-buoyancy plume model, the upper bound on CAPE* will be higher for a drier atmosphere (greater saturation deficit).

2.4.1 Data

We use temperature and humidity soundings from the level b1 dataset of the US Department of Energy Atmospheric Radiation Measurement (ARM) research sites in the tropical western Pacific (Mather et al., 1998). The ARM data archive contains twice daily, high vertical resolution radiosonde soundings from three stations [Darwin (12.4S,130.9E), Manus Island (2.1S,147.5E), Nauru (0.5S,166.9E)] over the period April 2001 to March 2013. The data are processed in three steps: (1) The soundings are linearly interpolated in pressure onto a uniform grid with a spacing of 5 hPa. Values requiring interpolation between levels more than 20 hPa apart are labeled as missing. (2) Soundings with surface temperatures outside the range 288 K – 313 K are considered to be erroneous and are discarded. Furthermore, temperatures at any level more than five standard deviations from the median profile of the resulting subset of soundings are labeled as missing. Any soundings with missing values between 900 hPa and 200 hPa are discarded. (3) Finally, a 1-2-1 temporal filter is applied to ensure the profiles are representative of the atmosphere over a time-scale sufficiently long for convective quasi-equilibrium to hold (effectively averaging between daytime and nighttime soundings). The result of this procedure is 19 700 temporally smoothed atmospheric profiles of temperature and humidity which we use in the analysis below.

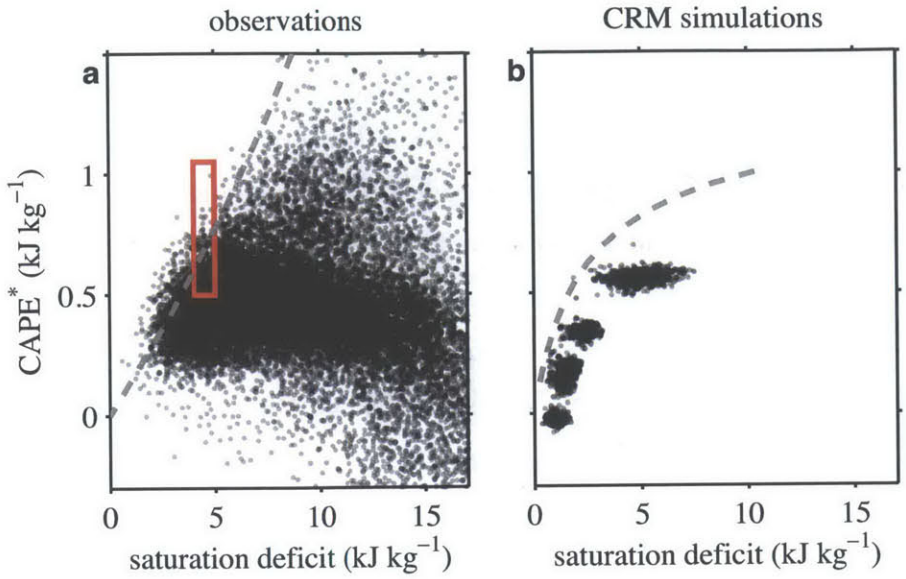

Figure 2-3: CAPE* for the pressure range 850 hPa – 400 hPa plotted against the mean saturation deficit over the same layer for (a) radiosonde observations in the tropical western Pacific and (b) grid-point columns in the CRM simulations. The saturation deficit ($q_v^* - q_v$) is averaged with mass weighting and multiplied by $L_{v0} = 2.501 \times 10^6$ J kg^{-1} to convert it to energy units. Gray dashed lines correspond to values obtained from the zero-buoyancy plume model with entrainment parameter $\hat{\epsilon} = 1.5$. In (a) the plume is initialized at saturation with the median temperature of the soundings at 850 hPa and the environmental relative humidity is varied over the range 20% – 100%. In (b) the plume is initialized at saturation with temperatures in the range 261 K – 303 K, and the environmental relative humidity is fixed at 80%.

2.4.2 Results and comparison to CRM simulations

Figure 2-3a shows the CAPE* based on the pressure range 850 hPa – 400 hPa plotted against the mean saturation deficit over the same pressure range for each sounding. There is a considerable spread of points, but the upper left corner is almost completely devoid of soundings, with a strong gradient in the density of points delineating the boundary of this "forbidden" region. There appears to be a limit to the degree of instability that can be maintained in the atmosphere as measured by CAPE*, and the value of CAPE* associated with this limit depends on the mid-tropospheric saturation deficit such that drier soundings are associated with higher values of CAPE*.

The gray dashed line in Figure 2-3a shows the position on the scatter plot given by the zero-buoyancy entraining plume model for a range of environmental relative

humidities (20% – 100%) and initialized with the median temperature of the soundings at 850 hPa and assuming saturation. Relative humidity variations are the major contributor to variations in saturation deficit in the observed soundings (in contrast to the large temperature changes between the CRM simulations). The zero buoyancy plume model gives a reasonable prediction for the upper bound on CAPE* for a given saturation deficit, although a larger entrainment parameter ($\hat{\epsilon} = 1.5$) is needed as compared to that used in Figures 2-1 and 2-2 ($\hat{\epsilon} = 0.75$) since we are now considering the upper bound on CAPE* rather than the mean CAPE.

A similar scatter plot for the CRM simulations is shown in Figure 2-3b. Here, the points correspond to vertical profiles at grid-point columns in the model. The profiles are spaced 7 km apart in the horizontal and smoothed with a 1-2-1 filter in time using snapshots 12 hours apart. There is less scatter for the simulations compared to the observations because the simulations are of RCE with no large-scale forcing that can stabilize the atmosphere. The clusters of points correspond to simulations with similar SSTs (c.f. Figure 2-1). The prediction from the zero-buoyancy plume model is also shown and gives a reasonable estimate of the upper limit on CAPE* in the simulations. In this case, the zero-buoyancy plume model is initialized with temperatures in the range 261 K – 303 K at 850 hPa (assuming saturation), and with an environmental relative humidity of 80%. Importantly, the same entrainment parameter ($\hat{\epsilon} = 1.5$) is used to match the upper bound on CAPE* for both the observations (Figure 2-3a) and CRM simulations (Figure 2-3b).

To examine the vertical profile of buoyancy contributing to CAPE in the observations, we use a subset of radiosonde soundings with relatively-high CAPE* and a relative humidity of roughly 80% that is typical of the CRM simulations. The subset is shown by the red box in Figure 2-3a and includes soundings with CAPE* greater than 500 J kg^{-1} and mean saturation deficits (averaged from 850 hPa – 400 hPa) between 1.6 g kg^{-1} and 2 g kg^{-1}. The difference in virtual temperature between a pseudo-adiabatic parcel ascent and the mean of this subset of soundings is shown in Figure 2-2b, together with the prediction from the zero-buoyancy plume model. The parcel and plume are initialized with the mean temperature and specific humidity at

1000 hPa, and the same entrainment parameter ($\hat{\epsilon} = 0.75$) and environmental relative humidity ($\mathcal{R}_e = 80\%$) is used in the plume as was used in the application to the CRM in Figure 2-2a. The zero-buoyancy plume model reproduces the magnitude of the observed buoyancy in the lower troposphere, but over-estimates it in the upper troposphere. This may be partly due to the assumption of total precipitation fallout in the zero-buoyancy plume; the agreement is better when no precipitation fallout is allowed in the plume or parcel ascent (Figure 2-8).

Overall, the observational results provide support for the CRM simulations and conceptual model discussed here in which lapse rates and CAPE are affected by the tropospheric saturation deficit.

2.5 Conclusions

We have shown that CAPE increases rapidly with temperature in simulations of RCE over a wide range of SSTs, implying a systematic deviation of the thermal stratification from that of an undilute moist adiabat. The increase in CAPE with SST was accounted for using a conceptual model in which the atmosphere is assumed to be neutrally buoyant with respect to an entraining plume. According to this conceptual model, both the increase in saturation deficit of the troposphere and the increase in height of convection contribute to the increase in CAPE, without the need to invoke a change to the entrainment rate.

Radiosonde observations were used to provide support for the CRM simulations and conceptual model: a measure of CAPE for saturated parcels lifted from 850 hPa to 400 hPa was found to have an upper bound that depends on saturation deficit, and this upper bound could be reproduced by the zero-buoyancy plume model. Importantly, the same entrainment parameters were found to be applicable to both the CRM simulations and the radiosonde observations, despite the difficulty in representing entrainment processes in model simulations.

Further work is needed to understand how our results for RCE relate to changes in CAPE and tropical lapse rates in simulations of the global climate. For small

temperature changes, the zero-buoyancy plume model is consistent with the "vertical shift transformation" described in chapter 5 which has recently been shown to account for much of the inter-model scatter in the response of upper-tropospheric lapse rates to global warming (O'Gorman and Singh, 2013). Climate-model simulations feature increases in CAPE in the tropics (Sobel and Camargo, 2011; Fasullo, 2012) and increases in the convective contribution to moist available potential energy in the extratropics (O'Gorman, 2010), but both of these increases could be influenced by changes in horizontal temperature gradients and circulations in addition to the factors controlling CAPE in RCE.

In our CRM simulations, cloud buoyancy and the vertical velocity of updrafts both increase with SST. Increases in the strength of strong updrafts may be directly tied to the increase in CAPE to the extent that strong updrafts are associated with relatively weak entrainment rates and the distribution of entrainment rates does not change as the SST is increased. However, it is known that cloud updraft velocities may also depend on the microphysics of hydrometeor formation and fallout (Parodi and Emanuel, 2009), and we leave detailed analysis of the changes in cloud buoyancy and updraft velocity to chapter 3.

2.6 Supplementary information

2.6.1 CRM simulations

Here we give more details of the CRM simulations described in section 2.2. Low resolution simulations are first run over a slab ocean to statistical equilibrium with CO_2 concentrations ranging from 1 ppmv to 1280 ppmv (Fig. 2-5). The slab ocean has a depth of 1 m and is assumed to be infinitely conducting such that it has a single temperature over the whole domain. Equilibrium is considered to be reached if the trend in SST over the last 50 days of the simulation is less than 1 K yr^{-1}. The slab-ocean simulations are performed with a horizontal grid-spacing of 2 km in a doubly periodic 80×80 km domain. The time-mean SST of the last 50 days of

each slab-ocean simulation is then used as a fixed surface boundary condition for higher resolution simulations (1 km horizontal grid spacing, 84×84 km domain) with the corresponding CO_2 values. These simulations equilibrate much faster because the SST is fixed and because the simulations are initialized with the mean state of the slab-ocean simulations. The total atmospheric energy and water vapor reach their equilibrium values in 10 - 20 days (Figure 2-4). The fixed-SST simulations are run for 40 days; statistics collected over the last 20 days are used for the results in this chapter. A subset of the simulations were also performed using a horizontal grid spacing of 0.5 km, and the results are found to be insensitive to horizontal grid spacing over the range 0.5 km – 2 km.

The slab ocean simulations at the two highest SSTs are affected by a form of convective self-aggregation which tends to decrease SST. The corresponding fixed-SST simulations do not show evidence of aggregation, and our results are not expected to be substantially affected by this issue[2].

2.6.2 Description of zero-buoyancy entraining plume model

In this section we give a detailed description of the zero buoyancy plume model used in sections 2.3.2 and 2.4. We consider a steady entraining plume as a bulk representation of an ensemble of cumulus clouds (e.g., Tiedtke, 1989). Neglecting kinetic energy and assuming hydrostasy, we may write the governing equations for the plume in terms of the conserved variables (in the absence of precipitation fallout) moist-static energy h and total water mass fraction q_t as

$$\frac{dh}{dz} = -\epsilon(h - h_e), \tag{2.5}$$

$$\frac{dq_t}{dz} = -\epsilon\left(q_t - q_{ve}\right). \tag{2.6}$$

Here z is height, ϵ is the entrainment rate (in units of inverse length), the subscript e refers to the environment, and h and q_t are expressed per unit total mass of moist

[2]In later chapters of this thesis we do not use results based on these aggregated simulations; they are included here to be consistent with the published version of this chapter.

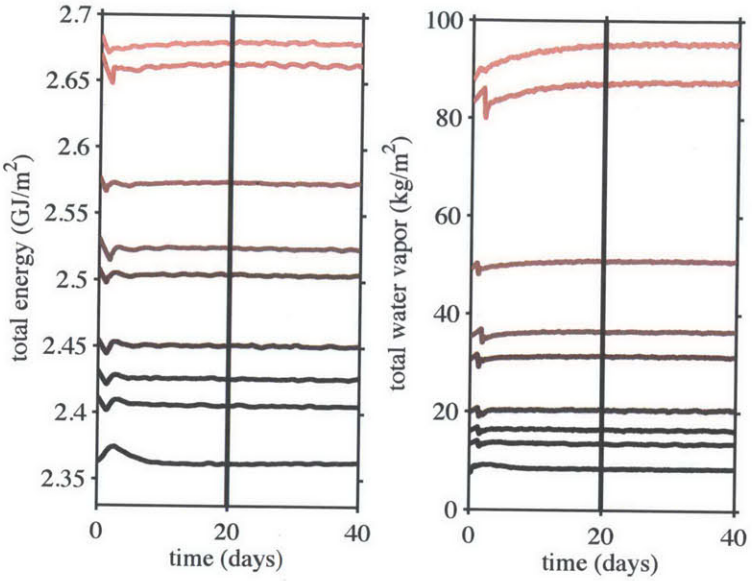

Figure 2-4: Timeseries of total atmospheric energy (left) and water vapor (right) for fixed-SST simulations with the CRM. The vertical black line corresponds to the time at which the collection of statistics begins.

air. The moist static energy is defined as

$$
\begin{aligned}
h &= (1-q_t)h_d + q_v h_v + q_l h_l + q_i h_i, \\
h_d &= c_{pd}(T - T_0) + gz, \\
h_v &= c_{pv}(T - T_0) + gz + L_{v0}, \\
h_l &= c_l(T - T_0) + gz, \\
h_i &= c_i(T - T_0) + gz - L_{f0},
\end{aligned}
$$

where T is the temperature, g is the gravitational acceleration, and the constants L_{v0} and L_{f0} are the latent heats of vaporization and fusion, respectively, at the reference temperature T_0. The total water mass fraction q_t has components associated with vapor (q_v), liquid (q_l), and ice (q_i). The isobaric specific heat capacity of dry air and water vapor are given by c_{pd} and c_{pv}, while liquid water and ice are treated as incompressible, with specific heat capacities c_l and c_i respectively. All constants are taken as the values used in the CRM and are given in table 2.1.

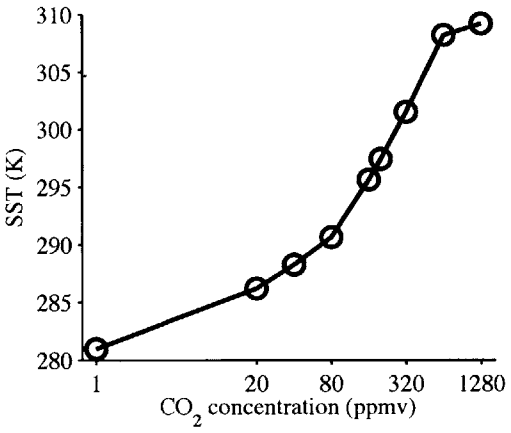

Figure 2-5: Equilibrium SSTs in CRM simulations of RCE with a slab ocean and varying CO_2 concentration. CO_2 concentration is shown on a log scale.

Equations (2.5) and (2.6) assume no fallout of precipitation, and this form of the zero-buoyancy plume model is used when considering reversible CAPE (Fig. 2-7 and Fig. 2-8). However, the default version of the zero-buoyancy plume model assumes complete fallout of all liquid and solid water from the plume. Fallout is applied in a separate step in which all liquid and solid water is removed, and the moist static energy is recalculated at constant pressure and temperature.

As in the CRM, the saturation vapor pressure e^* is written as a combination of the saturation vapor pressure over liquid (e_l^*) and ice (e_i^*) according to

$$e^*(T) = \zeta(T)e_l^*(T) + (1 - \zeta(T))e_i^*(T),$$

where $\zeta(T)$ increases linearly in temperature from zero to one between 233.15 K and 273.15 K. At saturation, the phases of water are divided according to

$$\begin{aligned} q_v &= q_v^*, \\ q_l &= \zeta(q_t - q_v^*), \\ q_i &= (1 - \zeta)(q_t - q_v^*), \end{aligned}$$

where q_v^* is the saturation specific humidity.

Table 2.1: Thermodynamic constants used in the CRM and zero-buoyancy plume model.

Symbol	Value	Units
g	9.81	m s^{-2}
c_p	1005.7	J kg^{-1} K^{-1}
c_{pv}	1870.0	J kg^{-1} K^{-1}
c_l	4190.0	J kg^{-1} K^{-1}
c_i	2106.0	J kg^{-1} K^{-1}
R_d	287.04	J kg^{-1} K^{-1}
R_v	461.50	J kg^{-1} K^{-1}
L_{v0}	2.501×10^6	J kg^{-1}
L_{f0}	2.069×10^5	J kg^{-1}
T_0	273.15	K

The plume model is solved in the zero-buoyancy limit in which the plume is exactly neutrally buoyant with respect to the environment. [In this limit (2.5) and (2.6) may also be obtained by applying the parcel model of Romps and Kuang (2010a) to a steady, vertically oriented flow with no precipitation fallout.] The inputs are the entrainment rate profile, the temperature and specific humidity near the surface (or at 850hPa in section 2.4), and a nominal value of the environmental relative humidity. Equations (2.5) and (2.6) are integrated upwards to solve for the environmental temperature. The integration is performed using forward differences with a step size of 50 m. At each step, the temperature and humidity of the plume are calculated from h and q_t. If fallout is specified, the liquid and solid water are removed as described above. The environmental temperature is then calculated by assuming the density of the plume and environment are equal and using the environmental relative humidity as given.

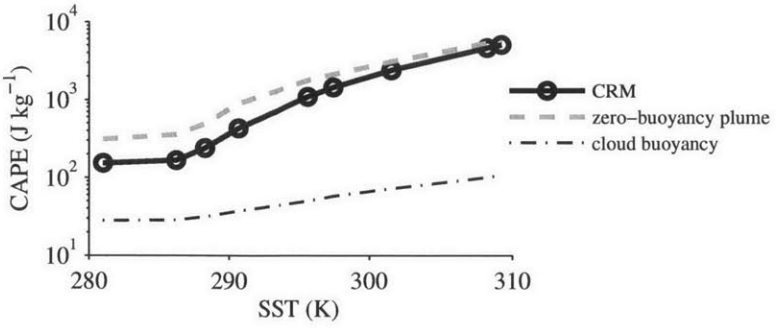

Figure 2-6: As in Figure 2-1a, but plotted with a logarithmic scale for the ordinate.

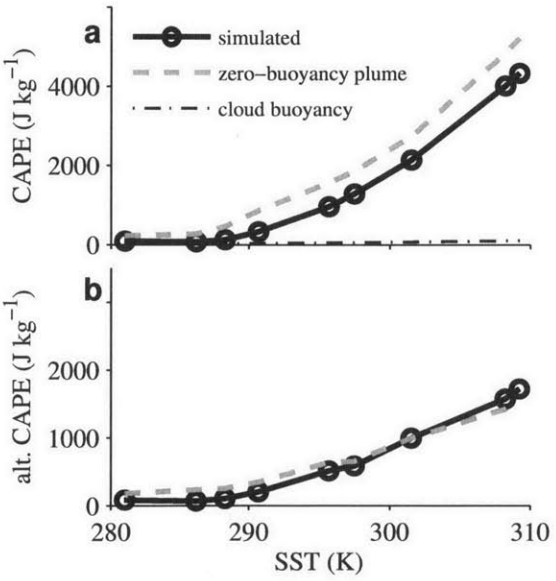

Figure 2-7: As in Figure 2-1, but for reversible CAPE, no precipitation fallout in the zero-buoyancy plume model, and an entrainment parameter of $\hat{\epsilon} = 0.5$.

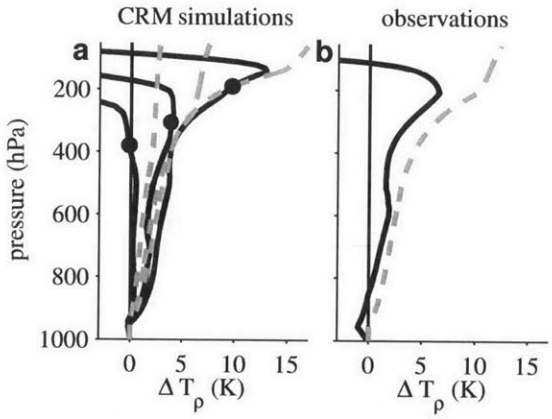

Figure 2-8: As in Figure 2-2, but for a reversible parcel ascent, no precipitation fallout in the zero-buoyancy plume model, and an entrainment parameter of $\hat{\epsilon} = 0.5$. Density temperature difference, ΔT_ρ, is shown rather than virtual temperature difference because the reversible parcel contains some condensate. The subset of soundings used in (b) is the same as that used for figure 2b.

Chapter 3

Increases in moist-convective updraft velocity with warming in radiative-convective equilibrium

3.1 Introduction

The updraft velocity in moist convection is important in determining the precipitation rates of convective clouds (Muller et al., 2011) and the lightning frequency in thunderstorms (e.g. Baker et al., 1999), and it may influence cloud microphysical properties (Del Genio et al., 2005; Morales and Nenes, 2010). However, cloud updrafts are not resolved by general circulation models (GCMs), and GCM-based predictions of future changes to the distribution of updraft velocity must rely on results derived from large-scale fields alone (Del Genio et al., 2007). An important question, therefore, is to what degree GCM grid-scale quantities, such as the large-scale stratification, may be used to infer possible changes to convective updraft velocity as a result of global warming.

Idealized studies of radiative-convective equilibrium (RCE) have found that moist-convective updraft velocity increases as the atmosphere warms (Romps, 2011; Muller et al., 2011). These studies with resolved convection, along with other studies with

parameterized convection (Sobel and Camargo, 2011; Fasullo, 2012) also find increases in convective available potential energy (CAPE) with warming. In chapter 2, we attributed the CAPE increase with warming in RCE to the increased effectiveness of entrainment at higher temperature. We constructed a model of a convective ensemble in which the clouds, as represented by a bulk entraining plume, remain neutrally buoyant with respect to the environment. The argument for increasing CAPE with warming proceeds as follows: at a fixed relative humidity, the saturation deficit of the troposphere increases with warming. This allows a given amount of entrainment to have a larger effect in reducing the plume temperature and, by the zero buoyancy assumption, alters the environmental lapse rate away from that of a moist adiabat.

But, the neglect of the cloud buoyancy precludes the use of the arguments outlined in chapter 2 to reason about updraft velocity. Additionally, the magnitude of the vertically integrated cloud buoyancy (the buoyancy integral) and its fractional increase with warming were found to be considerably smaller than the values implied by the CAPE in RCE simulations. We thus have some understanding of the reason for the increase in CAPE with warming, but it is unclear whether this can explain the coincident increase in updraft velocity in cloud-resolving simulations.

Previous studies have attempted to construct theories of convective updraft velocity using constraints on frictional dissipation derived from the entropy budget (Emanuel and Bister, 1996; Rennó and Ingersoll, 1996). As pointed out by Pauluis and Held (2002a), however, irreversible sources of entropy due to moist processes dominate the entropy budget of the atmosphere, complicating efforts to constrain the frictional dissipation rate. More recent work has suggested that the effects of cloud and precipitation microphysics may play a role in determining the updraft velocity in moist-convective clouds (Parodi and Emanuel, 2009). These microphysical effects are sensitive to temperature changes (see chapter 4) and may also contribute to changes in updraft velocity as the atmosphere warms.

Our aims in this chapter are threefold: 1) to document the scaling of moist-convective updraft velocity in RCE over a wide range of surface temperatures, 2) to determine the extent to which changes in large-scale fields, in particular the mean

stratification, may be used to estimate changes to the convective updraft velocity, and 3) to understand the possible reasons that CAPE and buoyancy integral increase at different fractional rates with warming as reported in chapter 2 of this thesis.

We conduct simulations of RCE using a cloud-system resolving model (CRM) over different surface temperatures and find substantial increases in the simulated updraft velocity and cloud buoyancy with warming, particularly for the most intense updrafts. The increases are reproduced by an entraining plume model in which the environment is represented by the mean profile in the simulations, and the entrainment and microphysical parameters are held fixed as the atmosphere warms. The plume results suggest that changes to the mean stratification of the troposphere play a leading role in governing the response of the simulated buoyancy and updraft velocity to warming, despite the lack of proportionality between CAPE and the buoyancy integral.

The relative scaling of the buoyancy integral and CAPE are investigated further using a generalization of the zero-buoyancy plume model introduced in chapter 2. We extend the zero-buoyancy plume model to include two plumes, with one plume representing the most intense updrafts and the second plume representing the bulk of the convective mass flux. As in chapter 2, the environmental lapse-rate is derived by assuming the bulk plume is neutrally buoyant with respect to the environment. Under the assumption that the entrainment rates of the plumes and the tropospheric relative humidity remain fixed as the surface temperature is varied, the two-plume model predicts large fractional increases in CAPE, and more modest fractional increases in the buoyancy integral. Based on these results, we argue that the different scaling of the buoyancy integral with temperature compared to that of CAPE in our simulations may be a result of entrainment processes affecting both the mean stratification and the buoyancy of the most intense updrafts.

The rest of this chapter is organized as follows: We first describe the simulations conducted (section 3.2) and the results for cloud buoyancy and updraft velocity (section 3.3). We then interpret the scaling of cloud buoyancy and updraft velocity using an entraining plume model in which the plume environment is given (section 3.4), before incorporating the environmental lapse rate into the plume solution via

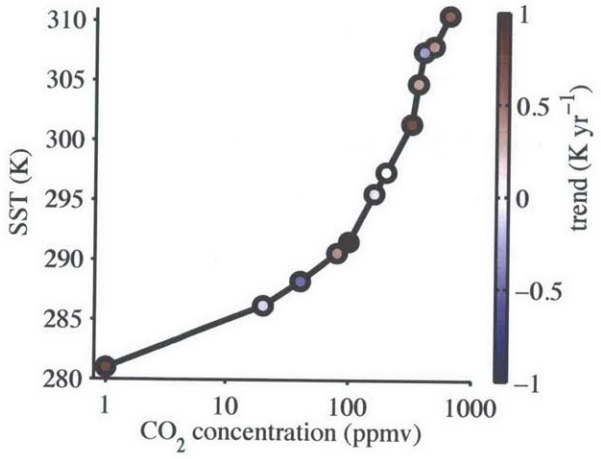

Figure 3-1: Equilibrium SST for the slab-ocean simulations as a function of the imposed CO_2 concentration. The equilibrium is defined as the mean over the last 50 days of each simulation and colors represent the trend in slab-ocean temperature over this period.

a generalization of the zero-buoyancy plume model (section 3.5). Finally, we recap the main findings and discuss potential implications of this work for convection in a warming atmosphere (section 3.6).

3.2 Simulations of radiative-convective equilibrium

3.2.1 Model configuration

The model configuration used is identical to that described in the previous chapter. We use a model similar to version 16 of the Bryan Cloud Model (Bryan and Fritsch, 2002), with minor alterations described in the appendix; further details may be found in section 2.2

A series of simulations with imposed CO_2 concentrations ranging from 1 to 640 ppmv are conducted over a slab ocean until equilibrium is reached[1]. The slab ocean

[1]This is the same series of slab-ocean simulations described in the previous chapter, but here, and in all other chapters, we have neglected the 1280 ppmv simulation which was affected by a form of weak convective aggregation. Additionally, we have extended the 640 ppmv simulation such that it reaches a new, warmer equilibrium in which there is no evidence of convective aggregation.

has a uniform temperature and a depth of one meter. While this is considerably shallower than the ocean mixed layer, the single temperature of the slab ensures it responds only to the domain-integrated net flux of energy at the surface, and that it is insensitive to cloud-scale anomalies in surface radiative and turbulent fluxes (Romps, 2011). The slab-ocean simulations equilibrate with sea-surface temperatures (SSTs) in the range 281 - 311 K (Figure 3-1). Here, equilibration is defined as occurring when the magnitude of the ocean temperature trend for the last 50 days of the simulation is less than 1 K yr^{-1}. The equilibration timescale for slab-ocean simulations of RCE is as long as a few hundred days (Cronin and Emanuel, 2013). In order to integrate the model for such long time periods, the slab-ocean simulations are run in a low-resolution, small-domain configuration with a horizontal grid-spacing of 2 km and a domain 80 $\times$ 80 km in size.

A subset of the slab-ocean simulations are repeated at higher horizontal resolution (grid spacing 0.5 km) and with a larger domain size (160$\times$160 km) by fixing the SST to the equilibrated value of the corresponding low-resolution simulation. Snapshots of three of these simulations are shown in Fig. 3-2. The high-resolution simulations are initialized with the equilibrium temperature and humidity profiles of the low-resolution simulations and run for 30 days, with statistics collected at hourly intervals over the last 10 days (Fig. 3-3). The fixed-SST boundary condition allows the high-resolution simulations to come to equilibrium more rapidly than the slab-ocean simulations, but it also implies that the high resolution simulations are not energetically closed. While they have the same CO_2 concentration as the corresponding slab-ocean simulation, top-of-atmosphere energy imbalances of the order of a few watts per meter squared remain in the high-resolution simulations even at equilibrium. These small imbalances are not likely to strongly affect the updraft velocity or cloud-buoyancy that are our primary interest here. In the rest of this chapter, we focus on results from the high-resolution simulations, since these simulations are better able to resolve cloud updrafts, but the conclusions are not altered significantly by considering the low-resolution, slab-ocean simulations.

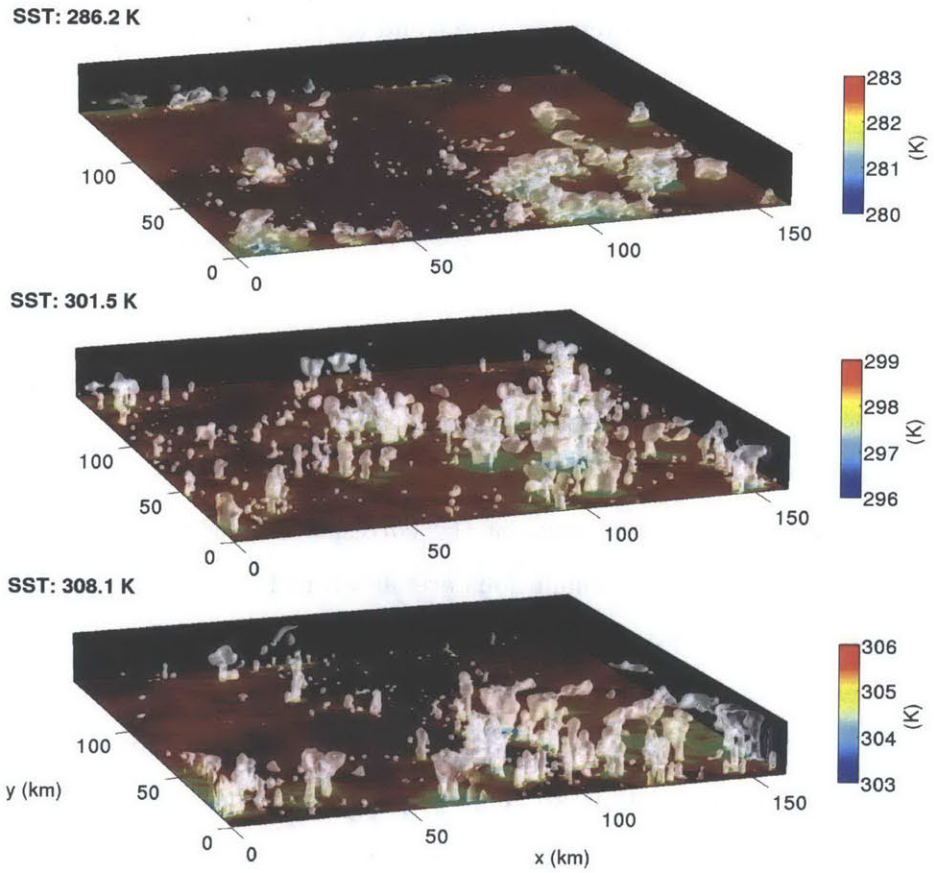

Figure 3-2: Snapshot of high-resolution simulations of RCE with CO_2 concentrations of (top) 20, (middle) 320 and (bottom) 480 ppmv, and SST fixed to values given. Colors represent temperature of the lowest model level, while white shading represents an isosurface of condensed water concentration (including hydrometeors) of 0.1 g m^{-3}.

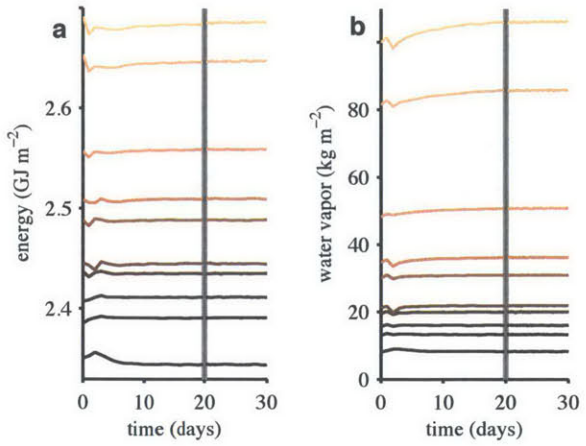

Figure 3-3: Time series of total atmospheric energy (left) and water vapor (right) per unit area for high-resolution fixed-SST simulations. The vertical gray lines correspond to the time at which the collection of statistics begins.

3.2.2 Mean temperature and cloud fraction

Here, we briefly highlight some general features of the simulations that are of relevance to later sections before we describe the results for updraft velocity in section 3.3. Figure 3-4a shows domain- and time-mean temperature profiles from four of the high-resolution simulations described above. As the surface temperature is increased, the tropospheric lapse-rate decreases, consistent with the behavior of moist-adiabatic ascent from the boundary layer. However, the increase in mean static stability in the simulations is not as rapid as for a moist adiabat; the simulated temperature profiles show a systematic deviation from moist-adiabatic lapse rates. These deviations were analysed in similar simulations of RCE in chapter 2 from the perspective of the CAPE. We consider the implications of these lapse-rate changes for the cloud buoyancy and updraft velocity in section 3.4.

The fixed anvil temperature hypothesis, introduced by Hartmann and Larson (2002) suggests that the detrainment level of deep convective clouds should remain at a relatively constant temperature as the surface temperature is varied. This hypothesis was tested in simulations of RCE at surface temperatures typical of Earth's tropics (299.65 - 305.65 K) by Kuang and Hartmann (2007), and here it is shown

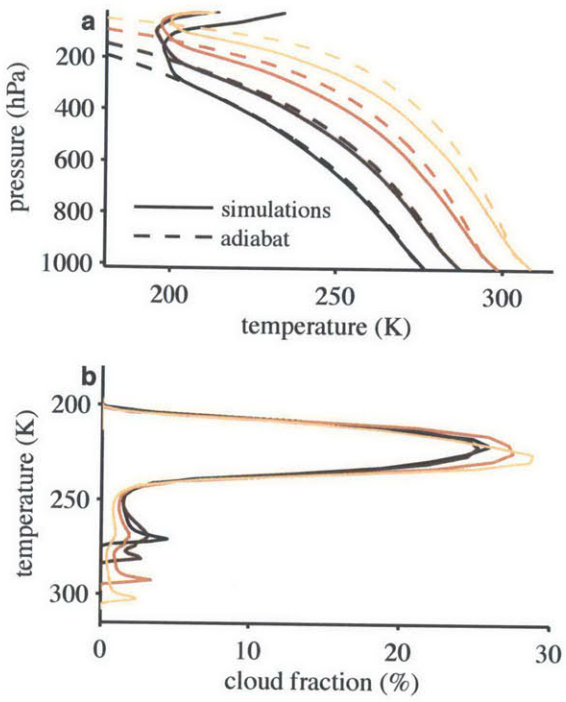

Figure 3-4: Properties of high-resolution simulations with SSTs of 281 (black), 291, 302 and 311 K (orange). (a) Domain- and time-mean temperature plotted as a function of pressure in each simulation (solid), and the temperature of a reversible parcel ascent initialized with the mean properties at the lowest model level in the corresponding simulation (dashed). (b) Mean cloud fraction plotted against mean temperature in the simulations. Cloudy grid points are defined as those with a cloud-water concentration greater than 0.01 g kg^{-1}.

to hold over a much wider range of surface temperatures. [See also the earlier work of Tompkins and Craig (1999) and the recent study of rotating RCE by Khairoutdinov and Emanuel (2013).] The cloud anvil level, as measured by the maximum in mean cloud fraction in the simulations, shifts upwards in such a way as to remain at a remarkably constant temperature of roughly 220 K for all surface temperatures simulated (Fig. 3-4b). The vertical shift transformation (VST) that will be described in chapter 5 also predicts an upward shift of the circulation with warming. While the VST is not directly applied to the cloud distribution in chapter 5, to the extent that cloud variables are related to local values of the circulation and relative humidity it would predict a slight decrease in the cloud anvil temperature with increasing surface

temperature. But in the simulations, the anvil temperature increases slightly, particularly for the simulation with the highest surface temperature shown. This slight increase in cloud-anvil temperature may be a result of the radiative influence of ozone on the upper tropospheric heat balance in the warmest simulations. The ozone profile is fixed across the simulations, and as the depth of convection increases, more of the total column ozone exists within the troposphere rather than in the stratosphere above. Notwithstanding these small differences, the approximate invariance of the cloud anvil temperature with increasing surface temperature across the simulations allows for a simple estimate of the depth of convection as extending to the 220 K isotherm regardless of the surface temperature.

3.3 Updraft velocity and cloud buoyancy

Fig. 3-5 shows profiles of the 99.99th percentile of vertical velocity (including all points) in a number of the simulations of RCE. This measure of the vertical velocity increases as the surface warms, although the increase is not uniform with height, but rather occurs primarily in the upper troposphere. The peak value of the profiles shown in Fig. 3-5, which we denote w_{max}, increases with warming by roughly a factor of two over the range of surface temperatures simulated. The fractional increase at a fixed pressure in the lower troposphere is somewhat weaker, while at levels below 900 hPa the vertical velocity, as measured by the 99.99th percentile of the distribution, is essentially unchanged. The increase in the peak vertical velocity also depends on the percentile chosen. The peak value of a higher percentile (99.999th) vertical velocity profile increases by a factor of 2.5 over the range of surface temperatures simulated, while for a lower percentile (99.9th) the peak vertical velocity increases by only a factor of 1.2.

To help understand the simulated increase in updraft velocity with warming, we consider various measures of buoyancy in the simulations. The buoyancy of an undilute parcel lifted from the surface may be measured by the CAPE. Here we calculate the CAPE as the integral of the positive buoyancy of a reversible parcel ascent up to

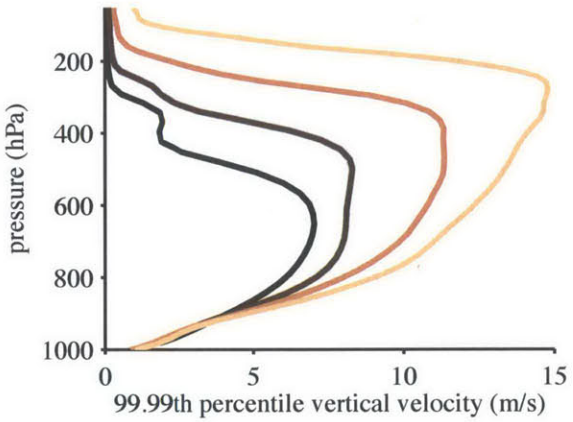

Figure 3-5: 99.99th percentile of vertical velocity in high-resolution simulations with SSTs of 281 (black), 291, 302 and 311 K (orange). The 99.99th percentile of the vertical velocity distribution is calculated at each level in each simulation, and the results are plotted as a vertical profile.

its level of neutral buoyancy. For each simulation, the parcel buoyancy is taken with respect to the domain- and time-mean virtual temperature profile, and the parcel is initialized with the mean properties at the lowest model level.

As found in chapter 2, the CAPE increases substantially with temperature, with its value in the warmest simulation being roughly a factor of forty greater than its value in the coldest simulation (Fig. 3-6a). The CAPE is also considerably larger in magnitude than a similar measure based on the simulated buoyancy of clouds. We define the buoyancy integral as the vertical integral of the 99.99th percentile of buoyancy at each level in the simulations. The integral is taken from the surface to a nominal cloud top, defined here as the level at which the mean temperature in the simulation equals 220 K (c.f. Fig. 3-4b). The buoyancy integral increases with warming like the CAPE, but it is nearly an order of magnitude smaller than the CAPE, and its fractional rate of increase is considerably lower than that of the CAPE; it increases by a factor of roughly seven over the range of surface temperatures simulated.

As expected from the application of a simple force balance [cf. equation (3.6)], the buoyancy integral is tightly coupled to the peak kinetic energy (per unit mass) of

updrafts. For example, we may construct a measure of the kinetic energy based on the maximum of the vertical velocity profiles in Fig. 3-5, given by w_{max}^2. A roughly linear relationship exists between the buoyancy integral and w_{max}^2 across the simulations (Fig. 3-6b, circles). A similar, albeit less linear, relationship also holds for alternative measures of the peak kinetic energy and buoyancy integral based on conditional-mean profiles for points within "convective cores" (crosses). Here, convective cores are comprised of all grid points with cloud water content greater than 0.01 g kg^{-1} and an upward velocity greater than 2 m s^{-1}. The buoyancy integral is taken as the integral of the conditional-mean buoyancy profile over all levels where it is defined, and the peak updraft is taken as the maximum in the conditional-mean vertical velocity profile. This measure of the peak updraft gives smaller values than w_{max}, and it increases with warming at a somewhat lower fractional rate than that of w_{max}.

In summary, we have shown that the updraft velocity increases with warming in the RCE simulations, with the largest increases occurring for the most intense updrafts. Additionally, the buoyancy integral appears to be a key parameter determining the peak updraft velocity in the simulations. But the buoyancy integral does not scale with a similar quantity based on an undilute parcel ascent, the CAPE. In the next two sections we seek to understand these results through the conceptual framework of a set of entraining plumes.

3.4 Spectrum of plumes with given environment

3.4.1 Calculation of plume properties

We consider the representation of a convective cloud ensemble by a spectrum of entraining plumes with a range of entrainment rates existing in a given environment. The plume model is written in terms of the vertical profile of moist static energy h

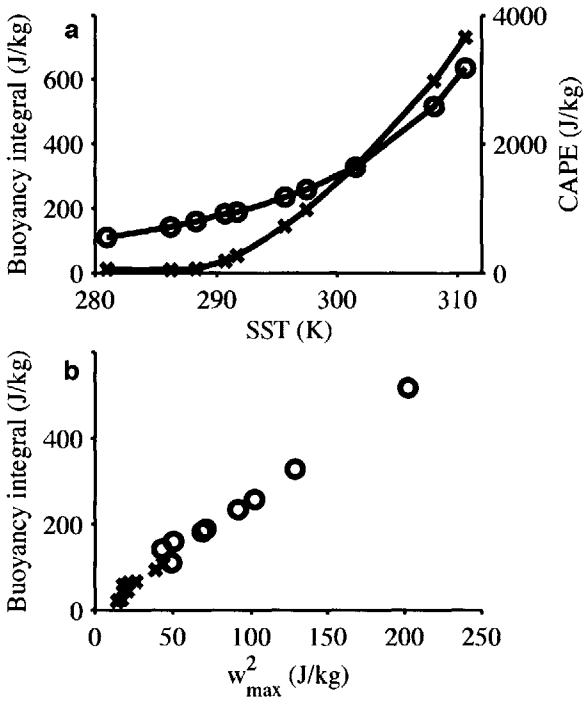

Figure 3-6: (a) Reversible CAPE (right axis, crosses) and buoyancy integral (left axis, circles) in high-resolution simulations as a function of SST. (b) Relationship between peak kinetic energy w^2_{max} and buoyancy integral in the high-resolution simulations (circles). Crosses in (b) correspond to alternate measures of the buoyancy integral and peak kinetic energy calculated based on a conditional mean over grid points within convective cores (see text for details).

and total water mass fraction q_t so that (in the absence of precipitation fallout),

$$\frac{dh}{dz} = -\epsilon(h - h_e), \tag{3.1}$$

$$\frac{dq_t}{dz} = -\epsilon(q_t - q_{ve}). \tag{3.2}$$

Here, ϵ is the height-independent entrainment rate, q_v is the mass fraction of water vapor (specific humidity), z is height, and the subscript e refers to properties of the environment. The moist static energy is defined by

$$h = c_p(T - T_0) + gz + L_v q_v - L_f q_i, \tag{3.3}$$

where c_p is the isobaric specific heat capacity of moist air, T is the temperature, $T_0 = 273.15$ K, g is the gravitational acceleration, L_v and L_f are the latent heats of vaporization and freezing evaluated at T_0, and q_i is the mass fraction of ice.

For each simulation, we calculate vertical profiles of moist static energy and total water mass fraction for a number of plumes with different entrainment rates by integrating equations (3.1) and (3.2) upwards, assuming the environmental properties are equal to those of the time and domain mean in the corresponding simulation. (Further details of the method of solution may be found in section 2.6.)

To account for the effect of boundary layer inhomogeneity, we set the temperature and specific humidity of the plumes at the lower boundary to be equal to one standard deviation above the mean at the lowest model level. For example, the plume temperature at the lower boundary is given by,

$$T = \overline{T} + \sigma_T \tag{3.4}$$

where $\overline{T}$ and σ_T are the mean and standard deviation of the temperature at the lowest model level of the corresponding simulation. A similar equation applies for the specific humidity. This one standard deviation perturbation to the mean properties of the simulations corresponds to a 0.4 – 0.6 K perturbation in virtual temperature with no obvious trend with warming. Including this lower-boundary perturbation within the plume calculation is important to capture the magnitude of the buoyancy of clouds, particularly at low surface temperatures. At surface temperatures characteristic of Earth's tropics and higher, on the other hand, the lower boundary condition plays a smaller role, consistent with recent results for shallow convection (Romps and Kuang, 2010b).

Once the profiles of h and q_t are calculated, we may derive the temperature, buoyancy and condensed water content of the plume given a set of microphysical assumptions. In the calculations to follow, we assume no fallout of condensate in all plume calculations and a mixed phase such that the fraction f of condensate that is ice increases linearly as the temperature decreases from 273.15 K to 233.15 K. The

saturation vapor pressure e^* is then taken to be,

$$e^* = (1 - f)e_l^* + fe_i^*, \tag{3.5}$$

where e_l^* and e_i^* are the saturation vapor pressures over liquid and solid, respectively. This form of the saturation vapor pressure is consistent with that used in the CRM simulations.

Finally, the upward velocity within the plumes $w(z)$, is calculated using a simple vertical velocity equation given by

$$\frac{\partial w^2}{\partial z} = aB - b\epsilon w^2, \tag{3.6}$$

where w is initialized at zero at the lower boundary, B is the buoyancy, and, following Bretherton et al. (2004), we set $a = 1$ and $b = 2$.

3.4.2 Results

We compare the plume spectrum to the simulations by examining the distribution of air parcel properties in the moist static energy-height plane. We calculate the cumulative distribution function of moist static energy at each level based on hourly snapshots from the simulations. Following Kuang and Bretherton (2006) we define the effective entrainment rate at a given point in the moist static energy-height plane as the value of ϵ of a plume passing through that point (see also Pauluis and Mrowiec, 2013). We may then associate different parts of the moist static energy distribution with different effective entrainment rates (Fig. 3-7a,b,c).

In all three simulations shown, the 99.999th percentile of moist static energy has an effective entrainment rate of between 0.1 and 0.2 km^{-1} over a large portion of the troposphere. This high percentile is exceeded by roughly 250 points at each level, and it represents the air parcels with close to the lowest effective entrainment rates at a given level (we show contours up to the 99.9999th percentile). The relatively high value of the effective entrainment rate for these air parcels implies that undilute ascent

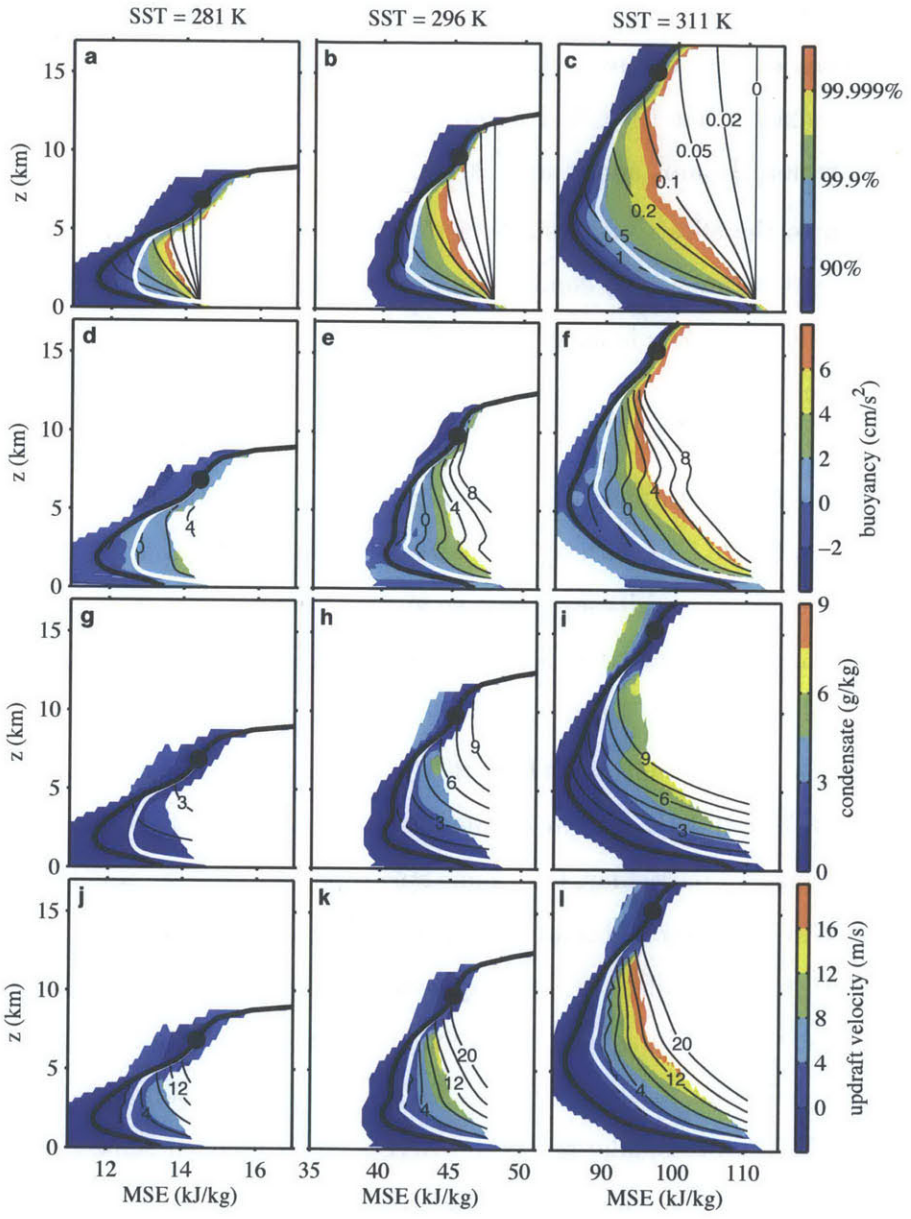

Figure 3-7: Domain- and time-mean moist static energy (black) and saturated moist static energy (white) profiles in three high-resolution simulations of RCE with SSTs of 281 K (left), 296 K (center) and 311 K (right). The black dots represent the level at which the mean temperature is equal to 220 K. (a,b,c) Cumulative distribution function of moist static energy at each level (colors) and profiles of moist static energy for plume calculations with entrainment rates as given in panel (c) in units of km^{-1} (thin black lines). Lower panels show distributions of buoyancy (d,e,f), cloud condensate (g,h,i), and updraft velocity (j,k,l) binned by moist static energy for the simulations (colors) and plume ensemble (thin black lines, units on contours same as color bar). See text for further details.

from the boundary layer is virtually absent in the simulations. This is consistent with the results presented in the previous section showing that the buoyancy integral is substantially smaller than the CAPE, and it is consistent with previous CRM studies of deep convection (Romps and Kuang 2010).

We return to the effective entrainment distributions below, but first we consider the distributions of buoyancy, condensate and updraft properties of parcels in the moist static energy-height plane, shown in the lower panels of Fig. 3-7. These properties are calculated based on hourly snapshots in the simulations and then binned by moist static energy at each level. The bin widths used are identical for each simulation, but the bin width increases with increasing moist static energy. Results are contoured for only the bins with at least forty grid points contributing. Similar distributions of buoyancy, condensate amount and updraft velocity are plotted for the plume spectrum by interpolating the properties of individual plumes in the spectrum to standard values of moist static energy and contouring.

The distributions of buoyancy (Fig. 3-7d,e,f) and to a lesser extent condensate amount (Fig. 3-7g,h,i) derived from the plume spectrum are relatively similar to those of the simulations. In particular, the plume spectrum captures the rough magnitude of the increase in buoyancy and condensate amount with warming for high moist static energy parcels in the simulations. The agreement is not as close for the case of the condensate amount, and in general, the condensate amounts according to the plume spectrum are somewhat too high. This is likely related to the simple assumption of no fallout in the plume calculation; better agreement is found if some precipitation fallout is included (not shown). It should also be noted that, at saturation, the moist static energy fully determines the virtual temperature of a parcel, and thus the buoyancy and condensate amount are not independent when plotted as a function of moist static energy.

The simulated vertical velocity distribution is also well reproduced by the plume spectrum, confirming the tight coupling of the buoyancy and updraft velocity found in the previous section (Fig. 3-7j,k,l). The simplified vertical momentum equation (3.6) roughly reproduces the distribution of updraft velocity for parcels with different

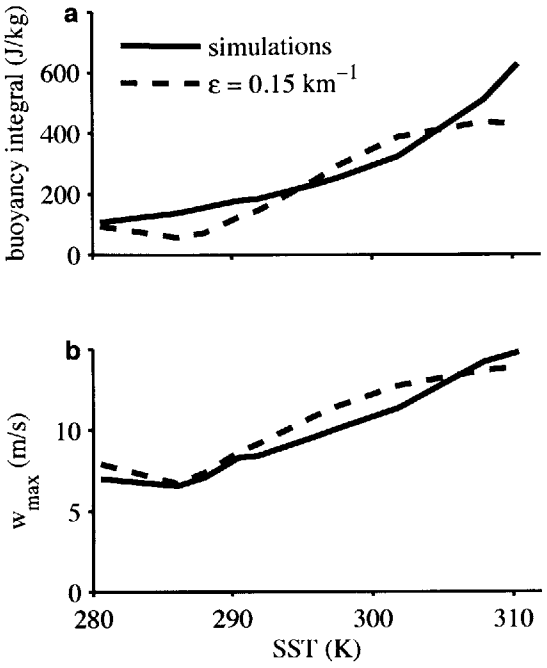

Figure 3-8: (a) Buoyancy integral and (b) peak value of the 99.99th percentile updraft profile, w_{max}, calculated in the high-resolution simulations (solid) and estimated by a plume calculation with a fixed entrainment rate of 0.15 km^{-1} (dashed). The plume estimate of the buoyancy integral is calculated as the vertical integral of the positive plume buoyancy up to the level at which the mean temperature in the simulations is equal to 220 K. The plume estimate of w_{max} is taken as the maximum value of vertical velocity achieved by the plume below the level at which the mean temperature of the simulations is equal to 220 K.

values of moist static energy. As with the buoyancy, the plume spectrum captures the increase of updraft velocity with increasing temperature for high percentiles of the moist static energy distribution in the simulations.

Having shown the fidelity of the plume spectrum in reproducing the buoyancy and updraft velocity for air parcels in the simulations with high values of moist static energy, we consider again the distribution of effective entrainment rates. As noted earlier, the 99.999th percentile of moist static energy has a similar effective entrainment rate through a large portion of the troposphere in all the simulations shown. Additionally, the 99.9th percentile of moist static energy has an effective entrainment rate of roughly 0.5 km^{-1} in the lower troposphere of all the simulations

shown. The consistency of the effective entrainment rate for these high percentiles of the moist static energy distribution suggests some insight may be gained from the plume spectrum by assuming the entrainment distribution among plumes remains fixed as the atmosphere warms. That is, assuming that the fraction of air parcels represented by a plume of a given entrainment rate remains fixed as the surface temperature varies.

We explore this possibility by comparing the buoyancy integral and peak updraft in the simulations to those estimated by a set of plumes with a fixed entrainment rate (Fig. 3-8). As in the previous section, our measure of the buoyancy integral in the simulations is based on the profile of the 99.99th percentile of buoyancy, and the peak updraft is taken as the maximum of the 99.99th percentile vertical velocity profile, w_{max}. The plumes are calculated as in section 3.4.1, and an entrainment rate of 0.15 km^{-1} is used. This entrainment rate is chosen to provide a good overall fit to the simulated buoyancy integral and w_{max}, but is somewhat below the value implied for the 99.99th percentile of moist static energy based on Fig. 3-7. This may be because the relationship between moist static energy and updraft properties is not one-to-one, and thus the percentiles of buoyancy and vertical velocity do not directly correspond to percentiles of the moist static energy (or effective entrainment) distribution.

The fixed-entrainment plume estimate roughly reproduces the magnitude of the increase in the buoyancy integral and w_{max} with warming. Since the entrainment rate and microphysical assumptions of the plume remain fixed as the surface temperature varies, the increase in the plume estimate of the buoyancy integral and peak updraft is a result of changes in the plume environment, as represented by the mean profiles in the simulations. (The surface perturbation of one standard deviation applied to the plumes contributes to the magnitude of the buoyancy integral as estimated by the plumes, but not to the increase with temperature.) Additional plume calculations in which the relative humidity of the environment is fixed to a constant value, rather than taken from the simulations (not shown), suggest that the increase in the plume estimate of the peak updraft is mostly due to changes to the lapse-rate in the simulations with warming. These results highlight the importance of the CAPE increase

found in the simulations in determining the behavior of the updraft velocity with warming.

The fixed-entrainment plume estimate does not, however, capture the detailed dependence of the buoyancy integral on surface temperature in the simulations. For instance, in the simulations with the highest surface temperatures, the rate of increase of the simulated buoyancy integral with warming is at its largest value ($\sim 9\%$ K^{-1}), while the estimate from the fixed-entrainment plume gives almost no change in buoyancy integral with warming. The variation in w_{max} with temperature is relatively well captured by the fixed-entrainment plumes, but since the updraft velocity given by the plume calculation is dependent on the plume buoyancy below the level of the maximum updraft, this close level of agreement may be somewhat coincidental. These results suggest that some knowledge of the behavior of convective updrafts with warming can be derived from plume arguments applied to large-scale fields, but the precise rate of increase given by such estimates should be taken with caution (c.f. Del Genio et al. 2007).

Despite the above caveats, the ability of the plume estimate to reproduce the magnitude of the increase in the buoyancy integral with warming is noteworthy, given the much larger fractional increase in CAPE. Indeed, the plume estimate of the buoyancy integral is much larger if an undilute set of plumes is used in the calculation, rather than plumes with an entrainment rate of 0.15 km^{-1} (Fig. 3-9a). Furthermore, the undilute buoyancy integral increases by roughly a factor of fourteen over the range of surface temperatures simulated, while the buoyancy integral in the simulations and as estimated by the fixed-entrainment plume calculation increase by a factor of seven and five respectively. The plume spectrum thus suggests that the differing scaling of CAPE and cloud buoyancy integral in the simulations may be understood to be a result of a constant level of entrainment affecting the most intense updrafts at different temperatures.

In the next section we further investigate why the inclusion of entrainment results in a lower fractional increase in the plume estimate of the buoyancy integral. Our aim is to construct a simple model, along the lines of the zero-buoyancy plume model of

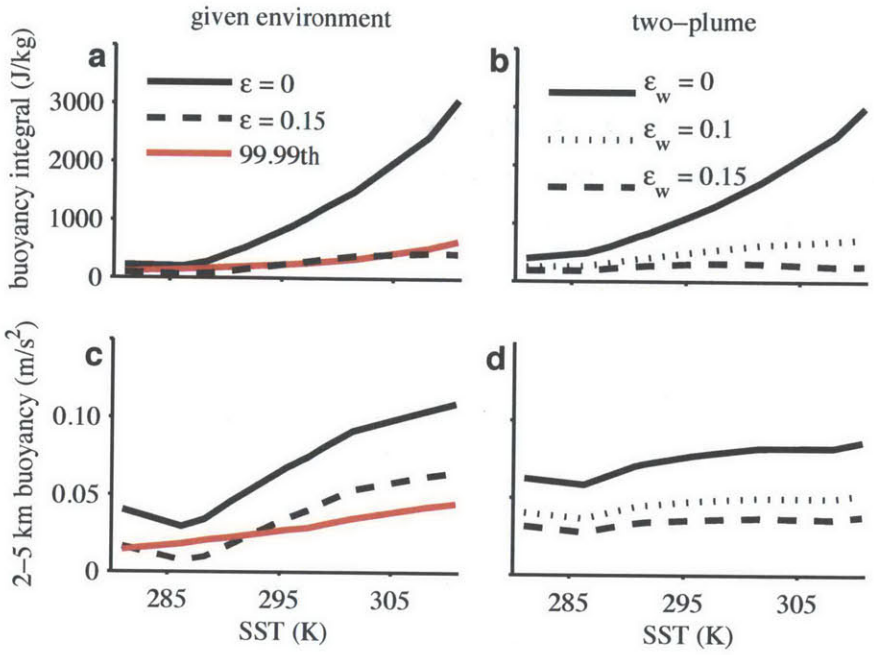

Figure 3-9: Estimates of (top) the buoyancy integral and (bottom) the mean buoyancy between 2 and 5 km for (left) the plume calculation with given environmental properties and (right) the two-plume model. Estimates are based on undilute plumes (solid) and plumes with entrainment rates of 0.1 km^{-1} (dotted) and 0.15 km^{-1} (dashed). The buoyancy integral is calculated as the integral of the plume buoyancy up to the level at which the environment temperature is 220 K. Results based on the 99.99th percentile buoyancy profile in the high-resolution simulations are shown in red. See text for details of plume calculations.

chapter 2, which includes a prediction for both the environmental lapse rate and the buoyancy of the most intense updrafts. Given the difficulty of accurately reproducing the simulated buoyancy integral, even when the environment is given, we do not expect detailed agreement between the simple model and the simulated buoyancy profiles. Instead, we seek to understand, on the conceptual level, how entrainment in the simulations may lead to a lower fractional rate of increase in the buoyancy integral with warming as compared to its undilute counterpart.

3.5 Two-plume model

3.5.1 Analytic formulation

We begin by considering an ensemble of convective clouds in RCE as modeled by two plumes; the first plume represents the clouds with relatively weak updrafts and strong entrainment and has an entrainment rate ϵ_s, while the second plume represents the most intense updrafts in the ensemble with a weak entrainment rate ϵ_w.

First we consider the strongly-entraining plume, with temperature T_s and moist static energy h_s. Following the arguments of chapter 2, we neglect the buoyancy of the strongly-entraining plume and assume it is exactly neutrally buoyant with respect to the environment. We may make some progress analytically if we ignore the effect of water on density and heat capacity, and we also neglect the contribution of ice-phase condensate to the plume moist static energy. Under these conditions the assumption of zero-buoyancy reduces to $T_s = T_e$, where the subscript e refers to the environment, as in section 3.4. Above the cloud base, the plume is saturated and we have that $h_s = h_s^* = h_e^*$, where the asterisk refers to a variable at saturation. Substituting this expression into the plume equation (3.1) allows us to write an equation entirely in terms of environmental properties and the entrainment rate ϵ_s,

$$\frac{dh_e^*}{dz} = -\epsilon_s(h_e^* - h_e). \tag{3.7}$$

This is similar to equation (2.2) of chapter 2.

We now consider the weakly-entraining plume, with moist static energy h_w, temperature T_w, and entrainment rate ϵ_w. Above the cloud base, this second plume is governed by

$$\frac{dh_w^*}{dz} = -\epsilon_w(h_w^* - h_e). \tag{3.8}$$

Subtracting (3.7) from (3.8) and solving the resultant ordinary differential equation gives,

$$h_w^* - h_e^* = \delta\epsilon \int_{z_b}^{z} e^{-\epsilon_w(z-z')}(h_e^* - h_e)dz', \tag{3.9}$$

where we have denoted $\delta\epsilon = \epsilon_s - \epsilon_w$, and we have assumed the plumes are identical below the level of the cloud base z_b. Additionally, we have assumed $\delta\epsilon$ is constant with height in order to simplify the presentation. We will relax this assumption in the next section.

Since $h_e^* - h_e = L_v(q_{ve}^* - q_{ve})$ the right-hand side of (3.9) depends on the saturation deficit of the free-troposphere. Linearizing the Clausius-Clapeyron equation about the environment temperature, we may write an expression for the temperature excess of the weakly entraining plume,

$$T_w - T_e = \frac{\delta\epsilon(1-\mathcal{R})}{1 + \frac{L_v^2 q_{ve}^*}{c_p R_v T_e^2}} \int_{z_b}^{z} e^{-\epsilon_w(z-z')} \frac{L_v q_{ve}^*}{c_p} dz, \tag{3.10}$$

where $\mathcal{R}$ is the relative humidity of the environment, assumed constant in the vertical, and R_v is the gas constant for water vapor.

Dividing by the environment temperature T_e, (3.10) gives an approximate equation for the buoyancy of the weakly-entraining plume, assuming the strongly-entraining plume has zero buoyancy. In the limit of $\epsilon_w \to 0$, this is similar to equation (2.4) of chapter 2 describing the buoyancy of undilute ascent. Here, we are interested in the case where the strongest updrafts, while having relatively low entrainment rates, are still far from undilute. The expression (3.10) states that the buoyancy of the weakly-entraining plume at some height z is proportional to the difference in entrainment rates between the plumes, $\delta\epsilon$, the relative humidity deficit of the environment, $1 - \mathcal{R}$, and a function of the saturation specific humidity that depends on its weighted integral below z. The dependence on the saturation specific humidity ensures that, for typical atmospheric temperatures, the buoyancy increases with temperature, assuming modest changes in the relative humidity of the environment and modest changes to the entrainment rates of the plumes. At very high temperatures, the denominator in (3.10) becomes large, and the dependence of the weakly-entraining buoyancy (at a fixed height) on temperature becomes weak. A similar equation to (3.10) was used in chapter 2 to account for the CAPE increase with warming in simulations of RCE. Here we will show that it may also be used to qualitatively account for the differ-

ences in the scaling of undilute buoyancy and cloud buoyancy with warming in our simulations.

It is instructive to consider the ratio of the buoyancy in the weakly-entraining plume to that of an undilute plume as given by (3.10). For simplicity, we approximate the dependence of the saturation specific humidity on height as an exponential, so that we may write,

$$q^*_{ve}(z) = q^*_{ve}(z_b) \exp\left(-\frac{z - z_b}{H_q}\right),$$

where H_q is the scale height for water vapor. In the undilute case ($\epsilon_w = 0$), the integral in (3.10) may then be written,

$$\int_{z_b}^{z} q^*_{ve} dz = H_q \left(q^*_{ve}(z_b) - q^*_{ve}(z)\right).$$

For the weakly-entraining plume ($\epsilon_w \neq 0$) one must also consider the exponential weighting function containing the entrainment rate ϵ_w. The result of the integral in (3.10) is dependent on the relative magnitudes of the water-vapor scale height H_q and the entrainment length ϵ_w^{-1}. The water-vapor scale height is of the order of 2-3 km, while the entrainment length scale is in the range 2-10 km for the entrainment rates characteristic of the high percentiles of the moist static energy distribution in Fig. 6. Here, we consider the case in which these two length scales are equal, for simplicity; the more general case behaves qualitatively similarly if H_q and ϵ_w^{-1} are of the same order, but the resultant analytic expressions are not as illuminating.

If $H_q = \epsilon_w^{-1}$, the integral in (3.10) then loses its exponential dependence, and we may write,

$$\int_{z_b}^{z} e^{-\epsilon_w(z-z')} q^*_{ve} dz = (z - z_b) q^*_{ve}(z).$$

Applying these results to (3.10), the ratio of the buoyancy of the weakly-entraining plume to the undilute buoyancy may then be written,

$$\frac{T_w - T_e}{T_u - T_e} = \frac{\delta\epsilon}{\epsilon_s} \frac{(z - z_b)}{H_q} \frac{q^*_{ve}(z)}{q^*_{ve}(z_b) - q^*_{ve}(z)}, \tag{3.11}$$

where T_u is the temperature of the undilute plume.

Consider how the ratio (3.11) at a fixed height in the mid-troposphere responds to warming. The assumption that H_q is constant in the vertical, used above to evaluate the vertical integral in (3.10), implies that the ratio $q^*_{ve}(z)/[q^*_{ve}(z_b) - q^*_{ve}(z)]$ remains constant with warming. If we also make the approximation that H_q does not vary as the surface temperature increases, the ratio in (3.11) is also constant with warming. In fact, H_q does vary somewhat, both in the vertical and with surface temperature. Nevertheless, as a first approximation, we might expect that the fractional increase in the buoyancy of the weakly-entraining plume at a fixed height is similar to that of the undilute buoyancy as the surface temperature increases. This is confirmed in more detailed calculations of the two-plume model outlined in the next section.

As pointed out in section 3.2, however, the top of the convecting layer remains at approximately fixed temperature as the atmosphere warms. Consider next the value of (3.11) in the region just below the top of the convecting layer. As the surface temperature increases, the numerator in (3.11) will be evaluated at roughly fixed temperature, and the only term that varies significantly is $(z - z_b)$, the depth of the convecting layer. For a roughly constant lapse-rate, the depth of the convecting layer increases linearly with increasing surface temperature. The denominator of (3.11), on the other hand, will increase exponentially with warming as a result of the dependence on $q^*_{ve}(z_b)$. This implies that, in the region just below the top of the convecting layer, the ratio given by (3.11) decreases with warming, and the fractional increase in the buoyancy of the weakly-entraining plume is smaller than that of the undilute buoyancy.

The approximate results presented in this section suggest a number of conclusions about the scaling of buoyancy with temperature according to the two-plume model, assuming weak changes in the tropospheric relative humidity and the entrainment rates of the plumes:

i. The buoyancy of the weakly-entraining plume increases with warming.

ii. The scaling of the weakly-entraining buoyancy and undilute buoyancy with temperature are similar at fixed height in the mid-troposphere. But near the top of

the convecting layer the fractional increase in undilute buoyancy with warming is larger than that of the weakly-entraining buoyancy.

iii. Point (ii) implies that, for the integral of the buoyancy over the convective layer, the fractional increase is somewhat higher in the undilute case than the weakly-entraining case.

These conclusions have been derived for the specific case in which the water-vapor scale height and the entrainment length are equal, and the difference in plume entrainment rates $\delta\epsilon$ is constant in the vertical. We next show that the conclusions broadly hold for a more detailed calculation of the two-plume model in which these assumptions are not made.

3.5.2 Numerical solution

We compare results from numerical integrations of the two-plume model to results from the plume spectrum calculated in section 3.4 and results from the simulations. The effects of water on the density and specific heat capacity of moist air, as well as the contribution of ice to the moist static energy are included in the plume calculations described here, unlike in the approximate treatment given in equations (3.7-3.11).

The properties of the strongly-entraining plume and the environment are calculated using an identical method to that of the zero-buoyancy plume model of chapter 2. We set the lower boundary condition of the strongly-entraining plume to be equal to the mean properties at the lowest model level in the corresponding simulation, and we integrate the plume equations upward assuming the strongly-entraining plume is exactly neutrally buoyant with respect to the environment, and assuming no fallout of condensate. We use an entrainment profile given by $\epsilon_s = 0.5/z$, and a constant environmental relative humidity of 80%. The same parameters were used in chapter 2 to reproduce the CAPE in simulations of RCE at different surface temperatures. We use an entrainment profile that varies inversely with height in order to crudely account for the bulk effects of many clouds detraining at different levels, since the strongly-entraining plume is representing nearly all of the mass flux in the domain.

The weakly-entraining plume, representing only the most intense updrafts, is given a constant entrainment rate. It is calculated using the environmental properties derived above, and it is initialized at the lower boundary as in the plume spectrum; the temperature and specific humidity of the weakly-entraining plume are set to the temperature and specific humidity at the lowest model level in the simulations corresponding to one standard deviation above the mean [see equation (3.4)]. (Initializing the weakly-entraining plume with the mean properties at the lowest model level does not change the qualitative behavior of the two-plume model.)

The two-plume model estimate of the buoyancy integral increases with warming, at least for low values of ϵ_w, and its fractional rate of increase is largest in the case where the weakly-entraining plume is undilute (Fig. 3-9b). On the other hand, the scaling of the mean buoyancy in the lower-troposphere with temperature according to the two-plume model is similar for both the undilute and entraining cases (Fig. 3-9d). These characteristics are consistent with the behavior of both the plume spectrum with a given environment, and the simulations, both in terms of the buoyancy integral as described earlier (Fig. 3-9a), and in terms of the lower-tropospheric buoyancy; the fractional increase in the mean buoyancy between 2 and 5 km is similar for the undilute plumes, the fixed-entrainment plumes and the 99.99th percentile of buoyancy in the simulations (Fig. 3-9c). This suggests that the two-plume model captures some of the behavior of the simulations, and it may be relevant for understanding the scaling of CAPE and cloud buoyancy in the RCE simulations.

However, there are also substantial differences between the behavior of the two-plume model and the simulations. For example, the lower-tropospheric (2 – 5 km) buoyancy according the two-plume model increases by a factor of 1.3 – 1.5, depending on the entrainment rate, across the simulations. The simulated lower-tropospheric buoyancy, on the other hand, increases by a factor of 3. Furthermore, for a value of $\epsilon_w = 0.15$ km^{-1}, equal to the entrainment rate used to match the simulations in the given-environment calculation, the two-plume buoyancy integral decreases with warming at high surface temperatures. It is only if a lower entrainment rate (0.1 km^{-1}) is used that the two-plume model reproduces the behavior of the simulations

(Fig. 3-9). The two-plume model is thus a useful tool for understanding the effect of entrainment on a convective ensemble, but is too crude to provide quantitatively accurate predictions of the buoyancy of clouds at different surface temperatures.

One reason for the poor quantitative agreement between the two-plume model and the simulations is that the environmental lapse rate is entirely determined by a single plume which must account for the bulk effects of all the convection in the domain. For the simple inverse height entrainment profile used, this results in an atmosphere that is too stable in the middle and upper troposphere. For instance, the level of neutral buoyancy for a plume with $\epsilon_w = 0.15$ km^{-1} in the warmest simulation according to the two plume model is roughly 10 km. From Fig. 3-7 it is seen that, a similar plume with the environment given from the simulations is neutrally buoyant at a height closer to 12 km. This difference explains part of the decrease in the buoyancy integral with warming according to the two-plume model at high surface temperature.

A possible alternative to the two-plume model that may address some of these deficiencies is to consider a spectrum of plumes as in section 3.4 and calculate the effect of all plumes on the mean lapse rate. Similar plume-spectrum models are the basis of many convective parameterizations in which the spectrum is used to determine the mass flux in convective clouds based on large-scale parameters (e.g., Arakawa and Schubert, 1974). In the case of RCE, the total mass flux in the domain is determined by the tropospheric radiative cooling (Robe and Emanuel, 1996; Takahashi, 2009), and the plume spectrum could instead be used to compute the environmental temperature profile that is consistent with this radiative cooling profile.

To close the problem, knowledge of the entrainment distribution among clouds is required. It may be possible to construct simple theoretical cloud-entrainment distributions based on an assumed relationship between cloud entrainment and cloud size (e.g., Tiedtke, 1989), and theoretical studies of the cloud size distribution (as measured by cloud-base mass flux) (Craig and Cohen, 2006; Cohen and Craig, 2006). Alternatively, the entrainment distribution could be derived from the CRM simulations themselves. The important aspect of such a plume-spectrum model is the

assumption that the entrainment distribution remains fixed as the surface temperature increases, allowing for a prediction of the updraft properties with warming. Such a detailed model of the interaction between convective clouds and their environment is beyond the scope of the present study, and we leave it to future work.

3.6 Conclusions

We have used simulations of radiative-convective equilibrium in a cloud-system resolving model to investigate the dependence of convective updraft velocity on surface temperature. The updraft velocity increases with warming in the simulations, with the largest fractional increases occurring for the most intense updrafts. Consistent increases in the buoyancy of clouds are also found; a roughly linear relationship exists between the vertical integral of the buoyancy and the square of the peak updraft velocity. As was documented in chapter 2, the CAPE in simulations of RCE also increases with warming, but the fractional increase in CAPE is considerably larger than the increase in the buoyancy integral.

We investigated the increases in buoyancy and updraft velocity using a conceptual model based on a set of entraining plumes. Firstly, we considered a plume model in which the environment is taken as the mean profile in the simulations, and the entrainment and microphysical assumptions of the plume remain fixed as the atmosphere warms. The plume model reproduces the magnitude of the simulated increase in updraft velocity with warming, suggesting changes to the mean lapse rate in RCE, as measured, for example, by the increase in CAPE, are important factors in determining the behavior of the simulated updraft velocity at different surface temperatures.

The plume results also suggest that the higher fractional increase of CAPE relative to the buoyancy integral with warming may be a result of the effect of entrainment on even the most intense updrafts in the simulations. A conceptual model for the relative scaling of undilute buoyancy and entraining buoyancy was constructed through a generalization of the zero-buoyancy plume model introduced in chapter 2 to the case of two plumes. This two-plume model provides a prediction of the changes in

the undilute and entraining buoyancy given the value of the tropospheric relative humidity. It predicts substantial increases in the vertical integral of plume buoyancy with warming, with the largest fractional increases occurring for plumes with no entrainment. This is consistent with the behavior of the simulations, suggesting the possible utility of considering the convective ensemble as consisting of a spectrum of plumes with an invariant entrainment distribution.

Previous work has suggested that the fall speed of hydrometeors may play a large role in determining the updraft velocity in moist convection (Parodi and Emanuel, 2009). The mean hydrometeor fall speed increases with warming in our simulations owing to an increase in the relative proportion of rain versus snow in the column. However, as will be documented further in chapter 4, the peak updraft velocity in our simulations, as measured by the maximum in the 99.99th percentile vertical velocity profile, is relatively insensitive to variations in hydrometeor fall speed unless a simpler warm-rain microphysics scheme is employed. Nevertheless, a role for microphysics, including the formation of precipitation, in determining the updraft velocity distribution in our simulations cannot be ruled out, even for the case where ice processes are important.

An additional factor not accounted for in the plume calculations is the role of the changing radiative cooling profiles as the atmosphere warms. Previous work has suggested that changes to the radiative cooling profile in RCE have a weak effect on the updraft velocity, and primarily affect the area fraction over which convection occurs (Robe and Emanuel, 1996). However, these area-fraction changes could potentially affect the updraft velocity at given percentiles, since the total fraction of the atmosphere experiencing upward motion is changing. For instance, Muller et al. (2011) found markedly different responses of CAPE and updraft velocity to warming in simulations of RCE in which the radiative cooling profile was fixed compared to cases where an interactive radiation scheme was used. The reasons for these different responses are not well known, but may relate to the effect of the radiative-cooling profile on the cloud fraction, or the effect of differences in the behavior of cloud microphysics in simulations with different radiative-cooling profiles.

The increase in updraft velocity found in the simulations, while large, occurs primarily in the upper troposphere. Other authors have shown the importance of the precise vertical profile of the updraft for the intensity of the heaviest precipitation events (precipitation extremes) (Muller et al., 2011; O'Gorman and Schneider, 2009b). In particular, the updraft velocity in the lower-troposphere is critical in determining the condensation rate during precipitation extremes. The weak changes in lower-tropospheric updraft velocity with warming in our simulations result in dynamical changes to precipitation extremes that are relatively small. Instead, thermodynamic and microphysical processes are dominant in driving changes to precipitation extremes with warming. We will investigate the scaling of precipitation extremes in RCE further in the next chapter.

The large changes in upper-tropospheric updraft velocity found in our simulations are associated with increases in convective overshooting, as measured by an increase in the magnitude of negative buoyancy fluxes in the upper troposphere. If such increases in overshooting were to occur in Earth's atmosphere as a result of global warming, there may be potential implications for the thermodynamic structure and transport properties of the region near the tropopause (e.g., Kuang and Bretherton, 2004; Chaboureau et al., 2007; Jensen et al., 2007). However, the plume results shown here suggest that the updraft velocity increases are sensitive to the representation of cloud entrainment in the simulations. While a large body of work exists studying cumulus entrainment [see section 6.2.1 for a brief review], the mechanisms by which clouds mix with their environment are not fully understood, nor are they well resolved in our simulations. It is thus unclear to what extent the results for RCE simulations may be applied to convection on Earth, and further work is needed to determine if the changes to the updraft velocity in RCE simulations described in this chapter have implications for the tropical tropopause layer in a warmer climate.

Chapter 4

The role of hydrometeor fall speed in the scaling of precipitation extremes with temperature

4.1 Introduction

Increases in the intensity of precipitation extremes are seen in simulations of climate warming (Kharin et al., 2007; O'Gorman and Schneider, 2009a) and have been identified in observational trends (Westra et al., 2013). Analyses of variability in the current climate also show a relation between precipitation extremes and the temperature at which they occur (e.g., Allan and Soden, 2008; Lenderink and van Meijgaard, 2008). However, the rate at which precipitation extremes strengthen as the climate warms remains uncertain to the extent that they involve moist-convective processes that are difficult to represent in climate models (Wilcox and Donner, 2007; O'Gorman, 2012).

Here we investigate the precipitation distribution in simulations with a cloud-system resolving model (CRM) in the idealized setting of radiative-convective equilibrium (RCE). Previous studies of the precipitation distribution in RCE have found that, at surface temperatures characteristic of Earth's tropics, precipitation extremes increase with warming following what is known as Clausius-Clapeyron (CC) scaling,

increasing roughly in proportion to the saturation specific humidity near the surface (Muller et al., 2011; Romps, 2011). This conclusion holds even when the convection is organized (Muller, 2013). CC scaling of precipitation extremes with surface temperature is consistent with a simple view of the response of strong precipitation events to warming in which the amount of converged water vapor increases due to the increased amount of moisture near the surface. However, the close agreement with CC scaling found in modeling studies of RCE may be coincidental because the water-vapor convergence does not occur only at the surface and the strength and vertical profile of the updraft changes with warming (Muller et al., 2011; Romps, 2011). In this study, we extend previous results to a wider range of surface temperatures and find that, in general, precipitation extremes in RCE do not follow a simple scaling based on the amount of near-surface moisture. In particular, for accumulation periods shorter than one hour and surface temperatures lower than 295 K, precipitation extremes increase with warming at a considerably higher rate than implied by CC scaling.

We argue that the high rate of increase of precipitation extremes found in our simulations is a result of a change in the mean fall speed of hydrometeors in a warming atmosphere. In simulations in which the fall speeds of hydrometeors are fixed to a constant value, the increase of precipitation extremes with warming is generally at a lower rate than predicted by CC scaling, and the precipitation extremes depend strongly on the imposed fall speed. When interactive fall speeds are included, the mean fall speed of precipitation increases with temperature as the makeup of hydrometeors in the column switches from being dominated by slowly falling snow to more rapidly falling rain. The rate of increase of precipitation extremes may then be seen to be largely a result of the increase in surface moisture in combination with the increase in hydrometeor fall speed as the atmosphere warms. A role for hydrometeor fall speeds in determining both the precipitation intensity and the updraft strength in RCE has been suggested previously (Parodi and Emanuel, 2009; Parodi et al., 2011). Here we find that the hydrometeor fall speed affects the precipitation rate through changes in precipitation efficiency, but that the effect on updrafts is relatively weak.

While the results we will show are for the idealized case of RCE, the mechanisms

involved are sufficiently general to be of potential relevance to Earth's atmosphere. Observational relationships between temperature and precipitation extremes on sub-daily timescales can vary substantially by region (Hardwick Jones et al., 2010), but analyses of station observations have suggested a scaling of precipitation extremes with temperature of up to twice the CC rate at particular locations (Lenderink and van Meijgaard, 2008; Lenderink et al., 2011; Berg et al., 2013). The increase in the fall speed of hydrometeors accompanying warming is one possible mechanism contributing to such high rates of increase of precipitation extremes.

4.2 Precipitation extremes in radiative-convective equiilbrium

We investigate precipitation extremes in a series of simulations of RCE conducted using version 16 of the Bryan Cloud Model (Bryan and Fritsch, 2002) with slight alterations to improve energy and mass conservation described in the appendix. These simulations are identical to those described in chapter 2 and 3 where the focus was on understanding increases in convective available potential energy and updraft velocity in RCE with warming. Of particular importance for the present chapter is the treatment of microphysics in the simulations; a six-species, one-moment scheme based on Lin et al. (1983) is used in which there are three hydrometeor species (rain, snow and hail) each with a different fall speed that depends on mixing ratio. Further details of the model configuration may be found in section 2.2

We present results based on a series of simulations in which each simulation has a different imposed CO_2 concentration in the range 1 – 640 ppmv. The series is run at three different horizontal resolutions, with all simulations including 64 vertical levels. First, a set of low-resolution simulations (2 km horizontal grid-spacing, 80 × 80 km domain) are run to equilibrium over a slab ocean of depth 1 m. These slab-ocean simulations achieve equilibrium SSTs in the range 281 – 311 K. A set of intermediate-resolution simulations (1 km horizontal grid spacing, 84 × 84 km domain) and a

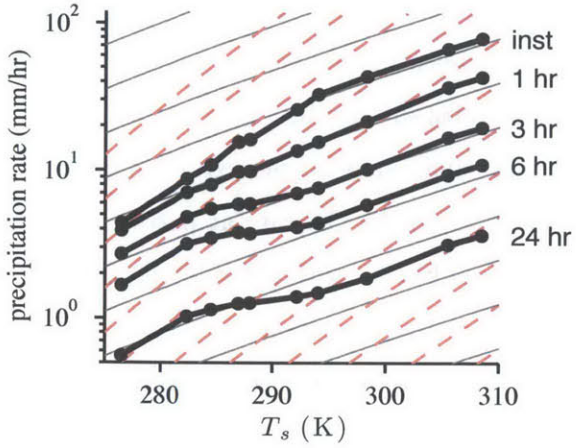

Figure 4-1: 99.99th percentile of precipitation rate in high-resolution simulations (black lines) calculated using various accumulation periods and shown as a function of the mean temperature at the lowest model level (T_s). Accumulation periods of one model time-step (inst), one hour (1 hr), three hours (3 hr), six hours (6 hr) and one day (24 hr) are shown. Gray lines are contours proportional to the surface saturation specific humidity, and red-dashed lines are contours proportional to the square of the surface saturation specific humidity; each successive line corresponds to a factor of two increase.

set of high-resolution simulations (0.5 km horizontal grid spacing, 160 × 160 km domain) are then conducted with the same range of CO_2 concentrations and using the equilibrium SSTs of the corresponding slab-ocean simulations as a fixed lower boundary condition. The intermediate-resolution simulations are each run for 40 days, and the high-resolution simulations are run for 30 days. In both cases we begin collecting statistics at hourly intervals after 20 days of simulation. Results are broadly similar across resolutions; we show results from the high resolution simulations in this section, but in following sections we switch to the intermediate-resolution results to allow direct comparison with additional intermediate-resolution simulations in which the fall speeds of hydrometeors are set to fixed values.

Fig. 4-1 shows precipitation extremes as measured by the 99.99th percentile of gridbox precipitation rates (zero precipitation rates are included when calculating percentiles) in the high-resolution simulations as a function of the mean temperature in the lowest model level (T_s) and for different accumulation time periods. The precipitation extremes increase as the accumulation period decreases, with the highest

values occurring for instantaneous (i.e., accumulated over one model time step) precipitation extremes. The fractional rate of increase of precipitation extremes with warming also varies with the accumulation period used. At surface temperatures below $\sim$ 295 K instantaneous precipitation extremes increase rapidly with temperature, exceeding the rate of increase given by CC scaling (gray lines) of 6-7% K^{-1} and approaching twice that rate (red-dashed lines). As the surface temperature increases above 295 K the rate of increase drops to be very close to that implied by CC scaling.

At longer accumulation periods of 3 hours and above, precipitation extremes increase at a rate that is generally close to that implied by CC scaling, although there is some variability in the rate of increase with temperature. At an intermediate accumulation period of one hour the rate of increase of precipitation extremes is somewhat higher than CC scaling at most temperatures. Consistent with previous studies (Muller et al., 2011; Romps, 2011), the rate of increase of precipitation extremes at surface temperatures typical of Earth's tropics is close to that implied by CC scaling at all accumulation periods.

The scaling of precipitation extremes documented here is somewhat sensitive to the percentile chosen. Higher percentiles (99.999th) show results consistent with Fig. 4-1, but lower percentiles (99.9th) show considerable variation in the rate of increase of precipitation extremes with warming. Nevertheless, instantaneous precipitation extremes generally increase at a rate substantially higher than implied by CC scaling over part of the range of temperatures simulated. This super-CC increase is worthy of further investigation since similar rates of increase have been reported in sub-daily station observations at both sub-tropical and temperate latitudes when precipitation is binned by daily mean surface temperature (Lenderink and van Meijgaard, 2008; Lenderink et al., 2011).

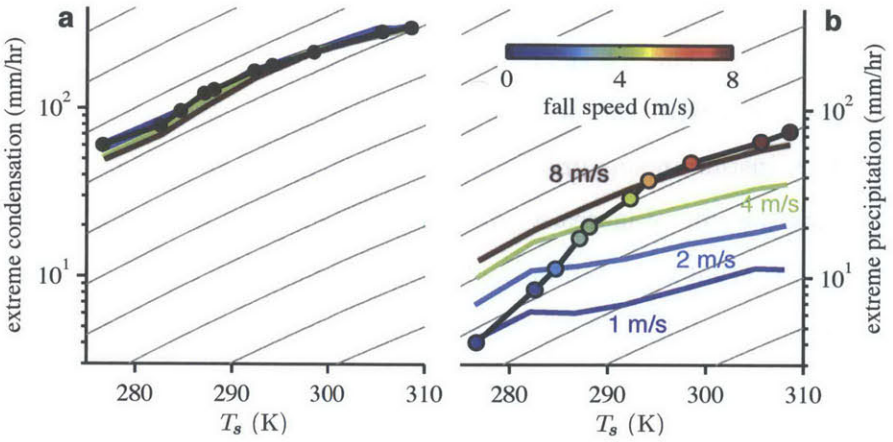

Figure 4-2: The 99.99th percentile of instantaneous (a) column net-condensation rate and (b) surface precipitation rate as a function of the mean temperature of the lowest model level (T_s) in intermediate-resolution simulations. Black lines correspond to full-microphysics simulations while colored lines show results from simulations in which the fall speed of all hydrometeors is set to constant values of 1 (blue), 2 (cyan), 4 (green) and 8 (maroon) m s^{-1}. Marker colors in (b) correspond to the effective fall speed of hydrometeors in the full-microphysics simulations (see text). Thin gray lines are contours proportional to the surface saturation specific humidity, with each successive line corresponding to a factor of two increase.

4.3 Scaling of condensation extremes with surface temperature

To examine the processes leading to deviations in the rate of increase of precipitation extremes from CC scaling we first consider extremes of the column net-condensation rate (Fig. 4-2a). The column net-condensation rate refers to the instantaneous condensation rate minus the instantaneous evaporation rate integrated over a column. Net-condensation extremes increase at a rate close to or slightly less than the CC rate over all temperatures, in contrast to the super-CC increase in instantaneous precipitation extremes, and despite the peak vertical velocity conditioned on net-condensation extremes increasing from 7 to 12 m s^{-1} over the range of temperatures simulated (Fig. 4-3). In order to explain the sub-CC scaling of net-condensation extremes in light of the increase in peak updraft strength we consider a decomposition of the net

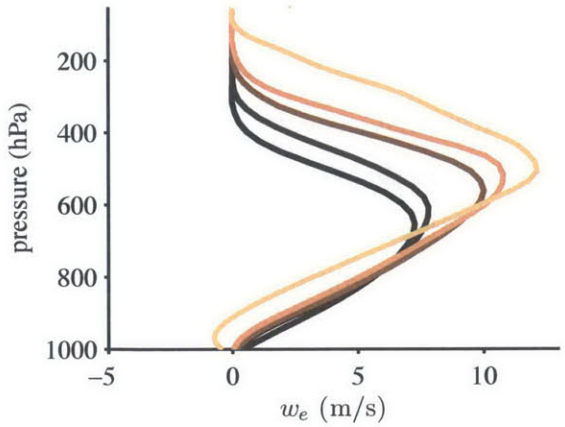

Figure 4-3: Mean vertical velocity profiles for points in which the instantaneous net-condensation rate in the column exceeds its 99.99th percentile. Intermediate-resolution simulations with mean temperatures of the lowest model level (T_s) of 277 (black), 285, 292, 298 and 309 K (orange) are shown.

condensation similar to that given by Muller et al. (2011):

$$C_e = -\epsilon_C \int_0^{z_t} \frac{\partial \overline{q^*}}{\partial z} \overline{\rho} w_e \, dz. \tag{4.1}$$

Here C_e is the 99.99th percentile of column net condensation, ρ is the density, q^* is the saturation specific humidity, the over-bar represents a time and domain mean and z_t is the height of the tropopause. The vertical velocity profile w_e is calculated as the mean vertical velocity for points in which the column net-condensation rate exceeds its 99.99th percentile. The integral in (4.1) represents an estimate of the column net-condensation rate derived from the dry static energy budget (see Muller et al., 2011). The inaccuracies in the estimate associated with the approximations made in the derivation are collected into the condensation efficiency ϵ_C so that (4.1) is exactly satisfied.

Consider the simple case in which the mass flux $\overline{\rho} w_e$ during net-condensation extremes is constant in the vertical except for near the surface, where there is strong convergence, and near the tropopause, where there is strong divergence. The integral in (4.1) may then be approximately evaluated as proportional to the near-surface saturation specific humidity (O'Gorman and Schneider, 2009a; Muller et al., 2011).

If we further assume there are no changes in the mass flux or condensation efficiency with warming, condensation extremes must increase with warming at the CC rate.

Deviations of net-condensation extremes from CC scaling result from a more realistic mass-flux profile, or from changes in the mass-flux profile or efficiency ϵ_C with temperature. In particular, the expression for the condensation rate (4.1) includes the vertical velocity within an integral weighted by the vertical gradient in saturation specific humidity. This vertical gradient maximizes at the surface and decreases exponentially above, making the low-level vertical velocity critical in setting the net-condensation rate. In our simulations, w_e decreases with warming at levels below 800 hPa. Low-level changes in w_e, therefore, have a negative influence on net-condensation extremes, explaining how the peak updraft increases but the net-condensation rate increases at a rate lower than that implied by CC scaling. These results are consistent with those of Muller et al. (2011), who also found that changes in updraft profile with warming weakened the scaling of precipitation extremes, despite increases in the peak value of the updraft as the surface temperature increased. We also find that the condensation efficiency ϵ_C decreases between 0.84 and 0.74 across the intermediate-resolution simulations (not shown), contributing to the sub-CC scaling of instantaneous net condensation in the simulations.

4.4 The effect of the fall speed of hydrometeors on precipitation extremes

It is useful to represent the relationship between instantaneous net-condensation extremes and instantaneous precipitation extremes by an efficiency ϵ_P such that,

$$P_e = \epsilon_P C_e, \tag{4.2}$$

where P_e is the 99.99th percentile of the precipitation rate. Since we consider net condensation, and since the occurrence of precipitation extremes may not be exactly collocated in space and time with the occurrence of net-condensation extremes, ϵ_P is

not a precipitation efficiency in the traditional sense. Nevertheless, ϵ_P represents the efficiency by which large net-condensation events are translated into large precipitation events as the condensate falls to the surface.

At low temperatures, the fractional rate of increase of instantaneous precipitation extremes with warming is larger than that of instantaneous net-condensation extremes, indicating that ϵ_P increases with warming. The value of ϵ_P is determined by the degree to which the precipitation is spread out relative to the column net condensation both spatially and temporally, as well as the fraction of condensation that evaporates in the time between the net-condensation event and its related precipitation event. These mechanisms are particularly sensitive to the microphysical properties of clouds. For instance, in the limit of instantaneous removal of condensate from the atmosphere, the precipitation rate equals the condensation rate, and ϵ_P is unity at all temperatures. In the opposite limit, in which condensed water takes a long time to form precipitation or the hydrometeor fall speed is low, turbulence and the cloud-scale circulation have a long time to act in removing the condensate from the column, and the precipitating hydrometeors may spend long periods of time in sub-saturated air (Fig. 4-4a). A low hydrometeor fall speed may also affect ϵ_P by spreading out the precipitation in time. Since the condensation occurs at a range of heights, precipitation will reach the ground at different times, even if the condensation were to occur at a single instant. If the timescale over which precipitation falls out is larger than the timescale of condensation events, this has the effect of spreading the precipitation event over a longer time period relative to the condensation event (Fig. 4-4b). For instantaneous precipitation extremes a lower hydrometeor fall speed would tend to reduce ϵ_P, but for precipitation accumulation times substantially longer than an individual convective event ($\sim$ 1 hour) the effect would be minimal.

The hydrometeor fall speed is sensitive to temperature changes; snow has typical fall speeds of 0.5 – 1 m s^{-1}, while rain often falls at speeds of 5 – 8 m s^{-1}. In the coldest simulations, precipitating hydrometeors spend most of their life as snow even though the surface precipitation is almost entirely in liquid form. We hypothesize that the super-CC scaling of precipitation extremes seen in the simulations is a result

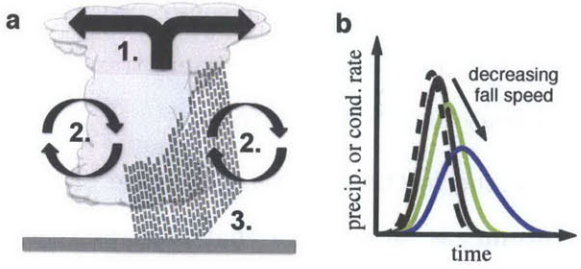

Figure 4-4: Schematic showing mechanisms affecting the value of ϵ_P. (a) Removal of liquid and solid water from the column by (1) the cloud-scale circulation and (2) turbulence (both resolved and sub-grid), as well as (3) evaporation and sublimation of precipitation. (b) Spreading of the precipitation event in time as the hydrometeor fall speed decreases (maroon to green to blue). Dashed black line represents the column net-condensation rate.

of a transition in hydrometeor distribution from a snow dominated regime to a rain dominated regime.

To investigate this hypothesis we examine additional intermediate-resolution simulations in which the model microphysics are altered such that the fall speed of all hydrometeors are fixed to a constant value. Sets of simulations are conducted with fall speeds in the range $1 - 8$ m s^{-1}; for each fall speed, seven simulations are run with different SST boundary conditions corresponding to a subset of the SSTs used in the full-microphysics simulations described in section 4.2. Apart from the values of the fall speeds of snow, rain and hail, the model used for each of these simulations is identical to the model used for the corresponding full-microphysics simulation at the same SST.

Previous work has shown that the hydrometeor fall speed strongly affects precipitation rates in RCE (Parodi et al., 2011). Parodi and Emanuel (2009) also showed that the fall speed influenced updraft velocities in moist convection. But in the simulations shown here net-condensation extremes (Fig. 4-2a) as well as the peak value of the updraft velocity (not shown) are relatively insensitive to the hydrometeor fall speed. Some dependence of the updraft strength on hydrometeor fall speed is found if only warm-rain microphysical processes are allowed as in Parodi and Emanuel (2009), but in general the effect of hydrometer fall speed on ϵ_P is a much larger factor in de-

termining the intensity of precipitation extremes. An increase in fall speed from 1 to 8 m s^{-1} results in an increase in instantaneous precipitation extremes by more than a factor of five at a surface temperature of $T_s = 298$ K (Fig. 4-2b). (For the case of 3 hourly accumulation this factor is reduced to approximately 2.5.) On the other hand, increasing the surface temperature while keeping the hydrometeor fall speed fixed results in an increase in precipitation extremes somewhat less than predicted by CC scaling.

An effective hydrometeor fall speed is defined by taking the hydrometeor-mass weighted mean of the fall speeds of all hydrometeors in the column conditioned on the precipitation rate exceeding its 99.99th percentile. In the fixed fall-speed simulations this is simply equal to the imposed hydrometeor fall speed. In the simulations with full microphysics, the effective fall speed ranges from less than 1 m s^{-1} in the coldest simulation to above 7 m s^{-1} in the warmest simulation (Fig. 4-2b). This is primarily a result of the increasing fraction of rain compared to snow in the column as the atmosphere warms, but the increase in rain mixing ratios with warming also increases the mean fall speed of rain itself. Hail has a fall speed larger than both snow and rain, but it contributes only a small fraction of the total hydrometeor loading of the atmosphere.

The precipitation extremes in a given full-microphysics simulation are roughly consistent with those in a fixed fall-speed simulation at the same surface temperature and with the same effective fall speed (compare the marker colors and line colors in Fig. 4-2b). This implies that without the change in fall speed, the increase of precipitation extremes with warming in the full-microphysics simulations would be somewhat below the CC rate. We thus conclude that the super-CC increase in instantaneous precipitation extremes found in the full-microphysics simulations is a result of the increase in the mean fall speed of hydrometeors that accompanies a switch from a snow-dominated to a rain-dominated hydrometeor distribution. Even for longer accumulation periods, the increase in precipitation extremes with warming for simulations with fixed hydrometeor fall speeds is less than the CC rate (not shown). The rough CC-scaling of precipitation extremes at accumulation periods longer than one hour in

the full-microphysics simulations appears to result from increases in hydrometeor fall speed that increase the precipitation efficiency relative to the fixed fall speed case.

4.5 Conclusions

We have investigated the relationship between precipitation extremes and surface temperature in CRM simulations of RCE. At temperatures characteristic of Earth's tropics or higher, the increase in precipitation extremes with warming is consistent with Clausius-Clapeyron scaling, whereby precipitation extremes scale with the near-surface saturation specific humidity. At lower surface temperatures the rate of increase of precipitation extremes with warming depends on the accumulation period under consideration. For accumulation periods of one hour or less stronger increases in precipitation extremes than expected from CC scaling are found over a broad range of temperatures, and at the shortest timescale the increase in precipitation extremes with warming approaches twice the CC rate. For longer accumulation periods, the rate of increase in precipitation extremes depends somewhat on temperature, but remains relatively close to the CC rate.

The reasons for the super-CC scaling of precipitation extremes are found to relate to changes in the fall speed of hydrometeors as the surface temperature is increased. At low temperatures, the precipitating water in the column is primarily composed of snow, while at higher temperatures it is primarily composed of rain, which falls at much faster speeds. The fall speed of hydrometeors has a large impact on precipitation rates in the simulations, consistent with recent studies (Parodi and Emanuel, 2009; Parodi et al., 2011). But unlike Parodi and Emanuel (2009), the updraft velocity is relatively insensitive to changes in hydrometeor fall speed. The effect of hydrometeor fall speed on precipitation extremes in the simulations shown here is a result of changes in the efficiency with which large net-condensation events are translated into large precipitation events. The changing efficiency is likely to be a result of a changing fraction of condensate that is turbulently diffused out of the column or re-evaporated before reaching the ground, as well as, for short accumulation periods, a spreading out

of the precipitation event in time. In simulations in which the model microphysics are altered such that hydrometeors fall at a fixed speed, precipitation extremes increase with temperature more slowly than the CC rate. These results suggest that, absent changes in fall speed, the rate of change of precipitation extremes with warming would not necessarily be close to the CC rate, even for accumulation periods longer than one hour.

The increase of hydrometeor fall speed with temperature across the simulations is qualitatively consistent with a shift from snow to rain and is likely to be a robust result because of the large difference in the fall speeds of snow and rain. Snow falls relatively slowly (~ 0.6 m s^{-1}) in the particular implementation of the one-moment microphysical parameterization of Lin et al. (1983) used in the simulations for this study. Additional simulations in which the hydrometeor fall speeds are calculated identically to Lin et al. (1983) as updated by Potter (1991) have slightly faster falling snow but show similar results for the scaling of precipitation extremes.

The super-CC scaling of precipitation extremes with temperature seen in the simulations resembles the scaling of precipitation extremes found in some high temporal-resolution station observations when stratified by surface temperature (Berg et al., 2013). It has been argued that this observed super-CC scaling of precipitation extremes is the result of stronger updrafts occuring during warm events (Loriaux et al., 2013). In the simulations shown here, changes in updraft velocity only weakly affect the precipitation rate, and it is the fall speed of hydrometeors that is important for the scaling of precipitation extremes. One discrepancy is that the observed super-CC scaling of precipitation extremes with temperature occurs for accumulation periods of both one hour and 5 minutes (Berg et al., 2013), while in the simulations the instantaneous precipitation extremes exceed CC scaling to a greater extent than the hourly precipitation extremes. Additionally, other high-resolution precipitation observations do not show robust scaling of precipitation extremes at greater than the CC rate in response to local temperature variation (Hardwick Jones et al., 2010). Further study is required to evaluate under what conditions the mechanisms outlined here in simulations of RCE may be relevant for convective precipitation in the mid-latitudes and

sub-tropics of in the current climate or under climate change.

Chapter 5

Upward shift of the atmospheric general circulation under global warming: theory and simulations

5.1 Introduction

A robust feature of simulations of climate change in a variety of different models is a tendency for the atmospheric circulation to shift upwards as the climate warms. Studies with general circulation models (GCMs) forced with increasing greenhouse-gas concentrations have found an upward shift in the static stability profile (Kushner et al., 2001), transient kinetic energy and momentum flux (Lorenz and DeWeaver, 2007), relative humidity (Sherwood et al., 2010), large-scale condensation rate (O'Gorman and Schneider, 2008) and cloud fraction (Mitchell and Ingram, 1992). Studies with cloud system resolving models have also found upward shifts in response to warming, including upward shifts in the vertical velocities and distributions of cloud water and ice as the sea-surface temperature (SST) is increased (Tompkins and Craig, 1999;

[1]Material in this chapter is a slightly edited version of: Singh, Martin S., Paul A. OGorman, 2012: Upward shift of the atmospheric general circulation under global warming: theory and simulations. *J. Climate*, 25, 82598276.

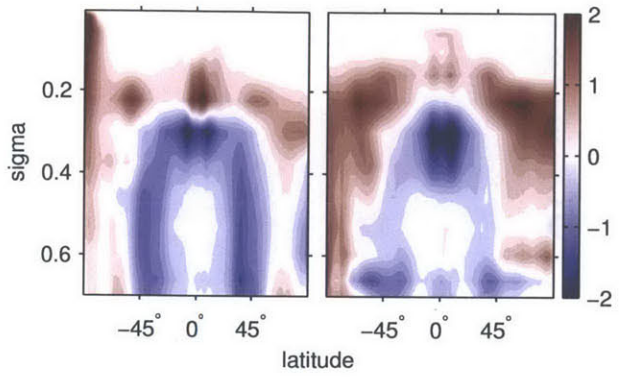

Figure 5-1: (left) Changes in zonal- and time-mean cloud fraction (%) between the last 20 years of the 20th and 21st centuries as simulated by the GFDL CM2.1 coupled model under the SRESA1b emissions scenario (Nakićenović et al., 2000). (right) Changes in the same statistic that result from an upward shift of the climatology of the last 20 years of the 20th-century (see text for details). The vertical coordinate is σ (pressure normalized by surface pressure). All changes shown are normalized by the change in global-mean surface air temperature (K).

Kuang and Hartmann, 2007; Muller et al., 2011).

One of the aims of this paper is to further document the upward shift in a wide range of variables and simulations. As a first example, Fig. 5-1 shows the changes in zonal-mean cloud fraction in a climate-change simulation with the Geophysical Fluid Dynamics Laboratory (GFDL) coupled climate model (CM2.1), and the corresponding changes obtained by an upward shift based on the climatology of cloud fraction from the same model. We define the upward shift as a transformation in pressure co-ordinates, so that $C'(p) = C(\beta p)$, where p is the pressure, C is the climatology of cloud fraction, and C' is the estimate of the cloud fraction in the warmer climate. The parameter $\beta = 1.12$ controls the magnitude of the shift; it is set based on the temperature changes simulated by the model (see section 5.5). The upward shift reproduces many of the features of the changes in cloud fraction simulated by the model, especially in the tropics and subtropics.

Mechanisms have previously been proposed to explain such upward shifts in clouds and certain other aspects of the general circulation as the climate is warmed. Artificially raising the tropopause in simulations with a dry idealized GCM results in a shift

of the zonal wind and eddy kinetic energy fields upward and poleward, similar to the changes that occur in comprehensive models forced with increases in greenhouse-gas concentrations. This suggests that increases in the height of the tropopause could be an important driver of shifts in the wind field (Lorenz and DeWeaver, 2007). An upward shift in tropical cloud properties as the surface is warmed has been attributed to the constraint on the temperature structure to remain close to neutral to moist convection (Tompkins and Craig, 1999). At a higher SST, the temperature remains pinned to a warmer moist adiabat, while the cloud features occur in the same temperature range. Since isotherms move upwards as the climate is warmed, this results in an upward shift to the profile. The "Fixed Anvil Temperature" (FAT) hypothesis of Hartmann and Larson (2002) suggests that convective anvil clouds, in particular, must remain at approximately the same temperature as the climate changes. This is because the vertical profile of heating in tropical convection is strongly constrained by the radiative cooling in clear sky regions. Since the dominant long-wave emitter in the troposphere is water vapor, its distribution essentially determines the distribution of radiative cooling. The dependence of saturation vapor pressure on temperature then ensures that the height to which cooling reaches, and thus the height of cloud tops and the circulation, must shift upwards as temperature increases.

We have, therefore, some understanding of why certain atmospheric properties might shift upwards with warming (at least in the tropics or near the tropopause). The need for an upward extension of the circulation with warming follows from the need to balance the upward extension of the radiative cooling rate as water vapor concentrations increase, and an upward shift may provide a consistent response of the circulation to the extent that latent heating rates and cloud properties also shift upwards. An upward shift cannot completely describe the response of the general circulation to warming because of the need to satisfy the surface boundary conditions, but it may provide a reasonable approximation to it sufficiently far from the lower boundary.

An advantage of viewing the atmospheric response to climate change in terms of shifts of the circulation is that one can then use observations of the general circulation

in the present climate to inform predictions of its behavior in a different climate. Motivated by this, and the ubiquity of the upward-shift response in model simulations, we seek to provide a more general theoretical basis for these vertical shifts that applies to all dynamic and thermodynamic variables. We construct a transformation based on the moist primitive equations that allows for the circulation to shift vertically while maintaining conservation of energy, water, and momentum. Thus, based on the governing equations and information about the current climate, we construct an estimate of the changes in the general circulation as the climate is warmed or cooled. The transformation may be viewed as giving the vertical structure of the response to climate change, but not the horizontal shifts in the circulation[2]. We do not consider cloud properties in the transformation to avoid dealing with the complexities of cloud microphysics, but we do consider related large-scale quantities such as statistics of relative humidity and vertical velocity; the changes in cloud fraction shown in Fig. 5-1 suggest that the theory could be extended to include changes in the cloud field.

We will show that the governing equations require that the vertical-shift transformation is not purely a vertical shift in the case of temperature or pressure (vertical) velocity. In addition to shifting upwards with warming, the pressure velocity also decreases in magnitude, implying a decrease in strength of the overturning circulation. While it is not immediately apparent that the decrease in circulation strength is related to the upward shift, the transformation implies that the two occur in tandem. A slowing down of the overturning circulation with warming has previously been related to the different rates of increase of specific humidity and precipitation in response to a given forcing (e.g., Held and Soden, 2006). While the accuracy of simple scaling arguments for the strength of the overturning circulation has been questioned (Schneider et al., 2010; Merlis and Schneider, 2011), many model simulations do show a decrease in the magnitude of the resolved-scale pressure velocity in the tropics in their response to greenhouse-gas induced warming (Knutson and Manabe, 1995; Held and Soden, 2006; Vecchi and Soden, 2007).

[2]The horizontal and vertical shifts of the circulation may be linked (e.g., Lorenz and DeWeaver, 2007), and a decomposition into horizontal and vertical shifts is necessarily an idealization.

We begin by deriving the vertical-shift transformation from the governing equations (section 5.2); a summary of the transformation is given by equations (5.13a-g). We then apply the transformation to simulations of warming in a number of models of varying complexity. Our aims are to determine the conditions under which it provides a good approximation to the response of the atmosphere to warming and to better interpret changes in more comprehensive models. We first demonstrate the ability of the transformation to reproduce pseudo-adiabatic parcel ascents initialized with different temperatures (section 5.3). We also consider an idealized aquaplanet GCM in which the radiative cooling is parameterized so as to conform to the transformation, and thus, in the free troposphere at least, the transformation represents a consistent solution to the governing equations (section 5.4). We then examine simulations performed for the World Climate Research Programme 3rd Coupled Model Intercomparison Project (CMIP3) and evaluate the extent to which the simple transformation reproduces the simulated response to greenhouse-gas and other forcings in comprehensive GCMs (section 5.5). Lastly, we summarize our results and discuss their implications (section 5.6).

5.2 Derivation of the transformation

5.2.1 Winds and geopotential

We work with the primitive equations in pressure coordinates and begin by considering the transformation of the winds and geopotential. The inviscid zonal momentum equation is given by

$$\frac{\partial u}{\partial t} + \frac{u}{a\cos\phi}\frac{\partial u}{\partial \lambda} + \frac{v}{a}\frac{\partial u}{\partial \phi} + \omega\frac{\partial u}{\partial p} = - \frac{1}{a\cos\phi}\frac{\partial \Phi}{\partial \lambda} + 2\Omega v\sin\phi + \frac{uv\tan\phi}{a},$$

where u and v are the zonal and meridional velocities, ω is the pressure velocity, a is the radius of the Earth, Ω is the rotation rate, and Φ is the geopotential. All fields

are functions of latitude, ϕ, longitude, λ, pressure, p, and time, t. Given a solution to the equations with zonal wind $u(\lambda, \phi, p, t)$ and meridional wind $v(\lambda, \phi, p, t)$, we define transformed winds (denoted by a prime) by setting

$$u'(\lambda, \phi, p, t) = u(\lambda, \phi, \beta p, t), \tag{5.1a}$$

$$v'(\lambda, \phi, p, t) = v(\lambda, \phi, \beta p, t). \tag{5.1b}$$

The transformation parameter β governs the magnitude of the rescaling in pressure; it will subsequently be taken to be close to unity. For values of $\beta > 1$, the circulation is shifted upwards by the transformation. By substitution, we find that the transformed solution satisfies the zonal momentum equation if we also define transformed pressure velocity and geopotential fields as

$$\omega'(\lambda, \phi, p, t) = \frac{\omega(\lambda, \phi, \beta p, t)}{\beta}, \tag{5.2a}$$

$$\Phi'(\lambda, \phi, p, t) = \Phi(\lambda, \phi, \beta p, t) + \Lambda(\beta p), \tag{5.2b}$$

for an arbitrary function of pressure $\Lambda(p)$. Similar considerations hold for the meridional momentum and continuity equations. Thus, for any solution of the horizontal momentum and continuity equations, we can find a corresponding vertically shifted solution defined by (5.1) and (5.2) that depends on the parameter β. The perturbation to the geopotential, $\Lambda(p)$, is a further degree of freedom by which the solution may be altered; its functional form will be constrained by the thermodynamic and hydrostatic equations.

5.2.2 Temperature

The hydrostatic equation may be written approximately as,

$$T = -\frac{p}{R}\frac{\partial \Phi}{\partial p}, \tag{5.3}$$

where T is the temperature and R is the gas constant for air[3]. Substitution of (5.2b) into (5.3) implies that the transformed temperature field must satisfy

$$T'(\lambda, \phi, p, t) = T(\lambda, \phi, \beta p, t) - \Delta T(\beta p), \tag{5.4}$$

where we have introduced

$$\Delta T(p) = \frac{p}{R}\frac{d\Lambda}{dp}. \tag{5.5}$$

To determine the form of ΔT, we enforce the requirement that the transformed solution satisfies the thermodynamic equation

$$c_p \Pi(p) \frac{D\theta}{Dt} = -L_v \frac{Dq}{Dt} + Q_{rad}, \tag{5.6}$$

where $\theta = T/\Pi$ is the potential temperature, $\Pi(p) = (p/p_0)^{\frac{R}{c_p}}$ is the Exner function, q is the specific humidity, L_v is the latent heat of vaporization, c_p is the specific heat capacity of air, and Q_{rad} is the radiative heating rate. To begin with, consider the simple case of unsaturated, adiabatic motion, in which the right hand side of (5.6) vanishes. The thermodynamic equation reduces to conservation of potential temperature, and any constant may be added to the potential temperature while still satisfying the equation. Hence, the transformed temperature (5.4) will satisfy the thermodynamic equation in this dry-adiabatic case if it has the form

$$T'(\lambda, \phi, p, t) = T(\lambda, \phi, \beta p, t) - \Delta\theta\, \Pi(\beta p), \tag{5.7}$$

where $\Delta\theta$ is a constant which may be varied independently of β. The freedom to independently rescale pressure by β in the dry primitive equations does not hold in the moist primitive equations because the vapor pressure then enters (Garner et al., 2007)[4]. As a result, the parameters $\Delta\theta$ and β are no longer independent in a moist

[3]Here, and for the rest of the derivation, we neglect the effects of water vapor on density and specific heat capacity, we take the latent heat of vaporization to be constant, and we neglect ice processes.

[4]The transformation presented here is not the same as the hypohydrostatic rescaling outlined in Garner et al. (2007). The vertical-shift transformation applies to the hydrostatic primitive equations, whereas the hypohydrostatic rescaling only alters the equations in the non-hydrostatic regime.

atmosphere, as we shall now see.

5.2.3 Moist processes

Returning to the thermodynamic equation (5.6), we consider the transformation of the latent heating term [the first term on the RHS of (5.6)]. We set $\Delta T = \Delta\theta\,\Pi$, with $\Delta\theta$ constant as in the dry case, so that dry adiabatic motions still transform correctly. For the latent heating term to transform correctly, we must also require that the specific humidity shifts vertically according to

$$q'(\lambda, \phi, p, t) = q(\lambda, \phi, \beta p, t). \tag{5.8}$$

We prescribe that both the relative humidity, $\mathcal{R}$, and saturation specific humidity, q_s, are similarly vertically shifted, so that (5.8) is satisfied, and the equation governing conservation of water vapor,

$$\frac{Dq}{Dt} = -c, \tag{5.9}$$

is also satisfied, assuming that the net condensation rate, c, is a local function of variables such as the relative humidity, specific humidity, and winds.

The saturation specific humidity, q_s, is a thermodynamic function of pressure and temperature, and so its transformation depends on the transformation of temperature. We may express the saturation specific humidity as a function of the saturation vapor pressure e_s via,

$$\frac{q_s}{1 - \left(1 - \frac{1}{\epsilon}\right) q_s} = \frac{\epsilon e_s(T)}{p}, \tag{5.10}$$

where ϵ is the ratio of gas constants for dry air and water vapor. We assume a small upward shift ($\beta - 1 \ll 1$) and that ΔT is small enough to allow linearization of the dependence of saturation vapor pressure on temperature. Substituting the transformed temperature (5.7) into (5.10) and performing this linearization, we find that

$$\frac{q'_s(p)}{1 - \left(1 - \frac{1}{\epsilon}\right) q'_s(p)} = \left[\beta\left(1 - \frac{L_v}{R_v T(\beta p)\theta(\beta p)}\Delta\theta\right)\right] \frac{\epsilon e_s(\beta p)}{p},$$

where R_v is the gas constant for water vapor, the Clausius-Clapeyron equation has

been used, and the dependence on horizontal coordinates and time has been suppressed for brevity. In the above equation, $q'_s(\lambda, \phi, p, t) = q_s(\lambda, \phi, \beta p, t)$ holds if the term in square brackets is equal to unity, that is, if

$$\Delta\theta = \left(\frac{\beta - 1}{\beta}\right)\left(\frac{R_v}{L_v}\right) T\theta. \tag{5.11}$$

This will only be strictly satisfied if the product $T\theta$ is constant, since both β and $\Delta\theta$ must not vary in space or time. In practice, the relation (5.11) will be most important in regions in which latent heating is a significant term in the thermodynamic equation. In the low to mid-troposphere, where latent heating is important, temperature decreases with height and potential temperature increases with height, with the result that for atmospheric profiles typical of Earth's atmosphere, the function $T\theta$ does not vary by more than ten percent between the surface and upper troposphere. We will further discuss the approximation of constant $T\theta$ and the errors it introduces in section 5.3.

5.2.4 Radiation

The vertical-shift transformation of the thermodynamic equation (5.6) is only valid if the radiative cooling rate in the atmosphere is also shifted vertically,

$$Q'_{rad}(\lambda, \phi, p, t) = Q_{rad}(\lambda, \phi, \beta p, t). \tag{5.12}$$

The extent to which the radiative cooling rate shifts upwards with warming has been discussed to some extent in previous studies (Hartmann and Larson, 2002; Ingram, 2010). The rate of radiative cooling in the free troposphere does not vary strongly in the vertical (e.g. Dopplick, 1972; Hartmann et al., 2001), and thus the most important issue is whether the upper limit of the region of strong radiative cooling shifts vertically in accordance with the transformation. One way for this to occur is if the radiative cooling rate declines at a level determined by the distribution of specific humidity (specific humidity and radiative cooling shift vertically in the same

way according to the transformation), in a similar way to the FAT hypothesis mentioned in the introduction (Hartmann and Larson, 2002). Simulations with cloud system resolving models have shown that the tropical cloud distribution does follow the FAT hypothesis, even with changes to the ozone distribution and CO_2 concentrations (Kuang and Hartmann, 2007). In the extratropics, however, there is less justification for this simplified view of the radiative response of the atmosphere.

5.2.5 Boundary conditions

The surface boundary conditions are not satisfied in detail by the transformation. We can, however, ensure that the boundary conditions on geopotential and temperature are satisfied to some extent. An immediate problem is that for a finite upward shift ($\beta > 1$), there is a region near the surface in which the transformed solution is not defined, as it refers to the original solution below the surface, and the transformed solution must be extrapolated. This issue is less problematic the smaller the climate change, and it does not arise for the downward shift associated with a cooling climate. More importantly, because we only expect the transformed solution to be valid above the boundary layer (the boundary layer tendencies are strongly tied to the surface and cannot shift upwards[5]), the boundary conditions should be applied at or above the top of the boundary layer rather than at the surface.

We begin with the boundary condition on the geopotential, Φ, and impose the requirement that the mass of the free-troposphere is unchanged by the transformation. Since only the first derivative of $\Lambda(p)$ is constrained by the combination of (5.5) and (5.11), we can introduce an integration constant $\Delta\Phi$ to set the geopotential near the top of the boundary layer. The remaining parameters in the transformation, β and $\Delta\theta$, are related by (5.11), and thus may be used to satisfy only one boundary condition, which we take to be temperature. (In practice, we will choose β using

[5]Additionally, the derivation assumes an inviscid atmosphere and is not a good approximation in the boundary layer in which small-scale turbulent eddies are dynamically important. While these eddies themselves are governed by the Navier-Stokes equations and could be encapsulated within the transformation, the hydrostatic form of the equations used is more appropriate for large-scale flow. Also, in the case of climate models, small-scale turbulence is often parameterized by schemes that do not respect the equations of motion.

a least-squares criterion based on global temperature changes above the boundary layer.) The need to satisfy the boundary conditions at all positions and times introduces a further approximation, since the transformation parameters must be constant. The inability of the transformation to satisfy the boundary conditions on wind and relative humidity will be seen to be the largest contributor to the mismatch between the responses to climate change given by the transformation and the simulations in sections 5.4 and 5.5.

5.2.6 Summary of transformation

The result of the preceding derivation is that for any solution to the moist primitive equations, we can find a family of new solutions using the following transformation:

$$u'(\lambda, \phi, p, t) = u(\lambda, \phi, \beta p, t), \tag{5.13a}$$

$$v'(\lambda, \phi, p, t) = v(\lambda, \phi, \beta p, t), \tag{5.13b}$$

$$\omega'(\lambda, \phi, p, t) = \frac{\omega(\lambda, \phi, \beta p, t)}{\beta}, \tag{5.13c}$$

$$\begin{aligned} \Phi'(\lambda, \phi, p, t) &= \Phi(\lambda, \phi, \beta p, t) \\ &\quad + c_p \Delta\theta \, \Pi(\beta p) + \Delta\Phi, \end{aligned} \tag{5.13d}$$

$$T'(\lambda, \phi, p, t) = T(\lambda, \phi, \beta p, t) - \Delta\theta \, \Pi(\beta p), \tag{5.13e}$$

$$\mathcal{R}(\lambda, \phi, p, t) = \mathcal{R}(\lambda, \phi, \beta p, t), \tag{5.13f}$$

$$Q'_{rad}(\lambda, \phi, p, t) = Q_{rad}(\lambda, \phi, \beta p, t). \tag{5.13g}$$

The parameter β determines the magnitude of the vertical shift (and is set by the temperature change), $\Delta\Phi$ is used to satisfy the boundary condition on geopotential, and $\Delta\theta$ is given by (5.11). Figure 5-2 shows a schematic of how the transformation affects typical profiles of temperature, zonal wind and pressure velocity. In particular, the temperature and pressure velocity are not simply shifted vertically (as shown by the gray dashed lines), but a pressure-dependent offset is applied to the temperature, and the pressure velocity is decreased in magnitude.

Some further insight is gained by explicitly relating β to the change in tempera-

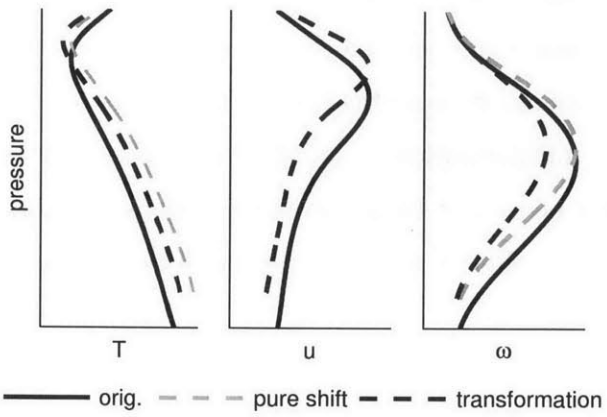

Figure 5-2: Schematic of the effect of the transformation on temperature (left), zonal wind (middle) and pressure velocity (right). Solid lines show the original solution and dashed lines show the transformed solution. For comparison, gray dashed lines show a pure upward shift for temperature and pressure velocity neglecting the extra terms introduced by the transformation [see eq. (5.13c,e)].

ture. Substituting the expression (5.11) for $\Delta\theta$ into (5.13e) and discarding terms of order $(\beta-1)^2$ or higher gives

$$T'(\lambda,\phi,p,t) \simeq T(\lambda,\phi,p,t) + (\beta-1)p\frac{\partial T}{\partial p} - (\beta-1)\frac{R_v}{L_v}T^2.$$

Denoting δT as the difference in temperature between the original and warm climate at a fixed pressure level, we have that

$$\delta T \simeq (\beta-1)\left[p\frac{\partial T}{\partial p} - e_s\frac{dT}{de_s}\right],$$

where the Clausius-Clapeyron equation has been used. The sensitivity of the upward shift to temperature change may then be written as

$$\frac{\beta-1}{\delta T} \simeq \left[(H_p - H_e)\,\Gamma\right]^{-1}, \tag{5.14}$$

where H_p and H_e are the scale heights for pressure and water vapor, respectively,

defined by

$$H_p = -\frac{\partial z}{\partial \ln p},$$
$$H_e = -\frac{\partial z}{\partial \ln e_s},$$

with z the geopotential height, and $\Gamma = -\partial T/\partial z$ the lapse rate. Substituting characteristic top-of-boundary-layer values of $H_p \simeq 8$ km, $e_s^{-1} de_s/dT \simeq 0.07$ K^{-1} and $\Gamma \simeq 5$ K km^{-1}, we find that

$$\frac{\beta - 1}{\delta T_{BL}} \approx 0.04 \text{ K}^{-1}, \tag{5.15}$$

where δT_{BL} is the change in temperature at a fixed pressure level near the top of the boundary layer. This value of β is somewhat sensitive to the assumed lapse rate, but it gives a rough sense of the magnitude of vertical shift that may be expected for a given level of warming.

It is also possible to formulate the transformation in geopotential height coordinates (z), in which case the vertical shift becomes more explicit. For example, the transformation of the zonal wind may be written as

$$u'(\lambda, \phi, z, t) = u(\lambda, \phi, z - \Delta z, t),$$

where Δz is the vertical shift in height. The pressure and density fields are shifted up similarly but must also be divided by β. The equivalence of the pressure and height formulations follows from the transformation of the geopotential in (5.13d). In the case of a dry atmosphere, we can take $\Delta\theta = 0$, and the vertical shift Δz is a constant; the transformation follows from translational invariance and the form of the ideal gas law. In the more general case of a moist atmosphere, the vertical shift Δz varies in the vertical, and it becomes much easier to demonstrate the validity of the transformation using pressure coordinates. We will refer to the transformation as a vertical shift for convenience, even though the magnitude of the vertical shift varies with height, and even though the temperature change is not purely a vertical shift.

5.3 Parcel ascents

We begin the evaluation of the vertical-shift transformation in the simplified setting of idealized parcel ascents in which we only consider temperature and moisture. This approach allows us to examine the effects of the approximations made in the derivation related to the latent heating term in the thermodynamic equation (cf. section 5.2.3).

For a dry-adiabatic parcel ascent or descent, we have that the potential temperature is uniform. Increasing the initial parcel temperature yields a temperature profile with a constant but higher potential temperature. The transformation gives the exact warmer solution by construction regardless of the combination of β and $\Delta\theta$ that is used to match the increase in initial temperature. The requirement that $T\theta$ be constant does not enter because (5.11) is only required to hold when moisture affects the thermodynamic equation. Thus, the vertical-shift transformation can exactly reproduce a shift to a warmer "climate" in the case of dry adiabatic displacements.

Moist-adiabatic parcel ascents are a non-trivial test because of the approximations made in the derivation related to the simplified expression for the saturation specific humidity (5.10) and the requirement of approximately constant $T\theta$ for the transformed thermodynamic budget to be accurate. We evaluate the accuracy of the transformation for pseudo-adiabatic parcel ascents. For simplicity we assume a constant latent heat of vaporization and neglect ice processes, consistent with the idealized simulations described in the next section. Figure 5-3 shows an example of one such ascent for a surface temperature of 300 K and a surface relative humidity of 80%. The ascents follow a dry adiabat up to saturation, and the air parcels are assumed to remain at saturation for the remainder of the ascent. We choose a surface air temperature characteristic of the tropics because the tropics are where condensation, and thus the constraint of invariant $T\theta$ given by (5.11), is most important. The product $(T\theta)^{1/2}$ remains roughly constant up to a pressure of around 300hPa, varying by only 2% between the surface and this level, implying that the vertical-shift transformation should work well in this case. Latent heating is weaker at levels above 300hPa, and the condition of constant $T\theta$ is less dynamically important, although

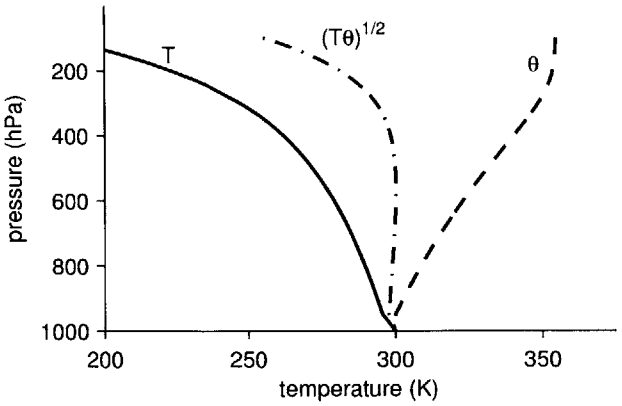

Figure 5-3: Pseudo-adiabatic parcel ascent with a surface temperature of 300 K and surface relative humidity of 80%. Shown are the temperature T (solid), potential temperature θ (dashed), and their geometric mean $(T\theta)^{1/2}$ (dot-dashed).

the transformation of specific humidity may still matter for the effect of water vapor on radiative transfer.

We next consider the application of the vertical-shift transformation to the difference in temperature between pseudo-adiabatic ascents with surface relative humidities of 80% and surface temperatures of 300 K (the control parcel) and 302 K (the warm parcel). The vertical-shift transformation is applied to the control parcel in order to reproduce the warm parcel ascent (Fig. 5-4a), and the implied difference in temperature is compared with the actual difference in temperature between the two parcel ascents (Fig. 5-4b). The value of β used for the vertical-shift solution is determined using a least-squares criterion in which we minimize the non-dimensional error function

$$E^2 = \frac{\overline{(T_W - T_V)^2}}{\overline{(T_W - T_C)^2}}, \tag{5.16}$$

where T_W, T_C and T_V are the temperatures of the warm parcel ascent, control parcel ascent, and vertical-shift solution. The overbar denotes a mass-weighted mean from 150 hPa above the lowest level at which the vertical-shift solution is well defined to the top of the atmosphere. (The value of β is insensitive to the precise choice of the levels used to evaluate it.) Once β is determined, the value of $\Delta\theta$ is calculated using (5.11) with the value of $T\theta$ evaluated at 600 hPa.

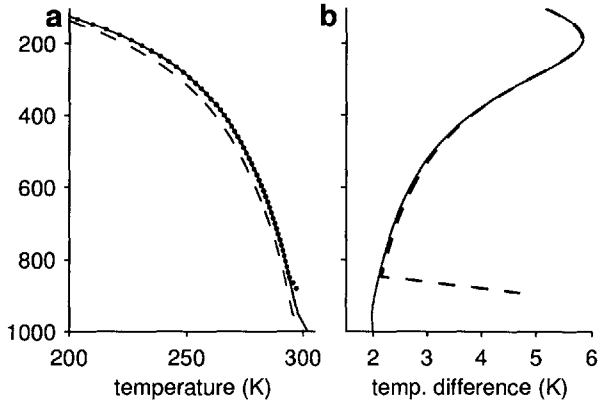

Figure 5-4: (a) Pseudo-adiabatic parcel ascents with surface temperatures of 300 K (dashed) and 302 K (solid), and surface relative humidity of 80% in both cases. The dotted line is an approximation of the 302 K parcel ascent calculated from the 300 K ascent using the vertical-shift transformation with $\beta = 1.122$ (corresponding to $\Delta\theta = 1.81$ K). Each adiabat is sampled at 1 hPa intervals, and the transformation is calculated by linear interpolation of the control parcel in pressure. (b) The temperature difference between the 300 K and 302 K parcel ascents (solid) and the difference calculated from the transformation (dashed).

Apart from the dry adiabatic region of the profile below the lifted condensation level (LCL)[6], the vertical-shift transformation is able to reproduce the temperature change remarkably well (Fig. 5-4). The minimized value of the error E [defined by (5.16)] is 0.7%. The minimized value of E is much greater (9%) if a pure upward shift in temperature is used instead of the full vertical-shift transformation (i.e., if only the parameter β is used and $\Delta\theta$ is set to zero). This shows that it is the precise combination of β and $\Delta\theta$ given by the transformation itself that allows for such a close agreement; a pure upward shift in temperature performs over ten times worse. The value of $\beta = 1.122$ found from the least-squares minimization is larger than the value of $\beta \approx 1.08$ implied by the approximate relation between β and the near-surface temperature change found earlier (5.15). But if a lapse rate of 4 K km^{-1} is used in the evaluation of (5.14) (closer to the actual lapse rate of the parcel ascents above the dry-adiabatic layer), a value of $\beta \approx 1.11$ is obtained, which is in better agreement with the result of the least-squares minimization.

[6]The mismatch at low levels results from the use of a constant surface relative humidity for both parcels, which implies that the LCL does not shift upwards in accord with the transformation.

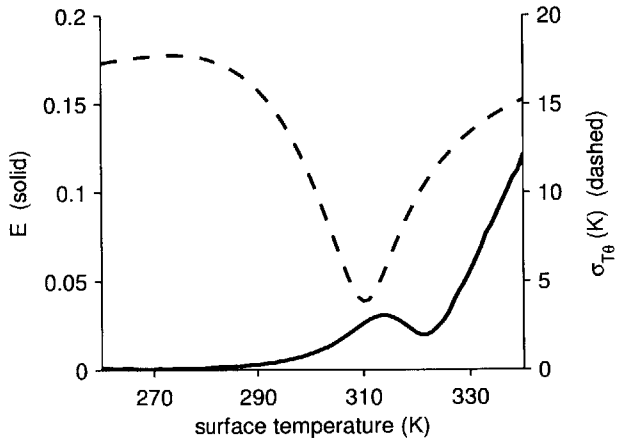

Figure 5-5: Solid line (left axis) shows minimized error function, E, defined by (5.16), as a function of control parcel surface temperature. Dashed line (right axis) shows standard deviation of $(T\theta)^{1/2}$ over the same pressure range used to calculate E.

We next quantify the temperature dependence of the accuracy of the transformation by repeating the procedure used to create Fig. 5-4 for a range of surface temperatures of the control parcel. In each case, the vertical-shift transformation is applied to the control parcel ascent in order to estimate the temperature profile of a parcel ascent with a surface temperature 2 K higher and the same surface relative humidity (80%). The magnitude of vertical variation in $T\theta$ is measured here by the standard deviation

$$\sigma_{T\theta} = \left\{ \overline{\left[(T\theta)^{1/2} - \overline{(T\theta)^{1/2}} \right]^2} \right\}^{1/2},$$

where the overbar denotes the same mass-weighted mean used to determine β. The transformation is very accurate for low surface temperatures (Fig. 5-5), which makes sense given that it is exact in the limit of dry adiabatic ascent. The error E increases as the surface temperature increases, up to around 315 K, dropping to a local minimum at 322 K. At around these temperatures $T\theta$ becomes close to constant in the vertical - the value of $\sigma_{T\theta}$ reaches a minimum at 312 K. At higher temperatures, the error E grows rapidly with temperature and the fidelity of the transformation breaks down, reflecting the decreasing accuracy of the assumption of constant $T\theta$. Over the range of typical Earth-like surface temperatures, however, the vertical-shift transformation

performs well in reproducing the warm ascents, and the error E is typically below 2%. It will be shown in the following section that the errors introduced by mismatches in the boundary conditions are likely to be more important than the errors related to the transformation of latent heating that have been quantified in this section.

5.4 Idealized general circulation model

We next discuss atmospheric GCM simulations in which we test the ability of the transformation to capture changes in the distributions of temperature, moisture, and winds as the surface temperature is increased. In order to focus on the dynamical accuracy of the transformation, we use a "radiation scheme" in which the radiative cooling of the atmosphere conforms to the vertical-shift transformation by depending primarily on the local specific humidity; GCMs with more realistic treatments of radiative transfer are discussed in section 5.5.

5.4.1 Model configuration

The idealized general circulation model is based on a version of the dynamical core of the Flexible Modeling System of the Geophysical Fluid Dynamics Laboratory (GFDL) with spectral dynamics run at T42 resolution in the horizontal and 30 levels in the vertical. Several aspects of the model formulation are similar to that of Frierson et al. (2006) and O'Gorman and Schneider (2008), but with different surface boundary conditions and a different radiation scheme. We use the simplified quasi-equilibrium moist convection scheme of Frierson (2007), a large-scale condensation scheme to prevent grid-box supersaturation, and boundary layer parameterizations similar to that of Frierson et al. (2006) [see O'Gorman and Schneider (2008) for precise details]. One should note that the convective and boundary layer parameterizations do not respect the moist primitive equations used to derive the vertical-shift transformation, and it is not obvious *a priori* to what extent the transformation will be applicable in regions in which convective or boundary layer tendencies are strong.

Our control simulation has a fixed and zonally symmetric SST distribution given

by

$$T_s = T_0 + \Delta_h \left(\frac{1}{3} - \sin^2 \phi \right), \tag{5.17}$$

with $T_0 = 290$ K and $\Delta_h = 30$ K. The radiative tendency depends primarily on the specific humidity q as follows

$$Q_{rad} = \begin{cases} -Q_0, & q > q_0, \\ -\left(T - T_{\text{strat}}\right)/\tau, & q < q_0, \end{cases} \tag{5.18}$$

where $q_0 = 0.01$ g kg^{-1}, $Q_0 = 1$ K day^{-1}, $T_{\text{strat}} = 200$ K, and $\tau = 40$ days. The radiative cooling rate is constant in the troposphere (for specific humidities above q_0, corresponding to saturation at a temperature of around 200K for a pressure of 200hPa) and involves a relaxation to a constant temperature in the stratosphere (for specific humidities below q_0). The form of the imposed radiative cooling ensures that if the temperature and relative humidity transform according to the vertical-shift transformation, then so too will the tropospheric radiative cooling. The stratospheric relaxation does not conform exactly to the transformation but is required to ensure stability of the simulation. The radiative tendencies (5.18) tend to give a tropopause near a temperature of 200 K, and this should be taken into account when interpreting upward shifts near the tropopause.

In addition to the control simulation, we also ran a warm simulation with the SST uniformly increased by 2 K. After a spin-up period, zonal- and time-mean statistics were calculated over 3600 days in each simulation. The mean state of the control simulation (Fig. 5-6) has a single jet in each hemisphere. The strength of the Hadley cells and the global-mean precipitation rate are within a factor of two of those in the annual mean of Earth's current climate.

5.4.2 Results

The transformation is applied to zonal- and time- mean variables of the control simulation in order to predict the simulated response to a uniform 2 K increase in surface temperature. The value of β is chosen by minimizing an error function similar to

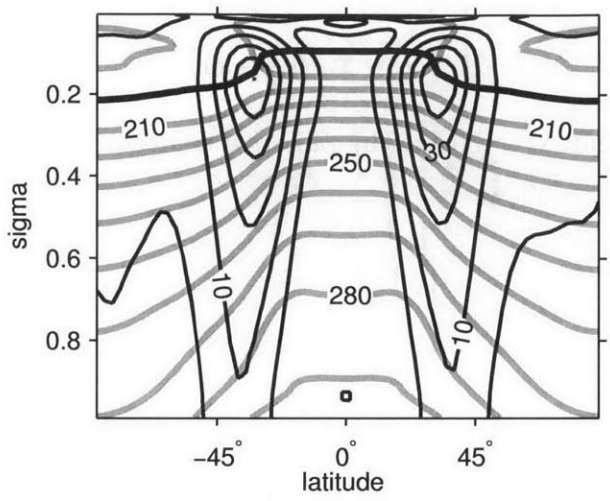

Figure 5-6: Mean state of the control simulation conducted using the idealized GCM described in the text. The zonal wind (black, contour interval 10 m s^{-1}) and temperature (gray, contour interval 10 K) are shown. The tropopause (thick line) is defined as the level at which the mean lapse rate is equal to 2 K km^{-1}.

that used for the parcel ascents and defined by (5.16). In this case, T_W and T_C correspond to the zonal- and time-mean temperatures of the warm and control simulation, respectively, while T_V is the temperature obtained from the application of the the vertical-shift transformation to the temperatures in the control simulation. The mass-weighted mean is taken over all latitudes and all levels above $\sigma = 0.6$[7]. The value of $\Delta\theta$ is calculated using (5.11) and the global mean of $T\theta$ at $\sigma = 0.6$. These transformation parameters are then used to calculate the transformed values for all other variables. As a result, the magnitude of the upward shift is determined using the simulated change in temperature, but it is independent of the simulated changes in other variables. The values of $(\beta - 1)/\delta T_s$ and $\Delta\theta/\delta T_s$ found using this procedure are 0.05 K^{-1} [roughly consistent with (5.15)] and 0.69, respectively. Here, $\delta T_s = 2$ K is the change in global-mean SST between the control and warm simulations.

The transformation requires that fractional variations in $T\theta$ are small in order for latent heating to transform correctly. In applying the transformation to GCM simula-

[7]The lower level used in the calculation of β is chosen to be above the region of the atmosphere in which the transformed solution refers to regions with substantial boundary-layer temperature tendencies in the original solution (see hatching in Fig. 5-7). The value of β obtained is insensitive to the precise choice of lower level used.

tions, both vertical and horizontal variations in $T\theta$ must be considered. The surface temperature varies by 30 K between equator and pole in the simulation described here, implying a non-negligible fractional variation in $T\theta$ of roughly 0.2. But latent heating is most important in the tropics where meridional temperature gradients are relatively small, and thus the errors induced by this approximation may not be very significant.

Differences in zonal- and time-mean temperature, lapse rate, relative humidity, and meridional mass streamfunction between the control and warm simulations are shown in Fig. 5-7 (left panels). The right panels show the same differences estimated from the control climatology using the vertical-shift transformation. Given its simplicity, the vertical-shift transformation performs surprisingly well in emulating the response to a uniform increase in SST. The response of the temperature distribution is relatively well captured in the tropics and polar regions, although the warming in the upper troposphere is too strong in the mid-latitudes (Fig. 5-7a). The inability to precisely capture the midlatitude temperature response may be a result of a different value of β being appropriate there; in the appendix to this chapter (section 5.7) it is shown that the temperature response is captured with considerable fidelity at all latitudes if β is allowed to vary in latitude. The improvement afforded by allowing β to vary is less pronounced for other variables, however, and the validity of the transformed solution as a solution to the governing equations is reduced. We continue to analyze results using a single value of β globally, noting that the transformation then involves only a single tunable parameter while describing changes to the entire general circulation.

The changes in temperature lapse rate are shown in Fig. 5-7b, and are well captured except in the lower troposphere at high latitudes. The increase in tropopause height is also captured, although some of this may be directly attributable to the constraint on tropopause height imposed by the specified dependence of radiative cooling on specific humidity. The transformation does not capture the lapse-rate response close to the boundary below which the transformed solution is no longer well defined ($\sigma = 1/\beta$). As discussed in section 5.2.5, this is to be expected because of

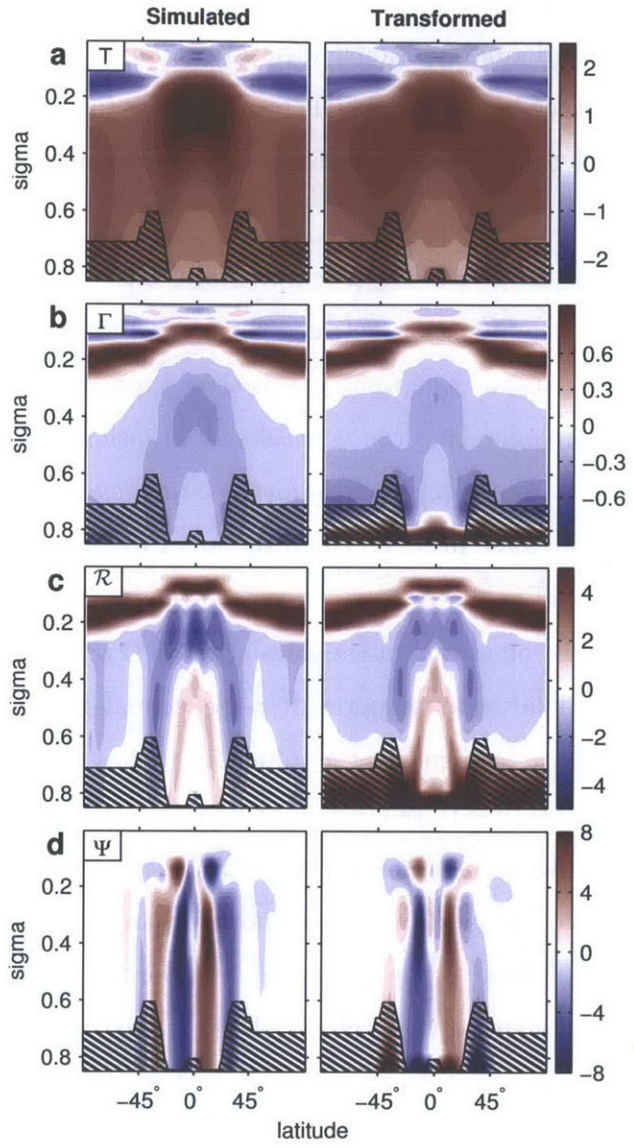

Figure 5-7: Normalized differences between the control and warm simulations (left) and the same differences calculated using the vertical-shift transformation (right). Changes in zonal- and time-mean (a) temperature (K), (b) lapse rate (K km^{-1}), (c) relative humidity (%) and (d) meridional mass streamfunction (10^9 kg s^{-1}), all normalized by the change in SST between simulations (2 K). The hatching shows where the vertical-shift transformation may refer to regions in the control simulation with substantial boundary-layer tendencies (see text). Interhemispheric asymmetries are indicative of sampling error.

the effects of boundary-layer processes; the regions marked with hatching in Fig. 5-7 give an indication of where the transformed solution refers to regions in the control simulation with substantial parameterized boundary-layer tendencies of temperature. The region of substantial boundary-layer tendencies in the control simulation is taken to extend to the highest level at which the magnitude of the mean temperature tendencies from the boundary layer scheme are above 1×10^{-6} K s^{-1} (roughly one tenth of their maximum value).

The transformation also captures much of the simulated response of relative humidity, both in the overall structure, and, to a lesser degree in magnitude, including a complicated pattern of increases and decreases in equatorial and subtropical regions (Fig. 5-7c). As for the lapse-rate, the errors in the transformation largely occur in the lower part of the troposphere, and much of the disagreement is confined to regions influenced by strong boundary-layer tendencies.

Changes in the meridional mass streamfunction also show similarities in the simulated and transformed responses. In both cases there is a decrease in strength of both the Hadley and Ferrel cells over most of the troposphere, with small increases near the tropopause relating to an upward extension of the circulation. However, the quantitative changes in the streamfunction are generally less-well predicted by the transformation than in the case of the relative humidity field, especially in the extratropics. Some of these differences may be a result of sampling error, as evidenced by the departures from interhemispheric symmetry of the simulated response of the mass streamfunction (since the boundary conditions are symmetric between the hemispheres). Considerable low-frequency variations in the streamfunction may be related to annular mode like variation that is known to have long time-scales in aquaplanet models (Cash et al., 2002). We measure the Hadley cell strength as the maximum in the absolute value of the zonal- and time-mean streamfunction, averaged between hemispheres. The vertical-shift transformation implies a decrease of $\sim 6\%$ K^{-1} in Hadley cell strength relative to the change in global-mean surface air temperature, while the simulated response is considerably weaker ($\sim 3\%$ K^{-1}). The transformation also predicts a weakening of the Ferrel cell in response to surface warming, and this

is indeed what occurs in the simulations, albeit at a lesser rate than given by the transformation.

The vertical-shift transformation does not capture the response of the mean zonal wind (Fig. 5-8a). While there are some similarities in the simulated and transformed changes in the low- and mid-latitude upper troposphere, the transformation implies a decrease in the strength of the wind below the jets that is too strong and an increase above that is too weak. There are also simulated decreases in the zonal wind at high latitudes that the vertical-shift transformation does not capture. On the other hand, the response of the mean meridional wind in the idealized GCM simulations forms a complex pattern of increases and decreases in the upper troposphere that is remarkably well captured by the vertical-shift transformation (Fig. 5-8b). The changes in meridional- and zonal- wind variances are also well described by the transformation, with increases in the upper troposphere and decreases below, the largest changes occurring near the location of the jet (Fig. 5-8c,d). The decrease implied by the transformation is slightly too strong, while the increase is slightly too weak, resulting in less eddy-activity overall in the transformed climate than occurs in the warm simulation. The reduction in eddy activity and associated meridional fluxes of zonal momentum implied by the transformation could be thought to be consistent with the transformed reduction in lower-tropospheric mean zonal winds, although there is no requirement for the vertical-shift transformation to respect the vertically-integrated zonal momentum budget in this way. Rather, the inaccuracy for the changes in zonal winds are likely related to the inability of the transformation to satisfy the surface boundary condition for zonal wind.

Overall, the extent to which the transformation reproduces the simulated changes in the idealized GCM simulations is remarkable given the simplicity of the transformation. It should also be stressed that the transformation has only one free parameter, which is fit using the global temperature response, and which does not depend on the response in humidity or wind fields. To summarize the results, Fig. 5-9 shows a Taylor diagram comparing the transformed response in each variable to the simulated response (see Taylor, 2001). Standard deviations and correlation coefficients of the

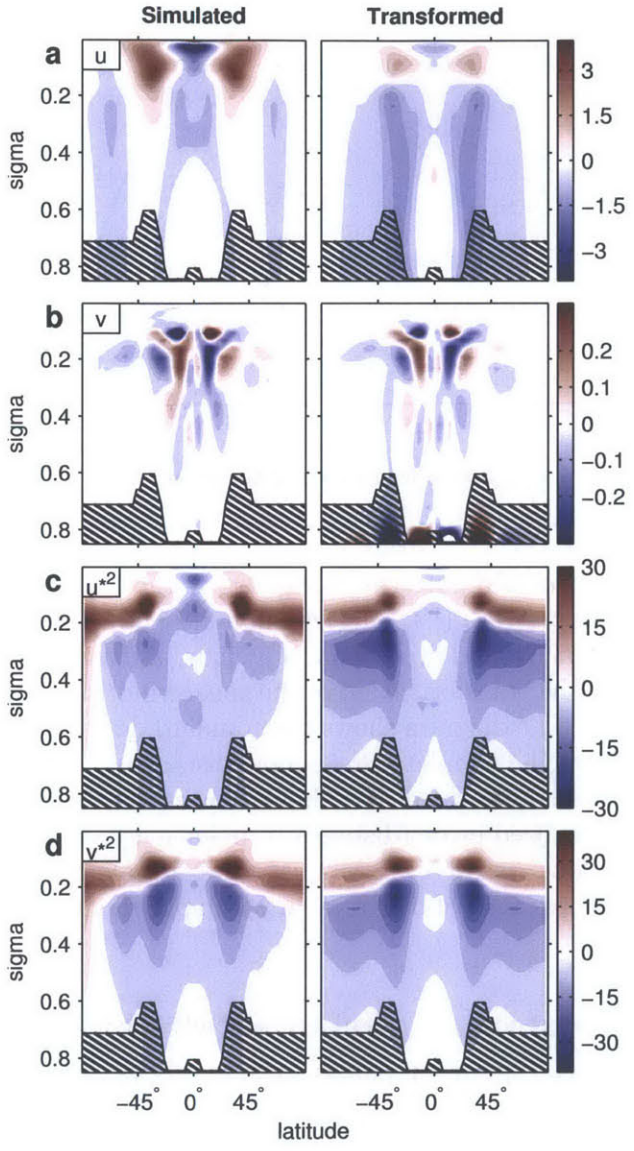

Figure 5-8: As in Fig. 5-7 but for normalized changes in (a) zonal- and (b) meridional-mean winds (m s^{-1}), and (c) zonal- and (d) meridional- wind variances (m^2 s^{-2}). The variances are calculated using four-times daily data with respect to a zonal and time mean.

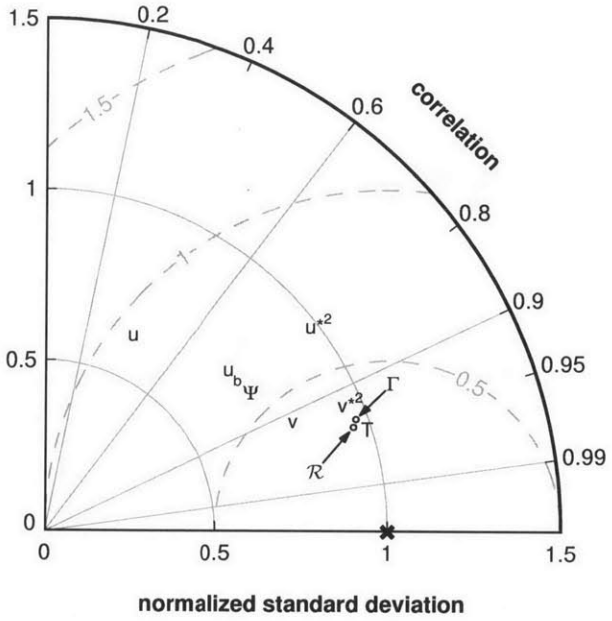

Figure 5-9: Normalized Taylor diagram quantifying the degree of similarity between the simulated and transformed patterns of response in the idealized GCM simulations for temperature (T), lapse rate (Γ), relative humidity ($\mathcal{R}$), meridional mass streamfunction (Φ), mean zonal (u) and meridional (v) winds, and zonal (u^{*2}) and meridional (v^{*2}) wind variances. The transformation of the zonal wind with a barotropic offset is shown as u_b (see text). The diagram shows the standard deviation of the transformed response normalized by the simulated response (distance to origin), the correlation coefficient between the transformed and simulated response (cosine of angle to the abscissa) and the normalized error (distance to point marked "X"). The error value does not include the global-mean bias. All quantities are calculated based on averages over all latitudes and pressures above $\sigma = 0.6$ with appropriate mass weighting.

responses and their differences are calculated globally for levels above $\sigma = 0.6$ and with mass weighting. The standard deviations shown in the diagram are normalized by the standard deviation of the simulated response in each case. The normalized standard deviation is close to one for all variables except for the mean zonal wind, which supports the existence of a coherent upward shift across variables as implied by the transformation. With the exception of the mean zonal wind, all variables have correlation co-efficients greater than 0.8 and normalized errors less than roughly 0.6. The normalized error shown is the pattern root-mean-square difference (Taylor, 2001) and does not include the mean bias. The mean bias is generally less than 10% of the

total error.

Figures 5-8 and 5-9 show that the transformation captures less of the simulated response of the mean zonal wind as compared to other variables. The difference between the simulated and transformed responses in mean zonal wind may be decomposed into components associated with near-surface wind changes (which we will refer to as the barotropic component) and a baroclinic component that is primarily related to changes in horizontal temperature gradients. The baroclinic component may be isolated by allowing for a latitude-dependent (but height-independent) offset Δu to be added to the transformation in order to match the barotropic component of the simulated changes. Indeed, this offset could be included in the framework of the transformation using the Galilean invariance of the tangent plane equations in the zonal direction, although we do not pursue this in detail here. The fidelity of the transformation including this offset is shown by the point marked u_b in Fig. 5-9. The offset is calculated as the difference between the simulated and transformed mean zonal wind at each latitude and at the lowest level at which the transformation is well defined. Other definitions using multiple levels give similar results. Inclusion of the barotropic offset leads to some improvement in the match with the simulated response, but the mean zonal wind remains one of the variables most poorly captured by the transformation. In the next section we consider simulations in the CMIP3 ensemble for which the barotropic offset is found to improve the fidelity of the transformed zonal wind to be on a par with the lapse-rate and relative humidity. Part of the reason for this difference may be that a poleward shift in the mid-latitude jet occurs in the CMIP3 simulations (e.g. Fyfe et al., 1999; Yin, 2005) but does not occur to the same extent in the idealized GCM simulations. The poleward shift cannot be captured by the vertical-shift transformation, and it increases the component of the error that resides in the barotropic component. This is also a difference between the idealized GCM results shown here and those of Lorenz and DeWeaver (2007), who found that a poleward (and upward) shift of the jets resulted from raising the tropopause height in a dry idealized GCM.

5.5 Comprehensive general circulation models

We next apply the vertical-shift transformation to simulations of climate change from the third Coupled Model Intercomparison Project (CMIP3). We examine results from ten fully coupled atmosphere-ocean GCMs[8], using the period 1981-2000 of the 20th century simulations as the control climate and the period 2081-2100 under the forcing scenario SRESA1b (Nakićenović et al., 2000) as the warm climate. (An example of the application of an upward shift to the change in cloud fraction in one such model is shown in Fig. 1, although cloud fraction is not explicitly included in the transformation discussed here.) In contrast to the idealized GCM simulations, the CMIP3 simulations include realistic representations of radiative transfer and ice processes, and thus the conditions on the radiative cooling and humidity fields required for the transformation to be valid may not be satisfied. Nevertheless, we will show that a substantial portion of the response to warming in simulations with comprehensive GCMs may be described using the vertical-shift transformation with a single tunable parameter.

The vertical-shift transformation is applied individually in each climate model to zonal- and annual-mean fields of the control climate to give an estimate of the general circulation in the warm climate. As in the application to the idealized GCM simulations in section 5.4, a value of β is found to best match the global temperature changes, and the same value of β is used to calculate the change in all other fields. The fitting procedure is the same as for the idealized GCM – the mean-squared difference between the warm-climate temperature field and that from the transformation is minimized over all latitudes and levels above the 600 hPa pressure level. The resulting value of $(\beta - 1)/\delta T_s$ varies between 0.036 and 0.048 K^{-1} between models, with an ensemble mean value of 0.044 K^{-1} [roughly consistent with (5.15)]. The

[8]The models used are BCCR-BCM2.0, GFDL-CM2.0, GFDL-CM2.0, CNRM-CM3, CSIRO-Mk3.5, ECHAM5, FGOALS-g1.0, INM-CM3.0, MIROC3.2-medres and MRI-CGCM2.3.2. Only the first three models are used in the calculation of ensemble-mean wind variances (Fig. 5-12c,d) because only these models had daily wind data available above 200 hPa; the results are similar below 200 hPa for the entire ensemble. The pressure velocity was not available for BCCR-BCM2.0 and CSIRO-Mk3.5, and these models are excluded from the calculation of ensemble-mean changes in pressure velocity (Fig. 5-11).

associated ensemble mean value of $\Delta\theta/\delta T_s$ is 0.59, ranging between 0.51 and 0.67 among models. Here, δT_s is the change in global-mean surface air temperature. Differences between the control and warm climate for each model are also normalized by δT_s before being combined into an ensemble mean, both for the simulated differences and the differences given by the vertical-shift transformation. While we only show ensemble-mean quantities, the vertical-shift transformation has a similar level of accuracy when applied to climate change in individual model simulations.

5.5.1 Temperature and moisture

The temperature change implied by the transformation compares well with the simulated temperature change (Fig. 5-10a), although, as in the case of the idealized GCM there is too much warming in the midlatitude troposphere. The ability of the transformation to capture the vertical structure of the changes in the middle and upper troposphere is also clearly demonstrated for the lapse-rate changes (Fig. 5-10b). The ability to capture the large lapse-rate changes associated with the increase in tropopause height is notable given that realistic radiative transfer is used in these models (unlike in the idealized GCM in which the radiative cooling was prescribed to shift upwards with specific humidity). Lorenz and DeWeaver (2007) reported similar results for the lapse rate changes in CMIP3 models but with a focus on the tropopause region and using a pure upward shift for temperature that does not capture the changes in mid-tropospheric lapse rate.

The vertical-shift transformation captures changes in relative humidity associated with the increase in tropopause height, as well as decreases in relative humidity in the tropical upper troposphere and subtropics (Fig. 5-10c). Sherwood et al. (2010) also showed that upward shifts account for a significant part of the relative humidity response in CMIP3 models, including different responses in different models because of their different climatologies of mean relative humidity.

The vertical-shift transformation is much less accurate in reproducing lower-tropospheric changes in lapse rates and relative humidities. Figure 5-10 only shows changes above 700 hPa since, as discussed previously, the transformation breaks down in the bound-

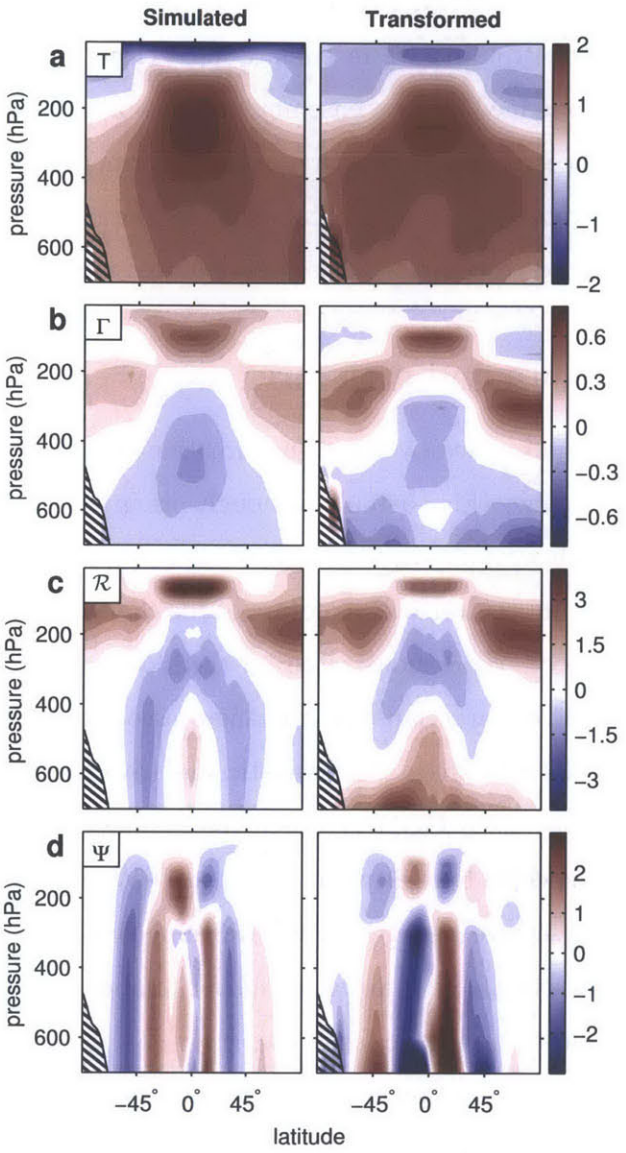

Figure 5-10: Ensemble-mean of the normalized changes in zonal- and time-mean variables between the 20th century simulation (1981-2000) and the SRESA1b scenario (2081-2100) in CMIP3 models. Left panels show the simulated changes and right panels show the changes calculated from the vertical-shift transformation. Changes in (a) temperature (K), (b) lapse-rate (K km^{-1}), (c) relative humidity (%) and (d) meridional mass streamfunction (10^9 kg s^{-1}), all normalized by the change in global-mean surface air temperature (K) prior to taking the ensemble mean. Hatching indicates regions in which boundary effects are likely to be important (see text).

ary layer. The lowest level at which the transformation may be applied is taken to be

$$p_b = (p_s - \Delta p_{BL})/\beta,$$

where $\Delta p_{BL} = 150$hPa is a nominal boundary-layer thickness. At most latitudes, p_b is somewhat greater than 700 hPa, except in the Antarctic, where hatching is used to indicate regions that are beneath the pressure level p_b. Despite this accommodation of a 150 hPa boundary layer, the vertical-shift transformation disagrees strongly with the simulated changes in levels just above 700 hPa. This could be an indication that boundary layer fluxes are significant at levels higher than 150 hPa above the surface, or it could, for example, be an effect of parameterized convection.

5.5.2 Winds

Changes in the meridional mass streamfunction are less-well captured than changes in thermodynamic and moisture variables (Fig. 5-10d). While the pattern of increases and decreases is largely correct in the Northern Hemisphere and near the tropopause of both hemispheres, the Southern Hemisphere troposphere is dominated by meridional shifts and the magnitude of the changes in the transformed solution are too strong by at least a factor of two in both hemispheres. Qualitatively, the weakening in tropical overturning in the model simulations is captured by the transformation, but the maximum absolute value of the meridional mass streamfunction averaged between hemispheres decreases by $\sim 5\%$ K^{-1} according to the transformation, while the model simulations have decreases in the range 0.5-1.5% K^{-1}. In the mid-latitudes the changes in the overall strength of the Eulerian-mean overturning are not captured by the transformation, with the streamfunction maximum poleward of 30 degrees latitude decreasing by $\sim 4\%$ K^{-1} according to the transformation, but not changing or increasing slightly in the simulations.

The zonal-mean pressure velocity (whose changes may be inferred from Fig. 5-10d) represents only a small residual of larger pressure velocities in ascent and descent regions distributed around the globe, as demonstrated in Fig. 5-11a. Previous

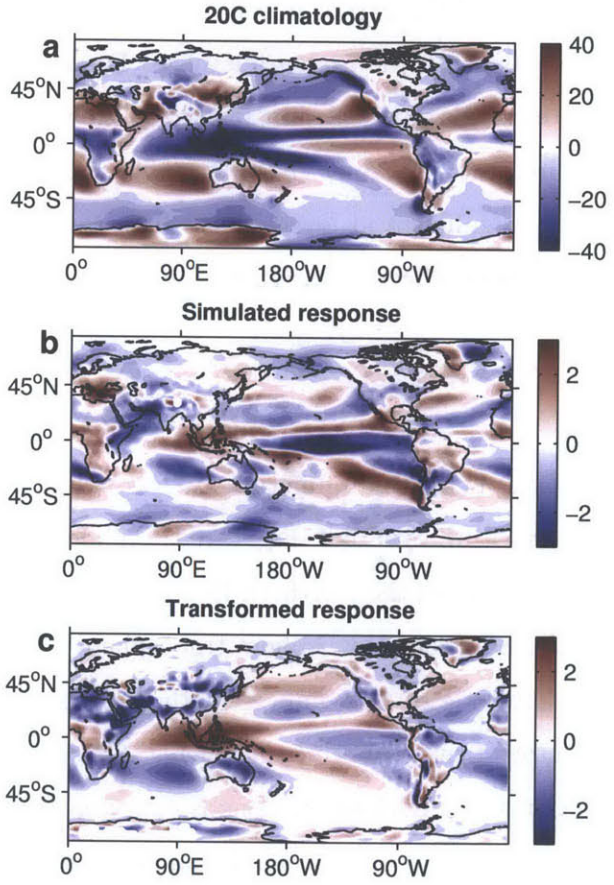

Figure 5-11: Global map of the CMIP3 ensemble- and time-mean pressure velocity (hPa day^{-1}) at 500 hPa: (a) 20th century climatology (1981-200), (b) response under the SRESA1b scenario and (c) response calculated using the vertical-shift transformation and the 20th century climatology. For (b) and (c) individual model changes are normalized by the global-mean change in surface air temperature before being combined into the ensemble mean.

studies have found that the zonally-symmetric circulation weakens by less than the zonally-asymmetric circulation (e.g., Vecchi and Soden, 2007), a difference that is not captured by the vertical-shift transformation. To examine the zonally asymmetric response, we apply the vertical-shift transformation to the pressure velocity at 500 hPa at each latitude and longitude. Both the simulated response and the response given by the vertical-shift transformation tend to be of opposite sign to the climatological value (Fig. 5-11b,c), implying a reduction in overturning in most places. The largest changes are in the equatorial Pacific, where both the simulated response and the transformation show less ascent over the maritime continent and more in the central and eastern Pacific. Similarly, the sign of the simulated response over the Pacific, Indian Ocean, and Africa is correctly captured by the transformation. There are some quantitative differences between the transformation and simulated changes. For instance, the simulated response shows stronger increases in ascent in the eastern tropical Pacific than decreases in the west [related to the tendency for coupled climate models to simulate a more "El Niño-like" state in a warmer climate (e.g., Vecchi and Soden, 2007)], whereas the transformation gives the opposite. Thus, the response of the transformation for the pressure velocity is not quantitatively accurate, but the agreement is better than might be inferred from consideration of the changes in meridional mass streamfunction alone.

There are considerable differences in the simulated response of the mean zonal wind and the response given by the vertical-shift transformation (Fig. 5-12a). The transformation shows a pronounced decrease in the troposphere with an increase near the tropopause, while the simulated changes show a larger increase near the tropopause and little change in most of the troposphere. The vertical-shift transformation appears to better reproduce the pattern of simulated changes in the mean and variance of the meridional wind than those of the zonal wind, although the magnitudes of the changes are not captured. Both the simulated response and transformation show increases in wind variance near the tropopause at mid-latitudes, and decreases below. But the decreases in wind variance in the troposphere are too large in the vertical-shift transformation, and the simulated response also exhibits a poleward

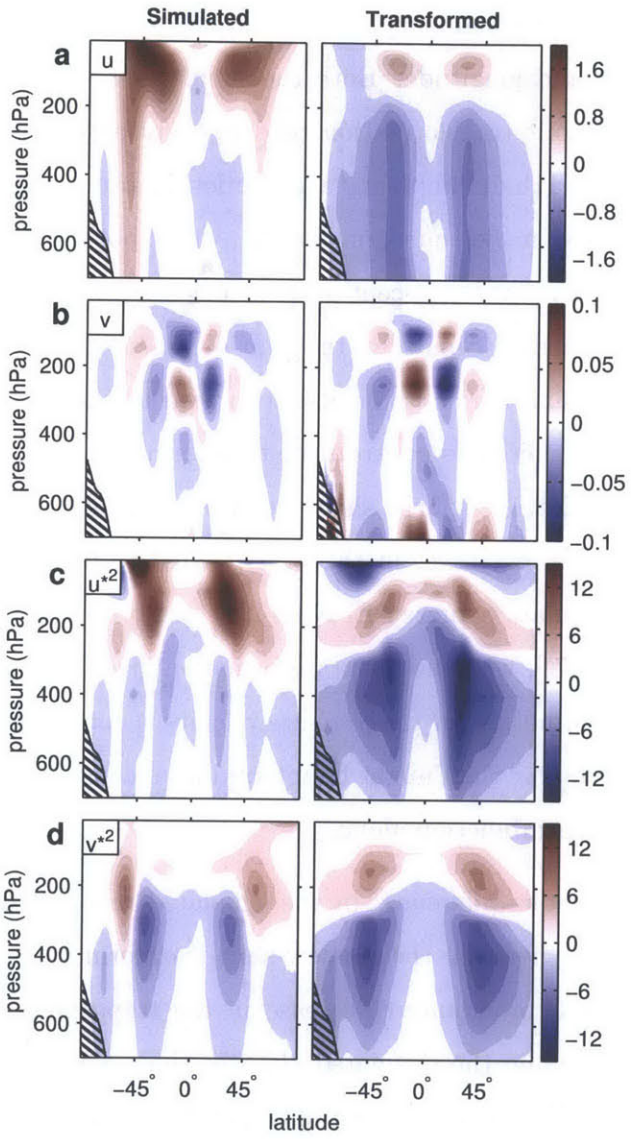

Figure 5-12: As in Fig. 5-10 but for normalized changes in (a) mean zonal wind (m/s), (b) mean meridional wind (m s^{-1}), (c) zonal wind variance ($m^2 s^{-2}$) and (d) meridional wind variance (m^2 s^{-2}). Wind variances are calculated based on daily data with respect to the annual mean before being zonally averaged.

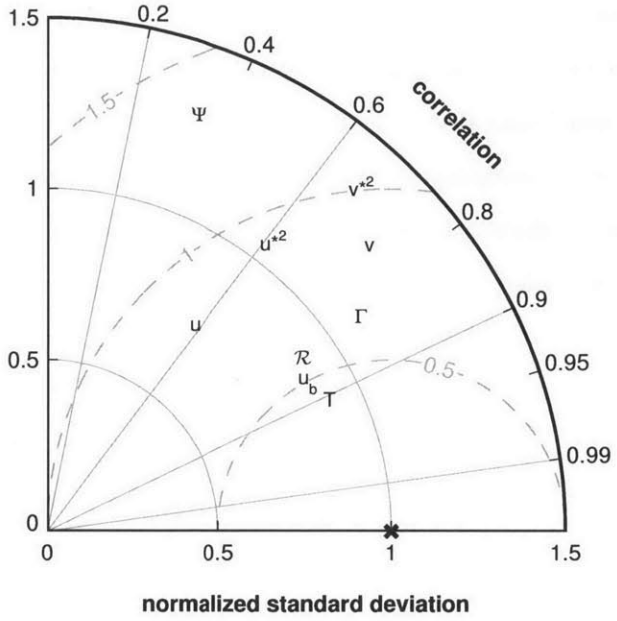

Figure 5-13: As in Fig. 5-9, but for the ensemble mean of the CMIP3 simulations.

shift (especially for the meridional wind variance).

5.5.3 Summary and poleward shift

The extent to which the transformation captures the simulated changes in the CMIP3 ensemble is summarized by the Taylor diagram shown in Fig. 5-13. Correlation coefficients are above 0.8 and normalized errors are below roughly 0.6 for temperature, lapse-rate, and relative humidity. The dynamical variables, on the other hand, have lower correlation coefficients and normalized errors close to unity. The normalized error is considerably greater than unity for the meridional mass streamfunction, indicating that by this measure the transformation is less accurate than simply assuming no change.

The pattern of mismatch in the response of the mean zonal wind (Fig. 5-12) suggests that the difference between the simulated and transformed responses in the mean zonal wind is largely in the barotropic component, and thus related to the inability of the transformation to satisfy the surface boundary conditions for momen-

tum (the transformation implies a general weakening of surface winds), together with a poleward shift of the jets that the vertical-shift transformation does not capture[9]. Note that the poleward shift does not account for all of the barotropic component of the error, and there is considerable weakening of the mid-latitude jets in the transformation that is not reflected in the model simulations. When a latitude-dependent barotropic offset is included in the transformation of the zonal wind (see section 5.4), the level of agreement improves considerably, as shown by the symbol u_b in Fig. 5-13.

In general, the vertical-shift transformation is less accurate in reproducing the response to warming in the CMIP3 simulations compared with the idealized GCM simulations, especially for the winds. This is not surprising given that the assumption of a simple upward shift in the radiative tendencies with warming is less accurate, given that the more complicated forcing implies a more complex response, and given that a poleward shift of the circulation occurs to a greater extent. Despite these caveats, the transformation still captures a number of the major features of the simulated climate changes in the middle and upper troposphere in both the tropics and mid-latitudes of the CMIP3 simulations.

5.6 Conclusions

We have examined the extent to which changes in temperature, humidity, and circulation that occur under global warming may be understood in terms of a vertical shift. Using the inviscid moist primitive equations on the sphere, a one-parameter transformation was derived that allows for a warming atmosphere and which shifts the circulation upwards in a manner consistent with the governing equations. While all variables are shifted upwards by the transformation, the pressure velocity also decreases in magnitude and the change in temperature includes an additional offset. Because of the effects of latent heat release, the transformation is only accurate to the extent that fractional variations in $T\theta$ are small. For Earth-like climates

[9]A complication regarding the poleward shift is the inconsistent treatment of ozone recovery between models (Son et al., 2008). However, we find similar results when only models with no changes in ozone over the 21st century are considered.

this condition is approximately satisfied in the troposphere, especially in the tropical lower-troposphere, where latent heating is most important.

The transformation was shown to be accurate in reproducing moist-adiabatic parcel ascents as the surface temperature was varied. This constitutes a simple but non-trivial demonstration that the transformation is able to reproduce changes to the mean temperature structure of an idealized convecting atmosphere. The transformation was evaluated in a more general framework using simulations with both an idealized GCM and an ensemble of comprehensive GCMs. The radiative-cooling parameterization in the idealized GCM was constructed so as to conform to the transformation, and the transformation was found to perform well in reproducing changes in the mean thermodynamic and moisture distributions and in the meridional wind and wind variances. For the comprehensive GCM simulations, the similarity between the simulated and transformed responses was less pronounced than in the idealized GCM simulations (possibly related to the radiative cooling not simply shifting upwards and a greater poleward shift of the winds in the midlatitudes), but some of the important features of the thermodynamic and dynamic responses were still captured.

According to the transformation, the pressure velocity decreases in magnitude as it shifts upwards, implying a decrease in the strength of the mass overturning of the atmosphere in proportion to the transformation parameter β. For typical values of β found in the tropics of the idealized and comprehensive GCM simulations, this corresponds to a decrease in overturning of 4-6% K^{-1} relative to the change in global mean surface air temperature. Further work would be needed to establish the relevance of the rate of change in overturning given by the transformation. One important limitation is that the transformation does not account for the radiative effects of well-mixed greenhouse gases or absorbing aerosols which could also affect global-mean precipitation and overturning (e.g., O'Gorman et al., 2011).

Mismatches between the transformation and the simulated response to climate change were primarily either in or near the boundary layer (as in the case of the relative humidity) or dynamically related to an inability to satisfy the correct surface boundary conditions (as in the case of the zonal wind). In light of this, it may

be useful to decompose the response of the general circulation into the sum of two parts: the upward shift outlined here and a correction to account for mismatches in surface boundary conditions. We speculate that it may be possible to investigate and reproduce the correction by simulating the climate response to a change in boundary conditions from the usual boundary conditions to boundary conditions that the transformed solution would satisfy. The correction might only be large close to the surface for some variables (e.g., relative humidity), but could be expected to have a barotropic component in the case of the zonal wind.

Because the transformation of temperature is not purely an upward shift [due to the $\Delta\theta$ term in (5.13e)], the transformation implies that both the cold-point temperature and the divergence-weighted temperature in the tropical upper troposphere should decrease with surface warming. The latter quantity has recently been investigated by Zelinka and Hartmann (2010), who found that in the CMIP3 models the tropical-mean divergence-weighted temperature increases as the climate warms, although much less so than the surface temperature. This discrepancy may indicate that the assumption of a simple upward shift of the radiative cooling is not sufficient to capture such relatively subtle changes in this region of the tropical atmosphere. Nevertheless, the vertical-shift transformation accurately reproduces much of the simulated changes in the lapse-rate of the tropical troposphere as the climate warms. A simple upward shift was also found to reproduce much of the change in mean cloud fraction in a simulation of greenhouse-gas driven warming (cf. Fig. 5-1), and it would be worthwhile to try to extend the vertical-shift transformation to include such cloud properties.

The transformation introduced here provides a simple framework in which to analyze the upward shift of the general circulation under global warming. It offers the advantage that it is based on the governing equations, and it suggests that the upward shift is a coherent response of the circulation as a whole, rather than something that occurs in one or two variables in a particular region. The extent to which the transformation (with a single tunable parameter) captures the global response of the circulation under a given radiative forcing may be expected to depend on the

complexity of the forcing and the extent to which the circulation shifts meridionally. Given that different climate models generate different control climatologies, the transformation may be helpful for understanding the source of intermodel scatter in the simulated response to climate change (cf., Sherwood et al., 2010). Indeed, the transformation has recently been found to reproduce the ratio of temperature trends in the middle and upper troposphere in a number of GCM simulations of global warming based on the climatological temperature distribution given by each model (O'Gorman and Singh, 2013).

5.7 Appendix: alternative calculation of the transformation: meridionally varying β

The derivation in section 5.2 assumes that the transformation parameter β is constant in both space and time. Consistently, we have used a single global value of β when applying the transformation to simulations of climate change. However, β could be allowed to vary with latitude such that the transformed solution still remains an approximate solution to the governing equations if the variations in β are small enough. Figure 5-14 shows an application of the transformation to the idealized GCM simulations in which β is allowed to vary in latitude. The value of β is calculated by minimizing the error function (5.16) at each latitude independently, and a corresponding value of $\Delta\theta$ was then determined at each latitude using (5.11). The extent to which the simulated response is captured by the transformation is improved considerably in the case of temperature (compare Fig. 5-14 and Fig. 5-7a), especially in the subtropics, but less so for other variables (not shown).

To quantify the extent to which β should be allowed to vary in latitude, consider the example of the transformation of the meridional gradient of the zonal wind,

$$\frac{\partial u'}{\partial \phi} = \left.\frac{\partial u}{\partial \phi}\right|_{\beta p} + \frac{\partial \beta}{\partial \phi} p \left.\frac{\partial u}{\partial p}\right|_{\beta p}, \tag{5.19}$$

where u' is the transformed solution. The difference in this quantity between the

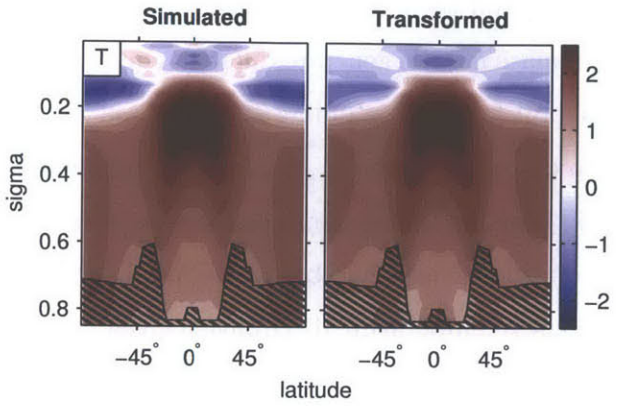

Figure 5-14: As in figure 5-7a but with the transformation parameter β allowed to vary in latitude. The values of β vary between 1.08 and 1.12 depending on latitude and were calculated by minimizing the error function (5.16) at each latitude independently.

control and vertically-shifted solution is approximately given by

$$\frac{\partial\left(u'-u\right)}{\partial\phi} = p\left[\left(\beta-1\right)\left.\frac{\partial^2 u}{\partial\phi\partial p}\right|_p + \left.\frac{\partial\beta}{\partial\phi}\,\frac{\partial u}{\partial p}\right|_{\beta p}\right]. \tag{5.20}$$

For the change between the control and vertically-shifted solution to be accurate, the second term on the right-hand side of the above equation must be small compared with the first term on the right-hand side. If meridional variations in $\partial_p u$ and β occur on similar length scales, then this condition reduces to requiring that the meridional variation $\Delta\beta$ satisfies

$$\frac{\Delta\beta}{\beta-1} << 1. \tag{5.21}$$

For the application of the transformation in Fig. 5-14, $\beta - 1/\delta T \approx 0.05$, varying between a maximum of 0.058 in the tropics and 0.038 in the midlatitudes. This yields $\Delta\beta/(\beta-1) \approx 0.4$, implying that allowing β to vary may introduce substantial errors. However, there are some regions of the atmosphere, such as the tropics, where β is indeed relatively constant, and the solution will be valid locally in these regions. Allowing β to vary for the CMIP3 models also leads to a greater similarity between the transformed and simulated temperature responses, however the condition (5.21) is still not very well satisfied with $\Delta\beta/(\beta-1) \approx 0.5$.

Chapter 6

Conclusion

6.1 Summary

In this thesis we conducted an idealized study into the effect of changing surface temperature on atmospheric circulations, employing a variety of theoretical and numerical tools. Chapters 2 – 4 focused on the atmosphere in a state of radiative-convective equilibrium (RCE) in order to investigate the behavior of moist convection at a wide range of surface temperatures. We explicitly simulated convective clouds using a cloud-system resolving model (CRM), and we employed a number of conceptual models to understand the behavior of the simulations and interpret the results in physical terms. We found large increases in the convective available potential energy (CAPE), cloud buoyancy, and updraft velocity in the simulations as the surface temperature increased. However, the magnitude of the simulated cloud buoyancy was found to be much smaller than that of the undilute buoyancy used to define CAPE, suggesting entrainment and mixing play important roles in determining the properties of moist convection in the simulations.

In chapter 2 we introduced a conceptual model, termed the "zero-buoyancy plume model" (ZBPM), to account for the simulated increase in CAPE with warming. The model is based on the representation of an ensemble of convective clouds as a bulk entraining plume, and the assumption that the plume is neutrally buoyant with respect to the environment. The ZBPM reproduces the large increase in CAPE with warming

seen in the simulations; as the atmosphere warms at constant relative humidity, the saturation deficit of the troposphere increases, and a given amount of entrainment becomes more effective in altering the plume temperature, and thus the environmental lapse rate, away from that of a moist adiabat. We also presented observational evidence of a relationship between the lower-tropospheric lapse rate and the environmental humidity in convecting regions of the atmosphere. This evidence supports a role for entrainment in determining the thermal stratification in these regions.

In chapter 3 we considered the mechanisms leading to the large increase in updraft velocity with warming in the RCE simulations. A tight coupling between the peak updraft velocity and the vertical integral of the cloud buoyancy was found, suggesting this buoyancy integral is a key determinant of convective vigor in the simulations. Using a plume model in which the plume environment was taken as the mean profile of the simulations, it was shown that the magnitude of the simulated increase in updraft velocity with warming could be explained while assuming a fixed representation of cloud entrainment and microphysics in the plumes. While this result is sensitive to the uncertain representation of cloud entrainment in the simulations, it nevertheless provides some support to the notion that knowledge of the behavior of cloud updrafts under climate change may be gleaned from large-scale fields (e.g., as provided by GCM output), although such estimates may not be quantitatively accurate (c.f. Del Genio et al., 2007).

The environmental lapse-rate was included in the plume calculation through a generalization of the ZBPM introduced in chapter 2. A two-plume model model was derived, in which one plume represents the most intense updrafts, and the other plume has negligible buoyancy. Under the assumption that the tropospheric relative humidity and the entrainment rates of the plumes are invariant as the surface temperature increases, the two-plume model predicts a rapid increase in the buoyancy integral of the most intense updrafts and even larger fractional increases in the buoyancy integral of an undilute plume. This is consistent with the behavior of the simulations in which the fractional increase in the undilute buoyancy integral with warming is larger than that of the buoyancy integral of the simulated clouds. The

two-plume model results suggest that the differing scaling of CAPE and buoyancy integral with temperature in the simulations may be in part explained by the effect of entrainment on the most intense updrafts. However, the profile of cloud buoyancy in the simulations is not reproduced in detail by the two-plume model, and further work is needed to understand all the mechanisms that determine the scaling of cloud buoyancy with temperature.

We examined the precipitation rates in RCE in chapter 4. Confirming previous results, we found that, at surface temperatures characteristic of Earth's tropics and higher, precipitation extremes (defined by high percentiles of the precipitation distribution) increase with warming in proportion to the near-surface humidity, following what is known as Clausius-Clapeyron (CC) scaling. But at lower temperatures and for short accumulation periods, the scaling of precipitation extremes with warming in the simulations is significantly higher than the CC rate. We argued that this super-CC scaling is a result of the increase in hydrometeor fall speeds accompanying warming. As the atmosphere warms, the column hydrometeor distribution switches from being dominated by snow to being dominated by rain. Since snow falls at typical speeds of $0.5 - 1$ m s^{-1}, while rain often falls at speeds in the range $5 - 8$ m s^{-1}, this increases the mean hydrometeor fall speed. Low hydrometeor fall speeds result in weaker precipitation extremes because the hydrometeors have more time to evaporate and turbulently spread out over a larger area as they fall. Additionally, for short accumulation periods, a lower fall speed may spread the precipitation out in time to a greater degree, also decreasing the intensity of precipitation extremes. The results suggest that precipitation extremes in RCE are not necessarily constrained to scale with surface moisture, and the rough CC scaling found at higher temperatures may be partly coincidental.

Finally, in chapter 5 we focused on the vertical structure of the large-scale circulation, and how it may change with warming. A novel transformation of the governing equations was derived which gives a one-parameter family of transformed solutions for any given solution of the equations of motion. The transformation involves a vertical shift of the circulation as well as an additional offset to the temperature

field and a weakening of the pressure (vertical) velocity. We applied the transformation to simulations of increasing surface temperature with a hierarchy of models, including both idealized and comprehensive general circulation models (GCMs), to determine its applicability to the change in the atmospheric circulation as a result of climate warming. For small climate perturbations, the transformation reproduced many aspects of the circulation change as predicted by GCMs, particularly for the thermodynamic variables. The weakness of the transformation lies in its inability to satisfy the correct boundary condition in the altered climate, reducing its fidelity near the surface, and reducing its fidelity for the zonal-mean wind, for which the integrated momentum budget is important. Nevertheless, the transformation is useful in providing a framework for understanding the tendency of many variables at different latitudes to experience an upward shift under climate warming.

6.2 Implications

The work presented in this thesis has a number of potential implications for the behavior of the atmosphere and its response to global warming.

6.2.1 Increase in updrafts and CAPE with warming: dependence on cumulus entrainment

In chapter 2 we found that the increase in CAPE with warming seen in simulations of RCE could be related to the effect of cloud entrainment on the mean tropospheric lapse rate. Furthermore, we argued in chapter 3 that this CAPE increase was associated with substantial increases in the upper tropospheric updraft velocity in the simulations. If such convective updraft increases were to occur in Earth's atmosphere under global warming, this could have implications for troposphere-stratosphere exchange. For instance, a change to the upper-tropospheric convective updraft velocity could alter the transport of trace constituents into the stratosphere (Chaboureau et al., 2007), or it could change the thermodynamic structure of the

tropical tropopause layer (Kuang and Bretherton, 2004).

It is thus important to understand the degree to which the mechanisms resulting in the increase in updraft velocity in the simulations may apply to Earth's atmosphere. In particular, the results of chapter 2 and 3 are dependent on the characteristics of mixing between the simulated clouds and their environment, but these mixing processes are not well resolved in the CRM, and the simulations may not accurately represent the mixing processes in cumulus clouds on Earth.

Given the importance of cumulus entrainment for the CRM results regarding CAPE and updraft velocity, it is helpful to briefly review some of the previous literature on the subject. Attempts to understand the mechanisms by which cumulus convection mixes with its environment have a long history in the atmospheric sciences. Early work suggested that much of the vertical heat transport in the equatorial region is achieved in undilute convective turrets which have since become known as "hot towers" (Riehl and Malkus, 1958). Xu and Emanuel (1989) found that radiosonde observations of the tropical atmosphere do not contradict the hypothesis that the tropospheric thermal structure is constrained to be neutrally buoyant with respect to a parcel lifted reversibly from the sub-cloud layer where convection is active. If such a hypothesis is true, it would indicate that undilute parcels from the boundary layer do penetrate to the upper troposphere, and that they play an important role in setting the thermal stratification of convective regions of the atmosphere. This is in contrast to the simulations shown in this thesis, in which the tropospheric lapse rate deviates considerably from moist-adiabatic at high surface temperature.

However, Zipser (2003) argues that, despite decades of field programs, unambiguous observations of undilute ascent significantly above the boundary layer have never been found. The author instead suggests that a combination of entrainment and the latent heating associated with the freezing of condensate in upward moving cloud parcels may account for the observed thermal structure of the tropical atmosphere. This conclusion is consistent with recent high resolution (100 m horizontal grid-spacing) simulations of RCE in which undilute ascent is almost completely absent in the upper troposphere, and the latent heat of freezing is important in allowing

cloud updrafts to reach the tropopause (Romps and Kuang, 2010a).

The primary mechanism by which environmental air is entrained into convective clouds has also been the subject of considerable debate. The conceptual model of convective entrainment used in this thesis is that of an entraining plume, first used to model cumulus clouds by Stommel (1947). In such a model, air enters the cloud laterally and is instantaneously incorporated into the updraft. However, an elegant analysis of aircraft measurements by Paluch (1979) suggested that this is not the main mechanism by which clouds mix with their environment. Paluch found that, when plotted in a phase space with liquid water potential temperature and total water content as the axes, in-cloud observations at a given level lie on a mixing line connecting environmental properties at the cloud base and environmental properties at a level several kilometers above the flight path. These results were confirmed by a number of later studies (see e.g., Reuter, 1986) and interpreted to be evidence that lateral entrainment into clouds is not the dominant mixing process, and instead, evaporatively driven downdrafts from the cloud top are the primary source of environmental air entrained into cumulus clouds.

More recent work, however, has cast doubt on the above interpretation of the Paluch mixing diagrams. Taylor and Baker (1991) presented a different conceptual model in which cloudy air parcels are diluted by a series of lateral mixing events with the environment, and these diluted parcels then move vertically towards their level of neutral buoyancy. This "buoyancy sorting" mechanism ensures that all mixtures on a Paluch diagram exist within two obtuse triangles which may resemble two-point mixing (see also Böing et al., 2014). It is therefore difficult to distinguish between cloud-top entrainment and lateral entrainment in combination with a buoyancy sorting mechanism using conserved-variable diagrams of in-cloud properties.

In the last few years, computational resources have grown such that entrainment mechanisms in cumulus clouds may be studied directly through large-eddy simulations (LES) of moist convection run at resolutions that resolve some of the inertial subrange of the turbulent kinetic energy spectrum (e.g., Siebesma et al., 2003; Romps and Kuang, 2010a). Such high resolution is a requirement for turbulent closures such

as those based on Smagorinsky (1963) to be well founded, and simulations at these resolutions may have some hope of representing the relevant mixing processes accurately. LES studies reveal significant horizontal mixing between cloudy and environmental air, both in shallow (Heus et al., 2008) and deep (Böing et al., 2014) convection, and very little evidence of significant mixing by penetrative downdrafts. In particular, Böing et al. (2014) explained the apparent mixing-line behavior of Paluch-diagrams based on LES of deep convection via an entraining parcel model which included a range of entrainment rates as well as a simple representation of precipitation. de Rooy et al. (2012) argues that this all but settles the debate as to the dominance of horizontal mixing as a mechanism for cloud dilution. However, it must be noted that this is based on results from large-eddy simulations (LES), which, while run at very high resolution, still require the smallest-scale mixing to be parameterized.

In chapter 2 of this thesis, observational evidence was presented that provides some support for a role for lateral entrainment in determining the lapse-rate in convecting regions of the tropics. The relationship between a measure of the lower-tropospheric lapse rate and a measure of the lower-tropospheric humidity found in radiosonde soundings was interpreted as a byproduct of the effect of lateral cloud entrainment on the critical lapse rate required for convective instability. Encouragingly, we found the observational estimate of the entrainment rate based on the zero-buoyancy plume model is consistent with a similar estimate derived from the simulations.

However, other interpretations of the observed lapse-rate-humidity relationship may be possible, and the representation of convection as a bulk entraining plume is a gross simplification of the actual mixing mechanisms within clouds. For instance, the appropriate entrainment profile that should be used in a bulk plume model is not well known, and may be tracer dependent (Romps, 2010). One may be able to partly address this deficiency by allowing for a spectrum of plumes, each with a different entrainment rate, as was done in section 3.4. Lin and Arakawa (1997a,b) argued that such a plume spectrum may be a reasonable model for a convective ensemble if the individual plumes in the spectrum are considered as convective elements, rather than clouds themselves.

Plume models of the form considered in this thesis, however, are not able to take into account a number of effects that potentially determine the rate of mixing between clouds and their environment, including precipitation driven downdrafts[1], episodic mixing events (Raymond and Blyth, 1986; Romps and Kuang, 2010b), the buoyancy sorting mechanism (Taylor and Baker, 1991; Raymond and Blyth, 1986; Kain and Fritsch, 1990), and inhomogeneities in the properties of entrained air (Romps, 2010). Heus and Jonker (2008), for instance, argue for the importance of a shell of downward moving air around convective clouds for the transport properties of shallow convection, and such descending shells could affect the properties of the air entrained into the convective updraft. The Plume models described in this thesis assume a single value for the environmental properties, and assume continuous entrainment as air ascends within the cloud.

The above discussion suggests that a plume representation of a convective ensemble is at best an incomplete description of all the relevant dynamics. While the plume model was found to be adequate for understanding many aspects of the CRM simulations, one must be cautious in extrapolating such results to Earth's atmosphere. Given these caveats, what can be said about the application of the CRM results to convection in a warmed climate?

We argue that the observational results of chapter 2 provide reasonable evidence for some role of lateral entrainment in determining the stratification of convecting regions of the atmosphere. Based on the zero-buoyancy plume model, this suggests that CAPE does indeed increase with global warming. Additionally, previous modeling studies of RCE have shown that CAPE increases with warming at a similar rate in simulations with both lower [Muller et al. (2011); 4 km horizontal grid spacing] and higher [Romps (2011); 200 m horizontal grid spacing] resolution to the simulations used in this thesis, while the undilute fraction of cloud updrafts actually slightly decreases as the grid spacing is decreased from 3.2 km to 100 meters (Romps and Kuang, 2010a). But even at relatively small grid spacings of the order of 100 meters,

[1]Some convection parameterizations constructed for large-scale models based on entraining plumes do have a representation of precipitation driven downdrafts (e.g., Tiedtke, 1989).

the mixing mechanisms in cumulus clouds are not fully resolved, and thus the exact rate at which CAPE may increase with warming is unknown. Additionally, changes in CAPE in Earth's atmosphere may also be influenced by changes in seasonal and horizontal temperature gradients which are not present in RCE.

The possible effects of changes in CAPE on the convective clouds themselves are even more uncertain, and further work is required to understand whether the updraft increases with warming found in the RCE simulations may apply to moist convection under future climate change.

6.2.2 Effects of hydrometeor fall speeds on updrafts and precipitation rates

The updraft velocity in the RCE simulations shown in this thesis is relatively insensitive to the fall speed of hydrometeors. This is in contrast to the recent study of Parodi and Emanuel (2009) documenting a strong influence of rain-drop fall speed on convective updrafts in similar idealized RCE simulations. Part of this disagreement may be a result of differences in the treatment of the ice phase; we recover some dependence of the updraft velocity on rain-drop fall speed if the CRM is altered to include only warm-rain microphysical processes, as was the case in Parodi and Emanuel (2009). We thus suggest that the influence of hydrometeor fall speed is weakened when more complex, ice-phase microphysics are considered. However, this does not imply that microphysics *cannot* play a role in determining updraft velocity in moist convection. In our simulations, the buoyancy of typical clouds is a relatively small residual between a term associated with the virtual temperature excess, and a term associated with condensate loading. Thus, microphysical effects other than hydrometeor fall speed that influence the condensate loading may have an effect on cloud buoyancy. A complete understanding of the factors influencing updraft velocity in moist convection remains a challenge for the field.

The precipitation rate in the RCE simulations, unlike the updraft velocity, is highly sensitive to the fall speed of hydrometeors. Our study of precipitation extremes

in RCE (chapter 4) demonstrates that this sensitivity can lead to a scaling of precipitation extremes with warming substantially higher than the "Clausius-Clapeyron" (CC) rate that relates precipitation to surface moisture. While precipitation extremes on Earth occur in regimes far from RCE, this mechanism is sufficiently general to be of potential relevance even in the case in which there is strong large-scale forcing. An increase in the mean fall speed of hydrometeors with warming is one factor that may contribute to super-CC scaling of precipitation extremes found in some station observations stratified by surface temperature (e.g., Lenderink and van Meijgaard, 2008). Since the increase in fall speed would be expected to occur under global warming, any attribution of the observed super-CC scaling to fall-speed changes may have implications for the response of precipitation extremes to long-term temperature trends associated with climate change. However, the dependence of precipitation extremes on fall speed invokes mechanisms that primarily spread the precipitation in space and time. Hydrometeor fall speed may thus have less of an effect on storm-total precipitation than precipitation rates at given locations. This would suggest that increases in precipitation rates with warming in high-resolution gauge observations could be different from the scaling of storm-total precipitation.

6.2.3 The thermal stratification of the troposphere

In chapter 5, we shifted focus to the large-scale circulation. The vertical-shift transformation (VST) provides a novel way to summarize the extent to which the circulation of the atmosphere shifts upward with warming. Recently, O'Gorman and Singh (2013) used the VST to attempt to understand the vertical structure of temperature change as a result of an increase in surface temperature. GCMs typically predict that the warming in the tropical upper troposphere will be amplified relative to lower levels in simulations of greenhouse-gas induced climate change. But the degree of this upper-tropospheric amplification varies greatly between models. O'Gorman and Singh (2013) were able to predict these different amplification factors in different GCMs based on an application of the VST to the mean climatology of each model. This suggests that differences in warming profiles between GCMs may be a result of

differences in their climatology, and the response of climate models to warming may be improved by improving their representations of the temperature structure in the current climate. Additionally, the authors found that radiosonde temperature trends in the middle and upper troposphere were consistent with the VST as applied to the observed climatology, although there are large uncertainties in the observed trend estimates.

The zero-buoyancy plume model (ZBPM), derived in chapter 2, also provides a prediction of lapse-rate changes as a result of surface warming. The ZBPM and VST predictions are approximately consistent with each other; application of the VST to a temperature profile derived from the ZBPM gives a similar result to recalculating the ZBPM-derived profile at a higher surface temperature. But the two models have somewhat different domains of validity; the VST may be applicable to the mean stratification over the entire globe, while the ZBPM is only potentially valid in regions of the tropical atmosphere that are actively convecting. Additionally, the ZBPM prediction of the upper-tropospheric amplification factor is relatively insensitive to the entrainment rate. This may be interpreted as evidence that variations in the entrainment formulations between GCMs do not account for the differences in upper-tropospheric amplification. Further research is needed to understand the physical mechanisms that lead to differences in tropical lapse rates in the climatology produced by different models. Nevertheless, these results demonstrate the utility of the VST in providing insight and suggesting directions for more targeted research in regards to the source of scatter among model responses to climate change, and the VST may potentially be useful in constraining observed upper tropospheric trend estimates based on temperature trends at lower levels, and the observed climatology.

6.3 Future work

In this section we briefly describe three possible future research directions motivated by the results presented in this thesis.

6.3.1 Entrainment in GCMs

The observational relationship between lower-tropospheric lapse rate and humidity shown in chapter 2 was used to argue for an effect of entrainment on the thermal stratification in actively convecting regions of the atmosphere. An interesting question one may ask is: to what degree is this relationship reproduced in GCMs?

Figure 6-1 shows radiosonde observations as well as GCM output plotted in a similar way to Fig. 2-3 of chapter 2. We consider as a measure of the lower-tropospheric lapse rate the difference between the saturation moist static energy between the middle and lower troposphere, ΔMSE. As in Fig. 2-3 the lower-tropospheric humidity is measured by the saturation deficit in energy units, $L_{v0}(q_v^* - q_v)$. Here, q_v is the specific humidity, with the asterisk referring to saturation, and L_{v0} is the latent heat of vaporization evaluated at the reference temperature $T_0 = 273.15$ K.

Fig. 6-1a shows data from individual soundings taken from the Integrated Global Radiosonde Archive (IGRA) at the locations shown in Fig. 6-2. As in chapter 2 there appears to be a limit to the degree to which soundings may be unstable, as measured by high values of ΔMSE, and the value of ΔMSE associated with this limit depends on the lower-tropospheric saturation deficit. The apparent stability limit does not appear to be as sharp as was the case in Fig. 2-3, but the basic behavior is consistent with the higher-vertical-resolution soundings from the tropical western Pacific considered in chapter 2.

Panels (b)-(i) of Fig. 6-1 show similar plots to panel (a), but using grid-point columns in a number of different GCMs participating in the 5th phase of the Coupled Model Intercomparison Project (CMIP5). Some of these models [e.g., (g) MIROC5] show an apparent stability limit similar to that in observations; the maximum value of ΔMSE obtainable by grid-point columns depends on the value of the lower-tropospheric saturation deficit in those columns. Other models show very different behavior; the highest values of ΔMSE in the model denoted (e) FGOALS appear to be insensitive to the saturation deficit.

A possible direction for future work is to probe the reasons that different models

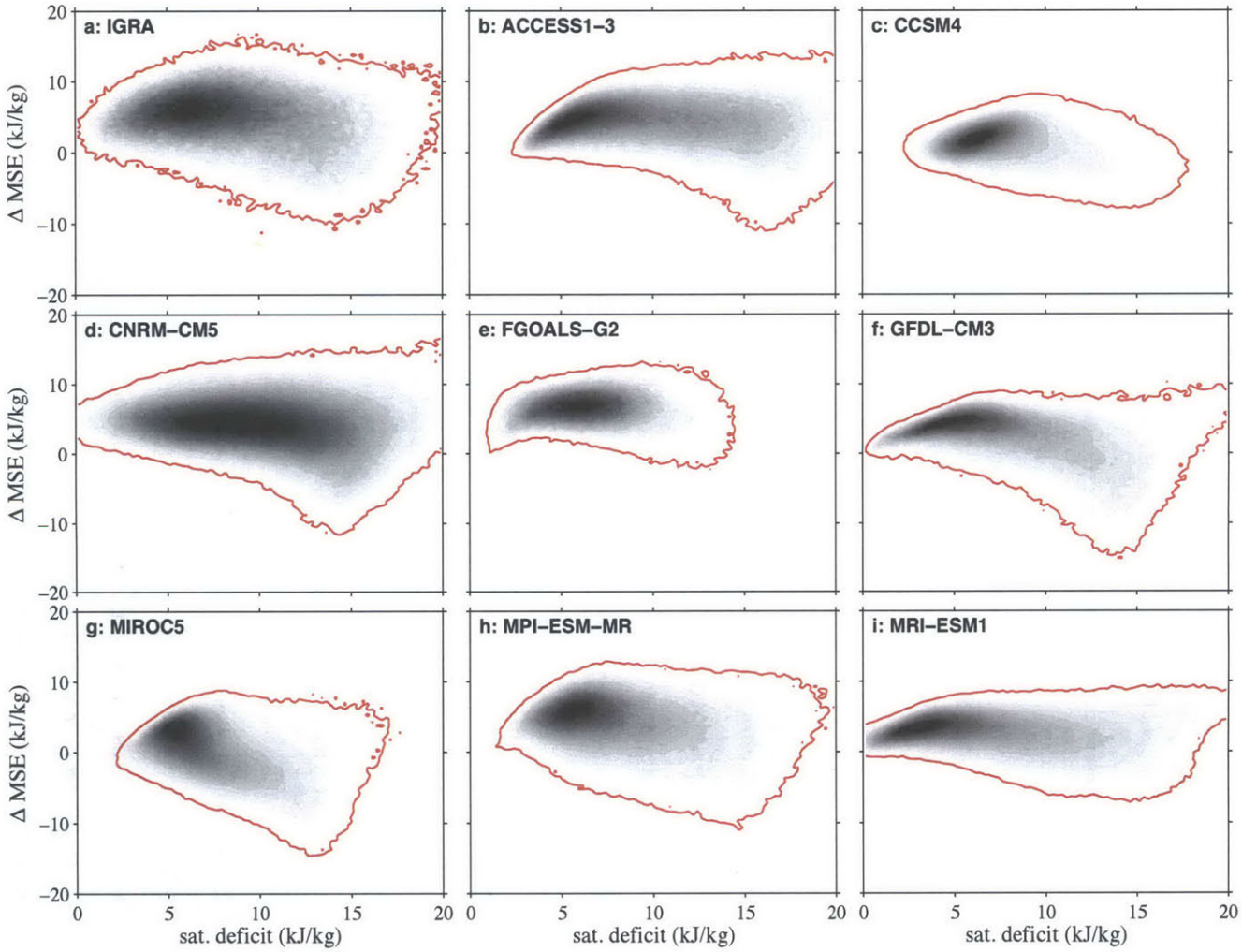

Figure 6-1: Two-dimensional histograms of profiles derived from (a) the IGRA dataset, and (b-i) a number of CMIP5 models. The profiles are binned by the pressure-weighted mean of the saturation deficit for levels between 850 and 500 hPa (x-axis) and the difference between the saturation moist static energy at 500 hPa and at 850 hPa, ΔMSE (y-axis). The saturation deficit is multiplied by the latent heat of vaporization to convert it to energy units (see text). In the case of IGRA, the profiles are taken from all the available radiosonde soundings from stations shown in Fig. 6-2 (a total of 670 thousand profiles). In the case of the CMIP5 models the profiles are daily grid-point columns over ocean points between 15°S and 15°N, for the year 1990 in the 20th century climate simulation. The histograms are normalized by their maximum value, and the red line is the contour level at 1/20th of this maximum value.

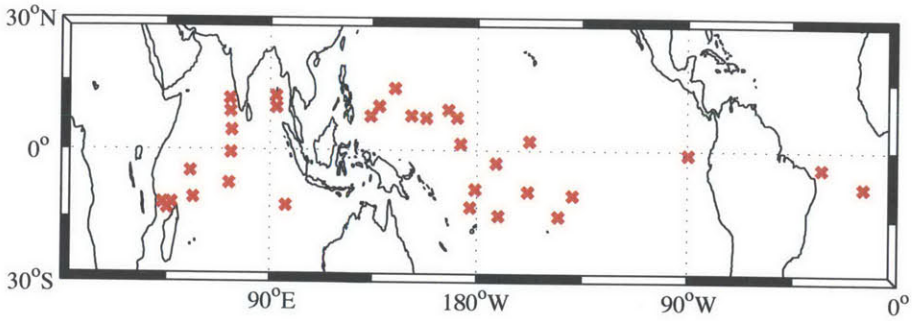

Figure 6-2: Locations of the 34 IGRA stations used to produce Fig. 6-1a. All stations are between 15°S and 15°N and were selected to be representative of maritime regions (i.e., stations that are away from continental influence were selected).

reproduce the observed stability limit to different degrees. One might hypothesize that the different behavior in regards to the stability limit may be a result of differences in the formulation of entrainment within the convective parameterizations of such models. In this case, the observed stability limit could be used to constrain the entrainment formulation in model convection parameterizations, providing a complementary method to those suggested by Sahany et al. (2012) for the same purpose.

6.3.2 Beyond radiative-convective equilibrium

In this thesis we studied the behavior of moist-convection in a domain of roughly 100 km across in RCE. RCE represents a state of the atmosphere in which there is no large-scale forcing; the mean vertical velocity in the domain is constrained to be zero. But in similar sized regions of Earth's atmosphere there may be significant vertical motion associated with large-scale circulations. In particular, strong convective events associated with precipitation extremes generally occur in regions of the atmosphere with strong large-scale ascent. This raises some question as to the applicability of the results discussed in this thesis to precipitation extremes and strong convective events on Earth. It is thus desirable to investigate the behavior of moist convection under the influence of large-scale forcing in order to demonstrate that the ideas outlined in this thesis apply to the more general case.

One method by which to include large-scale forcing in limited-domain models

such as CRMs is to use what is known as the weak-temperature gradient (WTG) approximation (e.g., Sobel and Bretherton, 2000; Raymond and Zeng, 2005). Under this approximation, the atmospheric temperature profile above the boundary layer is taken as given, and a domain-mean vertical velocity (the WTG vertical velocity) is included in the simulation to provide the required adiabatic cooling or warming to satisfy thermodynamic balance.

A potential extension of the work outlined in this thesis is to use the WTG approximation to conduct simulations of moist-convection including a representation of large-scale forcing. The behavior of convection at a range of temperatures with fixed large-scale forcing could then be investigated. A difficulty of such an approach, however, is in the specification of a 'fixed' large-scale forcing. For instance, a common way to describe the strength of the large-scale forcing in WTG models is the "relative sea-surface temperature" (SST). This is the difference between the SST specified in the simulation, and the SST that would lead to the RCE solution with the same tropospheric temperature (i.e., the solution with no large-scale vertical motion). But it is unclear if maintaining a constant relative SST with warming represents a 'fixed' large-scale forcing, or whether it would be more appropriate to maintain, for instance, a constant relative surface moist static energy.

A conceptually simpler method for including large-scale forcing in a study of moist convection is to simulate the entire Earth at a resolution high enough to explicitly resolve convective clouds. This is prohibitively expensive with current computational resources. But, by reducing the Earth's radius by some factor while simultaneously increasing the rotation rate by the same factor, the problem may be reduced to a more tractable one. For instance, reducing the Earth's radius by a factor of 6 would reduce the computational expense of a simulation with a given resolution by a factor of 36. An increase in the rotation rate would then be required to ensure that dimensional scales, such as the Rossby radius, remained fixed relative to the size of the planet. This is a similar approach to the "hypohydrostatic" rescaling recently discussed under various names by a number of authors (Kuang et al., 2005; Pauluis et al., 2006; Garner et al., 2007). Like the hypohydrostatic rescaling, the benefit of the "small-

Earth" approach is a reduction in the scale separation of convective clouds and the large-scale circulation, and thus a reduction in the computational resources required to resolve both scales. But the hypohydrostatic rescaling also includes a reduction of the diabatic timescales to maintain the relationship between these timescales and the rotation period. In the approach suggested here, the physical parameterizations of the model would remain unchanged, and the problem would instead be framed as investigating moist convection on a small, rapidly-rotating Earth-like planet.

6.3.3 Climate change and the entropy budget

Finally, a potentially interesting avenue of future work involves examining changes to the entropy budget of the atmosphere as the surface warms. As mentioned in the introduction, the entropy budget has been suggested as a possible constraint on the behavior of updrafts in moist convection by a number of authors (Emanuel and Bister, 1996; Rennó and Ingersoll, 1996). Subsequent work has pointed out that irreversible sources of entropy owing to mixing of dry and moist air and friction of falling hydrometeors must be accounted for if such closures are to be successful (Pauluis et al., 2000; Pauluis and Held, 2002a). Romps (2008) examined the entropy budget of an atmosphere in RCE in more detail and found that the frictional dissipation associated with the winds (anemonal dissipation) appeared to account for a roughly constant fraction of the radiative cooling of the atmosphere in simulations with different sub-grid diffusion schemes and with different surface temperatures. The author argued that this allowed for the possibility of constraints such as those advocated by Emanuel and Bister (1996) to apply, despite the fact that the anemonal dissipation was not the dominant irreversible entropy source. The RCE simulations described in chapters 2 – 4 provide an opportunity to test such hypotheses over a wide range of surface temperatures, and a possible direction for future work is to examine the entropy budget in these simulations.

Appendix A

Alterations to the cloud-system resolving model

Chapters 2 – 4 employ simulations of radiative-convecitve equilibrium (RCE) in a cloud-system resolving model (CRM) to examine various aspects of the behavior of moist convection. The model is similar to version 16 of Cloud Model 1 (CM1) outlined in Bryan and Fritsch (2002) and Bryan and Rotunno (2009), and available online at `www.mmm.ucar.edu/people/bryan/cm1/`, with minor alterations which we describe here.

We conduct series of simulations of RCE with a range of imposed CO_2 concentrations between 1 and 640 ppmv[1]. The CRM results shown in this thesis are primarily based on intermediate-resolution simulations, with a horizontal grid-spacing of 1 km and a domain size of 84 × 84 km (ch. 2 & 4), as well as high-resolution simulations, with a horizontal grid-spacing of 0.5 km and a domain size of 160 × 160 km (ch. 3 & 4). In these simulations, the sea-surface temperature (SST) at the lower boundary is fixed. However, the fixed-SST boundary condition is derived from corresponding low-resolution simulations (horizontal grid spacing 2 km, domain size 80 × 80 km) run to equilibrium over a slab ocean. As pointed out by Cronin and Emanuel (2013) the time-scale to equilibrium of an atmosphere in RCE is much longer when the lower

[1]Chapter 2 also included a simulation with a CO_2 concentration of 1280 ppmv, but this simulation was affected by a form of weak convective aggregation, and is not considered here.

boundary temperature is interactive, and can be up to a few hundred days. The required length of the slab-ocean simulations implies that accurate mass conservation in the model is critical, as any drift in mass will eventually affect the mean surface pressure. Similarly, to ensure the net top-of-atmosphere radiative flux is close to zero at equilibrium, accurate energy conservation is required.

In this appendix we outline alterations to version 16 of CM1 to improve mass conservation and reduce the drift in surface pressure with time (section A.1) as well as to improve global energy conservation (section A.2) and conservation of water substance (section A.3). Finally, we describe the degree to which the slab-ocean simulations described above conserve mass and energy (section A.4). In the following sections we will refer to the publicly available version 16 of CM1 as CM1v16, and we will refer to the version of the model used for the work presented in this thesis as the 'altered model'. Many of the changes outlined here are included in version 17 of CM1, and we thank George Bryan for incorporating our suggestions in the development of the model.

A.1 Mass conservation

Dry mass is not exactly conserved in CM1v16. This can have the effect of changing the surface pressure appreciably during long simulations of RCE. Mass conservation is improved in the altered model by including an extra calculation of the equation of state at each time step (section A.1.1). This reduces the drift in total dry mass with time considerably, but in order to reduce the mass drift to exactly zero, an explicit density adjustment is also included in the altered model (section A.1.2).

A.1.1 Ensuring dry-air density is unchanged by microphysical calculations

In CM1v16, the dry-air density is calculated using the equation of state immediately before the evaluation of the microphysical tendencies in each time step. The pressure

and potential temperature tendencies as a result of evaporation and condensation are then calculated, and new values of the pressure and potential temperature are found. In principle, the microphysical calculations should not change the dry-air distribution of the atmosphere, but in practice, small changes do occur owing to truncation error. To remove this spurious numerical mass source, we include in the altered model a recalculation of the pressure field after the microphysical calculations are performed using the pre-microphysics dry-air density.

We test the effect of the recalculation of pressure on global mass conservation using simulations of RCE with a fixed-SST boundary condition of 301.5 K over a time period of 50 days (Fig. A-1). We conduct simulations using the altered model in a similar configuration to the slab-ocean simulations described previously (2 km horizontal grid spacing, 80×80 km domain size, 64 vertical levels). The control simulation (black) includes all changes outlined in this document except the density rescaling outlined in section A.1.2. We compare the control simulation to similar simulations without the pressure recalculation (red) and with a doubled time step (blue). The pressure recalculation is very successful in improving global mass conservation in the model; it reduces the drift in total dry mass by two orders of magnitude[2]. The model time step also has some influence; doubling the time step from 6 to 12 seconds results in a significant increase in mass drift. But even in this case, the mass drift is considerably smaller than in the simulation without the pressure recalculation.

A.1.2 Dry-air density rescaling

In addition to the above change, the mass drift in the altered-model simulations is reduced to exactly zero by a rescaling of the dry-air density. Every hour of model time, the total mass of the atmosphere is calculated and the dry-air density rescaled by a spatially-invariant factor that ensures the total dry mass in the domain remains equal to its initial value. Since the mixing ratios of water species are unaltered by the dry-density rescaling, this also has the unfortunate side-affect of slightly altering

[2]This reduction in mass drift only occurs if the simulations are performed with variables stored in double precision; we perform all simulations using double precision variables.

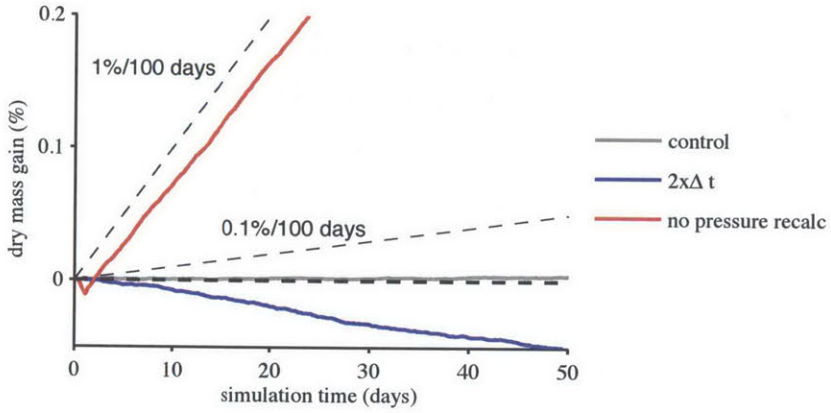

Figure A-1: Drift in dry mass in simulations of RCE. Control simulation (gray), simulation without pressure recalculation (red), and simulation with a doubled model time step (12 s) (blue). Also shown are reference lines for no mass increase (thick-dashed) and mass increase of 1% and 0.1% per hundred days of simulation (thin-dashed).

the total water mass in the atmosphere. However, this spurious water source is likely to be smaller than the spurious water source due to numerical error, as discussed in section A.3.

A.2 Energy conservation

A number of changes are made to CM1v16 to improve global energy conservation, including a change to the calculation of radiative heating rates (section A.2.1), and the inclusion of dissipative heating due to the friction between falling hydrometeors and air (section A.2.2).

A.2.1 Calculation of radiative heating rate

The tendency of potential temperature owing to radiative fluxes $\dot{\theta}_{rad}$ is calculated in CM1v16 based on a formula of the form,

$$\dot{\theta}_{rad} = \frac{g}{c_p \Pi} \frac{\partial F_{rad}}{\partial p},$$

where F_{rad} is the net-radiative flux density, g is the gravitational acceleration, c_p is the isobaric specific heat capacity of dry air, Π is the Exner function and p is the pressure. In the altered model this is calculated more accurately as,

$$\dot{\theta}_{rad} = \frac{c_v}{\rho c_{vm} c_p \Pi} \frac{\partial F_{rad}}{\partial z},$$

where ρ is the dry-air density, z is height and c_v is the specific heat capacity of dry air at constant volume. The variable c_{vm} is the specific heat capacity of moist air *per unit mass of dry air* at constant volume. As a result of this alteration to the model, the difference in the net-radiative fluxes into the atmosphere and the integrated atmospheric radiative cooling is less than 0.05 W m^{-2} in the altered model.

A.2.2 Inclusion of dissipative heating due to falling hydrometeors

The heating due to frictional dissipation of falling hydrometeors is neglected in CM1v16. This form of dissipative heating arises because the precipitation is falling at its terminal velocity, rather than accelerating under gravity, implying an upward frictional force equal in magnitude to the downward gravitational force (Pauluis et al., 2000). We include this precipitation related dissipation in the altered model by adding a term proportional to $\rho g v_h q_h$ to the thermodynamic equation. Here v_h and q_h are the fall speed and mixing ratio of a given hydrometeor, and we sum over all hydrometeors. This term accounts for a heating source of $2 - 4$ W m^{-2} in simulations of radiative-convective equilibrium (Pauluis et al., 2000), and thus results in a significant imbalance to the energy budget if neglected.

A.3 Artificial water sources

Accurate conservation of water is important for the energy budget because of the large latent heat carried by water vapor. Here we measure the global conservation of water as the difference between total water flux through the surface (i.e., evapo-

ration minus precipitation) and the time rate of change of atmospheric water mass over the same period. If these two quantities are not equal there exists an implied sink or source of water within the atmosphere. We may approximately convert this spurious water source, Q, to a spurious energy source by multiplying by the latent heat of vaporization evaluated at 273.15 K so that the energy source is given by, $E_{water} = L_{v0}Q$. The actual energy source implied by the spurious source of water is determined by the temperature and phase at which the spurious source removes or creates water. Nevertheless, E_{water} gives a rough upper bound on the effect of global non-conservation of water on the energy budget.

CM1v16 does not exactly conserve water mass for three main reasons,

i. the rain fallout routine does not conserve hydrometeor mass as it is advected downwards,

ii. the 6th order diffusion scheme is not scalar conserving,

iii. the numerical advection scheme is not scalar conserving.

In the altered model simulations we reduce the magnitude of (i) and (ii) via changes to the model formulation described below. Non-conservation by the advection scheme cannot be easily removed, but its effect is limited by increasing the magnitude of the scalar diffusion relative to the diffusion of momentum.

A.3.1 Numerics of rain fallout

Rain fallout in CM1v16 is performed by advecting hydrometeors downwards at their terminal velocity. This is done using a time step calculated based on the fall speed of hydrometeors that is typically shorter than the model dynamical time step. In the altered model we reduce this fallout time step by a factor of three to improve the conservation of hydrometeors. This reduces the energy input associated with the artificial water source by roughly 0.3 W m^{-2} (Fig. A-2).

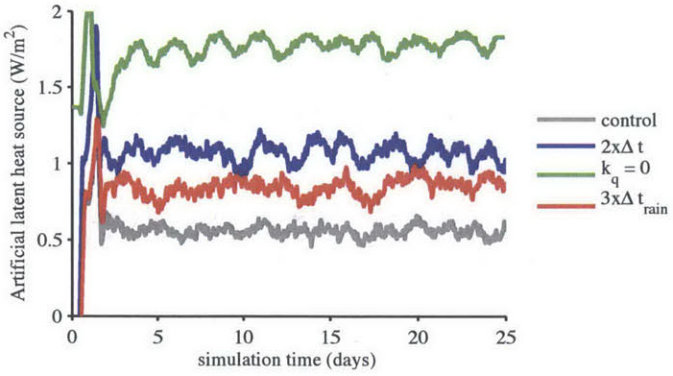

Figure A-2: Latent energy source E_{water} due to non-conservation of water in altered model simulations using standard configuration (gray), simulation with one third of the number of rain fallout time steps (red), simulation with doubled model time step (12 s) (blue), and simulation with no 6th order diffusion of scalars (green). Results are smoothed in time for presentation. The simulations shown include the density rescaling outlined in section A.1.2.

A.3.2 Diffusion and advection of water species

The simulations described in this thesis are conducted using a 6th order diffusion scheme applied to the velocity fields for numerical stability. This diffusion scheme is applied in addition to the Smagorinsky turbulence scheme used to represent sub-grid scale motions. An explicit diffusion scheme is used in combination with a non-diffusive advection scheme to allow for an explicit calculation of the associated frictional dissipation, and thus enable more accurate closure of the energy budget.

The 6th order scheme is also applied to the mixing ratios of water species.The 6th order diffusion of scalars implemented in in CM1v16 is not conservative. In CM1v16 the diffusion of scalars is implemented via an equation of the form,

$$D_q = c\Delta x_i \frac{\partial}{\partial x_i}\left(\Delta x_i^5 \frac{\partial^5 q}{\partial x_i^5}\right).$$

Here D_q is the diffusive tendency of the mixing ratio of some species q, Δx_i is grid spacing in direction x_i, and we sum over the index i. The coefficient $c = \frac{k_q}{64\Delta t}$, governs the strength of the diffusivity based on the time step Δt and a diffusivity parameter

k_q. In the altered model, this implementation is adjusted so that,

$$D_q = \frac{c}{\rho}\frac{\partial}{\partial x_i}\left(\rho c \Delta x_i^6 \frac{\partial^5 q}{\partial x_i^5}\right),$$

where ρ is the dry-air density. The form used in the altered model conserves the global integral of tracer mass[3].

In the altered model we take $k_q = 0.06$ for water species, and $k_u = 0.02$ for momentum, while no 6th order diffusion is applied to potential temperature. The different diffusion coefficients used are based on the minimum values required for stability, in the case of the winds, and reasonable scalar mass conservation, in the case of water species. If low values of k_q are used, the model does not conserve water very accurately, presumably due to the difficulty in accurately advecting water species in the presence of large humidity gradients.

Figure A-2 shows the spurious latent energy input to the atmosphere that occurs as a result of non-conservation of water in simulations of RCE. The simulations are similar to Fig. A-1, but in this case include the density rescaling outlined in section A.1.2. For the control simulation (gray), with $k_q = 0.06$, the artificial energy source is around 0.5 W m^{-2}. However, if diffusion of water species is turned off (green), this jumps to almost 2 W m^{-2}. The mass correction mentioned in the previous section is also a source of water vapor, but even for a mass drift as large as 1 % per 100 days (much larger than in the altered model simulations) this amounts to only 0.13 W m^{-2} in latent energy. The size of the model time step has some effect on the conservation of water, with a doubling of the time-step from 6 to 12 seconds leading to an increase in the spurious latent energy source of roughly 0.5 W m^{-2} (blue). The combination of including scalar diffusion, reducing the rain fallout time step, and running with a relatively small model time step reduces the non-conservation of water to relatively low levels.

[3]For momentum diffusion by the 6th order scheme, we keep the original formulation of CM1v16, but we include in the altered model a term in the thermodynamic budget representing the implied frictional heating associated with momentum diffusion.

A.4 Altered model simulations

Figure A-3 shows the degree of energy and mass conservation for the last 50 days of each slab-ocean simulation performed with the altered model. Based on the results of the previous sections we conduct the slab-ocean simulations with a relatively short time step of 6 seconds. The energy imbalance is generally less than 0.5 W/m^2, and to some degree follows the energy source due to the artificial source of mass. The latent energy source due to water mass conservation is larger than 1 W/m^2 in the very warmest simulations, but it does not seem to have much of an effect on the energy budget. This suggests that at least part of the spurious water source occurs for condensed water. Adding condensed water to the atmosphere that is then immediately rained out affects the energy budget only weakly because no spurious latent heating occurs. The artificial mass source in the simulations is also relatively small, being around 0.1 % per 100 days or smaller in all but one simulation.

The smallness of the energy imbalance relative to the precipitation dissipation [2-4 W m^{-2} (Pauluis et al., 2000)], which was neglected in CM1v16, indicates that the energy budget of the altered model is well closed compared to the energy budget of CM1v16. Similarly, based on the results of figure A-1, the mass source associated with the density rescaling in the altered model is much smaller than would be required in CM1v16.

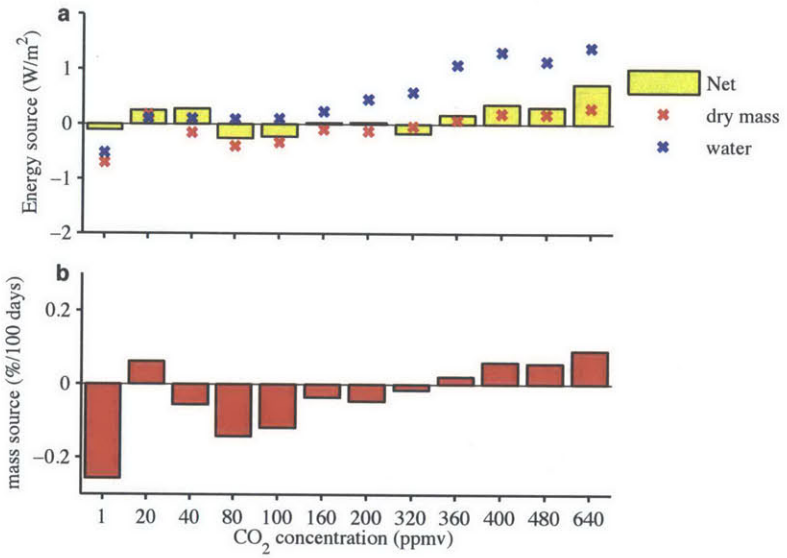

Figure A-3: Energy and mass non-conservation in slab-ocean simulations with the altered model. (a) Net energy imbalance as measured by the difference between the integrated atmospheric radiative and turbulent flux divergence and the change in atmospheric energy content over the last 50 days of each simulation (yellow bars). Latent energy source due to water non-conservation (blue crosses) and energy source due to artificial mass source (red crosses) are also shown. (b) Source of mass introduced by the mass rescaling outlined in section A.1.2 in order to keep the dry mass in the simulation constant with time.

Bibliography

Allan, R. P. and B. J. Soden, 2008: Atmospheric warming and the amplification of precipitation extremes. *Science*, **321**, 1481–1484.

Arakawa, A., 2004: The cumulus parameterization problem: past, present, and future. *J. Climate*, **17**, 2493–2525.

Arakawa, A. and W. H. Schubert, 1974: Interaction of a cumulus cloud ensemble with the large-scale environment, part I. *J. Atmos. Sci.*, **31**, 674–701.

Baker, M. B., A. M. Blyth, H. J. Christian, J. Latham, K. L. Miller, and A. M. Gadian, 1999: Relationships between lightning activity and various thundercloud parameters: satellite and modelling studies. *Atmos. Res.*, **51**, 221–236.

Berg, P., C. Moseley, and J. O. Haerter, 2013: Strong increase in convective precipitation in response to higher temperatures. *Nat. Geosci.*, **6**, 181–185.

Bjerknes, J., 1938: Saturated-adiabatic ascent of air through dry-adiabatically descending environment. *Quart. J. Roy. Meteor. Soc*, **64**, 325–330.

Böing, S. J., H. J. Jonker, W. A. Nawara, and A. P. Siebesma, 2014: On the deceiving aspects of mixing diagrams of deep cumulus convection. *J. Atm. Sci.*, **71**.

Bretherton, C. S., P. N. Blossey, and M. Khairoutdinov, 2005: An energy-balance analysis of deep convective self-aggregation above uniform SST. *J. Atmos. Sci.*, **62**, 4273–4292.

Bretherton, C. S., J. R. McCaa, and H. Grenier, 2004: A new parameterization for shallow cumulus convection and its application to marine subtropical cloud-topped boundary layers. part I: Description and 1D results. *Mon. Wea. Rev.*, **132**, 864–882.

Bretherton, C. S. and S. Park, 2008: A new bulk shallow-cumulus model and implications for penetrative entrainment feedback on updraft buoyancy. *J. Atmos. Sci.*, **65**, 2174–2193.

Bryan, G. H. and J. M. Fritsch, 2002: A benchmark simulation for moist nonhydrostatic numerical models. *Mon. Wea. Rev.*, **130**, 2917–2928.

Bryan, G. H. and R. Rotunno, 2009: The maximum intensity of tropical cyclones in axisymmetric numerical model simulations. *Mon. Wea. Rev.*, **137**, 1770–1789.

Bryan, G. H., J. C. Wyngaard, and J. M. Fritsch, 2003: Resolution requirements for the simulation of deep moist convection. *Mon. Wea. Rev.*, **131**, 2394–2416.

Cash, B. A., P. J. Kushner, and G. K. Vallis, 2002: The structure and composition of the annular modes in an aquaplanet general circulation model. *J. Atmos. Sci.*, **59**, 3399–3414.

Chaboureau, J.-P., J.-P. Cammas, J. Duron, P. J. Mascart, N. M. Sitnikov, and H.-J. Voessing, 2007: A numerical study of tropical cross-tropopause transport by convective overshoots. *Atmos. Chem. Phys.*, **7**, 1731–1740.

Chadwick, R., I. Boutle, and G. Martin, 2013: Spatial patterns of precipitation change in CMIP5: Why the rich do not get richer in the tropics. *J. Climate*, **26**, 3803–3822.

Cohen, B. G. and G. C. Craig, 2006: Fluctuations in an equilibrium convective ensemble. part II: Numerical experiments. *J. Atmos. Sci.*, **63**, 2005–2015.

Collins, M., et al., 2013: Long-term climate change: Projections, commitments and irreversibility. *Climate Change 2013: The Physical Science Basis. Contribution of Working Group I to the Fifth Assessment Report of the Intergovernmental Panel on Climate Change*, T. Stocker, D. Qin, G.-K. Plattner, M. Tignor, S. Allen, J. Boschung, A. Nauels, Y. Xia, V. Bex, and P. Midgley, Eds., Cambridge Univ. Press, chap. 12.

Craig, G. C., 1996: Dimensional analysis of a convecting atmosphere in equilibrium with external forcing. *Quart. J. Roy. Met. Soc.*, **122**, 1963–1967.

Craig, G. C. and B. G. Cohen, 2006: Fluctuations in an equilibrium convective ensemble. Part I: Theoretical formulation. *J. Atmos. Sci.*, **63**, 1996–2004.

Cronin, T. W. and K. A. Emanuel, 2013: The climate time scale in the approach to radiative-convective equilibrium. *J. Adv. Model. Earth Syst.*, **5**, 843–849.

de Rooy, W. C., et al., 2012: Entrainment and detrainment in cumulus convection: an overview. *Quart. J. Roy. Met. Soc.*, **10**.

Del Genio, A. D., W. Kovari, M.-S. Yao, and J. Jonas, 2005: Cumulus microphysics and climate sensitivity. *J. Climate*, **18**, 2376–2387.

Del Genio, A. D., M.-S. Yao, and J. Jonas, 2007: Will moist convection be stronger in a warmer climate? *Geophys. Res. Lett.*, **34**, L16 703, doi:10.1029/2007GL030525.

Derbyshire, S. H., I. Beau, P. Bechtold, J.-Y. Grandpeix, J.-M. Piriou, J.-L. Redelsperger, and P. M. M. Soares, 2004: Sensitivity of moist convection to environmental humidity. *Quart. J. Roy. Meteor. Soc.*, **130**, 3055–3079.

Dopplick, T. G., 1972: Radiative heating of the global atmosphere. *J. Atmos. Sci.*, **29**, 1278–1294.

Emanuel, K., 2001: Quasi-equilibrium thinking. *General Circulation Model Development: Past, Present, and Future*, D. Randall, Ed., Academic Press, International Geophysics, Vol. 70, 225–255.

Emanuel, K., A. A. Wing, and E. M. Vincent, 2014: Radiative-convective instability. *J. Adv. Model. Earth Syst.*, **6**, 75–90, doi:10.1002/2013MS000270.

Emanuel, K. A. and M. Bister, 1996: Moist convective velocity and buoyancy scales. *J. Atmos. Sci.*, **53**, 3276–3285.

Emanuel, K. A., J. D. Neelin, and C. S. Bretherton, 1994: On large-scale circulations in convecting atmospheres. *Quart. J. Roy. Meteor. Soc.*, **120**, 1111–1143.

Fasullo, J., 2012: A mechanism for land-ocean contrasts in global monsoon trends in a warming climate. *Clim. Dyn.*, **39**, 1137–1147.

Frierson, D. M. W., 2007: The dynamics of idealized convection schemes and their effect on the zonally averaged tropical circulation. *J. Atmos. Sci.*, **64**, 1959–1976.

Frierson, D. M. W., I. M. Held, and P. Zurita-Gotor, 2006: A gray-radiation aquaplanet moist GCM. Part I: Static stability and eddy scale. *J. Atmos. Sci.*, **63**, 2548–2566.

Fyfe, J. C., G. J. Boer, and G. M. Flato, 1999: Arctic and antarctic oscillations and their projected changes under global warming. *Geophys. Res. Lett.*, **26**, 1601–1604, doi:10.1029/1999GL900317.

Garner, S. T., D. M. W. Frierson, I. M. Held, O. Pauluis, and G. K. Vallis, 2007: Resolving convection in a global hypohydrostatic model. *J. Atmos. Sci.*, **64**, 2061–2075.

Hardwick Jones, R., S. Westra, and A. Sharma, 2010: Observed relationships between extreme sub-daily precipitation, surface temperature, and relative humidity. *Geophys. Res. Lett.*, **37**, L22 805, doi:10.1029/2010GL045081.

Hartmann, D. L., J. R. Holton, and Q. Fu, 2001: The heat balance of the tropical tropopause, cirrus, and stratospheric dehydration. *Geophys. Res. Lett.*, **28**, 1969–1972, doi:10.1029/2000GL012833.

Hartmann, D. L. and K. Larson, 2002: An important constraint on tropical cloud-climate feedback. *Geophys. Res. Lett.*, **29**, 1951, doi:10.1029/2002GL015835.

Held, I. M., R. S. Hemler, and V. Ramaswamy, 1993: Radiative-convective equilibrium with explicit two-dimensional moist convection. *J. Atm. Sci.*, **50**, 3909–3927.

Held, I. M. and B. J. Soden, 2006: Robust responses of the hydrological cycle to global warming. *J. Climate*, **19**, 5686–5699.

Heus, T. and H. J. J. Jonker, 2008: Subsiding shells around shallow cumulus clouds. *J. Atm. Sci.*, **65**, 1003–1018.

Heus, T., G. Van Dijk, H. J. Jonker, and H. E. Van den Akker, 2008: Mixing in shallow cumulus clouds studied by lagrangian particle tracking. *J. Atm. Sci.*, **65**, 2581–2597.

Holloway, C. E. and J. D. Neelin, 2009: Moisture vertical structure, column water vapor, and tropical deep convection. *J. Atmos. Sci.*, **66**, 1665–1683.

Ingram, W., 2010: A very simple model for the water vapour feedback on climate change. *Quart. J. Royal Met. Soc.*, **136**, 30–40.

Islam, S., R. L. Bras, and K. A. Emanuel, 1993: Predictability of mesoscale rainfall in the tropics. *J. Appl. Meteor.*, **32**, 297–310.

Jensen, E. J., A. S. Ackerman, and J. A. Smith, 2007: Can overshooting convection dehydrate the tropical tropopause layer? *J. Geophys. Res.-Atmos.*, **112**, D11 209, doi:10.1029/2006JD007943.

Kain, J. S. and J. M. Fritsch, 1990: A one-dimensional entraining/detraining plume model and its application in convective parameterization. *J. Atm. Sci.*, **47**, 2784–2802.

Khairoutdinov, M. and K. Emanuel, 2013: Rotating radiative-convective equilibrium simulated by a cloud-resolving model. *J. Adv. Model. Earth Syst.*, **5**, 816–825, doi: 10.1002/2013MS000253.

Kharin, V. V., F. W. Zwiers, X. Zhang, and G. C. Hegerl, 2007: Changes in temperature and precipitation extremes in the IPCC ensemble of global coupled model simulations. *J. Climate*, **20**, 1419–1444.

Knutson, T. R. and S. Manabe, 1995: Time-mean response over the tropical pacific to increased CO_2 in a coupled ocean-atmosphere models. *J. Climate*, **8**, 2181–2199.

Kuang, Z., P. Blossey, and C. Bretherton, 2005: A new approach for 3D cloud-resolving simulations of large-scale atmospheric circulation. *Geophys. Res. Lett*, **32**, 1–4.

Kuang, Z. and C. S. Bretherton, 2004: Convective influence on the heat balance of the tropical tropopause layer: a cloud-resolving model study. *J. Atm. Sci.*, **61**, 2919–2927.

Kuang, Z. and C. S. Bretherton, 2006: A mass-flux scheme view of a high-resolution simulation of a transition from shallow to deep cumulus convection. *J. Atmos. Sci.*, **63**, 1895–1909.

Kuang, Z. and D. L. Hartmann, 2007: Testing the fixed anvil temperature hypothesis in a cloud-resolving model. *J. Climate*, **20**, 2051–2057.

Kushner, P. J., I. M. Held, and T. L. Delworth, 2001: Southern Hemisphere atmospheric circulation response to global warming. *J. Climate*, **14**, 2238–2249.

Lenderink, G., H. Y. Mok, T. C. Lee, and G. J. van Oldenborgh, 2011: Scaling and trends of hourly precipitation extremes in two different climate zones – Hong Kong and the Netherlands. *Hydrol. Earth Syst. Sci.*, **15**, 3033–3041.

Lenderink, G. and E. van Meijgaard, 2008: Increase in hourly precipitation extremes beyond expectations from temperature changes. *Nature Geosci.*, **1**, 511–514.

Lin, C. and A. Arakawa, 1997a: The macroscopic entrainment processes of simulated cumulus ensemble. part i: Entrainment sources. *J. Atm. Sci.*, **54**, 1027–1043.

Lin, C. and A. Arakawa, 1997b: The macroscopic entrainment processes of simulated cumulus ensemble. part II: Testing the entraining-plume model. *J. Atm. Sci.*, **54**, 1044–1053.

Lin, Y.-L., R. D. Farley, and H. D. Orville, 1983: Bulk parameterization of the snow field in a cloud model. *J. Clim. Appl. Meteorol.*, **22**, 1065–1092.

Lorenz, D. J. and E. T. DeWeaver, 2007: Tropopause height and zonal wind response to global warming in the IPCC scenario integrations. *J. Geophys. Res.*, **112**, D10 119, doi:10.1029/2006JD008087.

Loriaux, J. M., G. Lenderink, S. R. De Roode, and A. P. Siebesma, 2013: Understanding convective extreme precipitation scaling using observations and an entraining plume model. *J. Atmos. Sci*, **70**, 3641–3655.

Manabe, S. and R. Strickler, 1964: Thermal equilibrium of the atmosphere with a convective adjustment. *J. Atmos. Sci.*, **21**, 361–385.

Manabe, S. and R. Wetherald, 1967: Thermal Equilibrium of the Atmosphere with a Given Distribution of Relative Humidity. *J. Atmos. Sci.*, **24**, 241–259.

Mather, J. H., T. P. Ackerman, W. E. Clements, F. J. Barnes, M. D. Ivey, L. D. Hatfield, and R. M. Reynolds, 1998: An atmospheric radiation and cloud station in the tropical western Pacific. *Bull. Amer. Meteor. Soc.*, **79**, 627–642.

Merlis, T. M. and T. Schneider, 2011: Changes in zonal surface temperature gradients and walker circulations in a wide range of climates. *J. Climate*, **24**, 4757–4768.

Mitchell, J. and W. Ingram, 1992: Carbon dioxide and climate: Mechanisms of changes in cloud. *J. Climate*, **5**, 5–21.

Molinari, J., D. M. Romps, D. Vollaro, and L. Nguyen, 2012: CAPE in tropical cyclones. *J. Atmos. Sci.*, **69**, 2452–2463.

Morales, R. and A. Nenes, 2010: Characteristic updrafts for computing distribution-averaged cloud droplet number and stratocumulus cloud properties. *J. Geophys. Res. Atmospheres*, **115**, D18 220, doi:10.1029/2009JD013233.

Muller, C., 2013: Impact of convective organization on the response of tropical precipitation extremes to warming. *J. Climate*, **26**, 5028–5043.

Muller, C. J. and I. M. Held, 2012: Detailed investigation of the self-aggregation of convection in cloud-resolving simulations. *J. Atm. Sci.*, **69**, 2551–2565.

Muller, C. J., P. A. O'Gorman, and L. E. Back, 2011: Intensification of precipitation extremes with warming in a cloud-resolving model. *J. Climate*, **24**, 2784–2800.

Nakićenović, N., et al., 2000: *IPCC Special Report on Emissions Scenarios (SRES).* Cambridge University Press.

O'Gorman, P. A., 2010: Understanding the varied response of the extratropical storm tracks to climate change. *Proc. Nat. Acad. Sci.*, **107**, 19 176–19 180.

O'Gorman, P. A., 2012: Sensitivity of tropical precipitation extremes to climate change. *Nature Geosci.*, **5**, 697–700.

O'Gorman, P. A., R. P. Allan, M. P. Byrne, and M. Previdi, 2011: Energetic constraints on precipitation under climate change. *Surv. Geophys.*, doi:10.1007/s10712-011-9159-6.

O'Gorman, P. A. and T. Schneider, 2008: The hydrological cycle over a wide range of climates simulated with an idealized GCM. *J. Climate*, **21**, 3815–3832.

O'Gorman, P. A. and T. Schneider, 2009a: The physical basis for increases in precipitation extremes in simulations of 21st-century climate change. *Proc. Nat. Acad. Sci.*, **106**, 14 773–14 777.

O'Gorman, P. A. and T. Schneider, 2009b: Scaling of precipitation extremes over a wide range of climates simulated with an idealized GCM. *J. Climate*, **22**, 5676–5685.

O'Gorman, P. A. and M. S. Singh, 2013: Vertical structure of warming consistent with an upward shift in the middle and upper troposphere. *Geophys. Res. Lett.*, **40**, 1838–1842.

Paluch, I., 1979: The entrainment mechanism in Colorado cumuli. *J. Atmos. Sci.*, **36**, 2467–2478.

Parodi, A. and K. Emanuel, 2009: A theory for buoyancy and velocity scales in deep moist convection. *J. Atmos. Sci.*, **66**, 3449–3463.

Parodi, A., E. Foufoula-Georgiou, and K. Emanuel, 2011: Signature of microphysics on spatial rainfall statistics. *J. Geophys. Res.*, **116**, D14 119, doi:10.1029/2010JD015124.

Pauluis, O., V. Balaji, and I. M. Held, 2000: Frictional dissipation in a precipitating atmosphere. *J. Atmos. Sci.*, **57**, 989–994.

Pauluis, O., D. Frierson, S. Garner, I. Held, and G. Vallis, 2006: The hypohydrostatic rescaling and its impacts on modeling of atmospheric convection. *Theor. Comp. Fluid Dyn.*, **20**, 485–499.

Pauluis, O. and I. M. Held, 2002a: Entropy budget of an atmosphere in radiative-convective equilibrium. Part I: Maximum work and frictional dissipation. *J. Atmos. Sci.*, **59**, 125–139.

Pauluis, O. and I. M. Held, 2002b: Entropy budget of an atmosphere in radiative-convective equilibrium. Part II: Latent heat transport and moist processes. *J. Atmos. Sci.*, **59**, 140–149.

Pauluis, O. and J. Schumacher, 2011: Self-aggregation of clouds in conditionally unstable moist convection. *Proc. Nat. Acad. Sci.*, **108**, 12 623–12 628.

Pauluis, O. M. and A. A. Mrowiec, 2013: Isentropic analysis of convective motions. *J. Atm. Sci.*, **70**, 3673–3688.

Popke, D., B. Stevens, and A. Voigt, 2013: Climate and climate change in a radiative-convective equilibrium version of ECHAM6. *J. Adv. Model. Earth Syst.*, **5**, 1–14.

Potter, B. E., 1991: Improvements to a commonly used cloud microphysical bulk parameterization. *J. Appl. Meteorol.*, **30**, 1040–1042.

Raymond, D. J. and A. M. Blyth, 1986: A stochastic mixing model for nonprecipitating cumulus clouds. *J. Atm. Sci.*, **43**, 2708–2718.

Raymond, D. J. and X. Zeng, 2005: Modelling tropical atmospheric convection in the context of the weak temperature gradient approximation. *Quart. J. Roy. Meteor. Soc*, **131**, 1301–1320.

Rennó, N. O. and A. P. Ingersoll, 1996: Natural convection as a heat engine: A theory for CAPE. *J. Atmos. Sci.*, **53**, 572–585.

Reuter, G. W., 1986: A historical review of cumulus entrainment studies. *Bull. Amer. Meteor. Soc.*, **67**, 151–154.

Riehl, H. and J. S. Malkus, 1958: On the heat balance in the equatorial trough zone. *Geophysica*, **6**, 503–538.

Robe, F. R. and K. A. Emanuel, 1996: Moist convective scaling: Some inferences from three-dimensional cloud ensemble simulations. *J. Atmos. Sci.*, **53**, 3265–3275.

Romps, D., 2008: The dry-entropy budget of a moist atmosphere. *J. Atmos. Sci.*, **65**, 3779–3799.

Romps, D. M., 2010: A direct measure of entrainment. *J. Atm. Sci.*, **67**, 1908–1927.

Romps, D. M., 2011: Response of tropical precipitation to global warming. *J. Atmos. Sci.*, **68**, 123–138.

Romps, D. M. and Z. Kuang, 2010a: Do undiluted convective plumes exist in the upper tropical troposphere? *J. Atmos. Sci.*, **67**, 468–484.

Romps, D. M. and Z. Kuang, 2010b: Nature versus nurture in shallow convection. *J. Atm. Sci.*, **67**.

Rowell, D. P., 2012: Sources of uncertainty in future changes in local precipitation. *Clim. Dyn.*, **39**, 1929–1950.

Sahany, S., J. D. Neelin, K. Hales, and R. B. Neale, 2012: Temperature-moisture dependence of the deep convective transition as a constraint on entrainment in climate models. *J. Atm. Sci.*, **69**, 1340–1358.

Schneider, T., P. A. O'Gorman, and X. Levine, 2010: Water vapor and the dynamics of climate changes. *Rev. Geophys*, **48**, RG3001, doi:10.1029/2009RG000302.

Seager, R., N. Naik, and G. A. Vecchi, 2010: Thermodynamic and dynamic mechanisms for large-scale changes in the hydrological cycle in response to global warming*. *J. Climate*, **23**, 4651–4668.

Sherwood, S. C., W. Ingram, Y. Tsushima, S. Masaki, M. Roberts, P. L. Vidale, and P. A. O'Gorman, 2010: Relative humidity changes in a warmer climate. *Geophys. Res. Lett*, **115**, D09 104, doi:10.1029/2009JD012585.

Siebesma, A. P., et al., 2003: A large eddy simulation intercomparison study of shallow cumulus convection. *J. Atm. Sci.*, **60**, 1201–1219.

Singh, M. S. and P. A. O'Gorman, 2012: Upward shift of the atmospheric general circulation under global warming: theory and simulations. *J. Climate.*, **25**, 8259–8276.

Singh, M. S. and P. A. O'Gorman, 2013: Influence of entrainment on the thermal stratication in simulations of radiative-convective equilibrium. *Geophys. Res. Lett.*, **40**, 4398–4403, doi:10.1002/grl.50796.

Smagorinsky, J., 1963: General circulation experiments with the primitive equations: I. the basic experiment*. *Mon. Wea. Rev.*, **91**, 99–164.

Sobel, A. H. and C. S. Bretherton, 2000: Modeling tropical precipitation in a single column. *J. Climate*, **13**, 4378–4392.

Sobel, A. H. and S. J. Camargo, 2011: Projected future changes in tropical summer climate. *J. Climate*, **24**, 473–487.

Son, S., et al., 2008: The impact of stratospheric ozone recovery on the southern hemisphere westerly jet. *Science*, **320**, 1486–1489.

Stommel, H., 1947: Entrainment of air into a cumulus cloud. *J. Meteorol.*, **4**, 91–94.

Takahashi, K., 2009: Radiative constraints on the hydrological cycle in an idealized radiative-convective equilibrium model. *J. Atmos. Sci.*, **66**, 77–91.

Taylor, G. R. and M. B. Baker, 1991: Entrainment and detrainment in cumulus clouds. *J. Atm. Sci.*, **48**, 112–121.

Taylor, K., 2001: Summarizing multiple aspects of model performance in a single diagram. *J. Geophys. Res*, **106**, 7183–7192.

Tiedtke, M., 1989: A comprehensive mass flux scheme for cumulus parameterization in large-scale models. *Mon. Wea. Rev.*, **117**, 1779–1800.

Tomita, H., H. Miura, S. Iga, T. Nasuno, and M. Satoh, 2005: A global cloud-resolving simulation: Preliminary results from an aqua planet experiment. *Geophys. Res. Lett.*, **32**, L08 805, doi:10.1029/2005GL022459.

Tompkins, A. and G. Craig, 1998: Radiative–convective equilibrium in a three-dimensional cloud-ensemble model. *Quart. J. Roy. Met. Soc.*, **124**, 2073–2097.

Tompkins, A. M. and G. C. Craig, 1999: Sensitivity of tropical convection to sea-surface temperature in the absence of large-scale flow. *J. Climate*, **12**, 462–476.

Vecchi, G. A. and B. J. Soden, 2007: Global warming and the weakening of the tropical circulation. *J. Climate*, **20**, 4316–4340.

Westra, S., L. V. Alexander, and F. W. Zwiers, 2013: Global increasing trends in annual maximum daily precipitation. *J. Climate*, **26**, 3904–3918.

Wicker, L. J. and W. C. Skamarock, 2002: Time-splitting methods for elastic models using forward time schemes. *Mon. Wea. Rev.*, **130**, 2088–2097.

Wilcox, E. M. and L. J. Donner, 2007: The frequency of extreme rain events in satellite rain-rate estimates and an atmospheric general circulation model. *J. Climate*, **20**, 53 – 69.

Wing, A. A. and K. A. Emanuel, 2014: Physical mechanisms controlling self-aggregation of convection in idealized numerical modeling simulations. *J. Adv. Model. Earth Syst.*, **6**, 59–74, doi:10.1002/2013MS000269.

Xu, K.-M. and K. A. Emanuel, 1989: Is the tropical atmosphere conditionally unstable? *Mon. Wea. Rev.*, **117**, 1471–1479.

Yin, J., 2005: A consistent poleward shift of the storm tracks in simulations of 21st century climate. *Geophys. Res. Lett*, **32**, L18 701, doi:10.1029/2005GL023684.

Zelinka, M. and D. Hartmann, 2010: Why is longwave cloud feedback positive. *J. Geophys. Res.*, **115**, D16 117, doi:10.1029/2010JD013817.

Zhang, G. J. and H. Wang, 2006: Toward mitigating the double ITCZ problem in NCAR CCSM3. *Geophys. Res. Lett.*, **33**, L06 709, doi:10.1029/2005GL025229.

Zipser, E. J., 2003: Some views on "hot towers" after 50 years of tropical field programs and two years of TRMM data. *Meteor. Monogr.*, **29**, 49–58.